2023-08-28

Physical, Mechanical and Elastic Properties of Chondrite Lithologies

Ciceri, Fabio

UNIVERSITY OF CALGARY

Physical, Mechanical and Elastic Properties of Chondrite Lithologies

by

Fabio Ciceri

A THESIS

SUBMITTED TO THE FACULTY OF GRADUATE STUDIES

IN PARTIAL FULFILMENT OF THE REQUIREMENTS FOR THE

DEGREE OF DOCTOR OF PHILOSOPHY

GRADUATE PROGRAM IN GEOLOGY AND GEOPHYSICS

CALGARY, ALBERTA

AUGUST, 2023

ABSTRACT

This project measured the physical, mechanical, and elastic properties of a range of chondrite lithologies, a domain that was inadequately explored. The properties measured are porosity, bulk and grain density, seismic velocity (P and S waves), Unconfined Compressive Strength, Direct Shear Strength, Hardness (HLD)/Coefficient of Restitution, dynamic elastic moduli (Young's modulus, Shear modulus, Bulk modulus, Poisson's ratio), Static Young's Modulus, Proportional Limit, and Elemental Compositions. The complexity of measuring these properties accurately in small samples (ranging from 2.5 mm to 2 cm) is underscored, particularly due to the inherent weakness of some lithologies. Innovative adaptations of established methodologies, as elaborated in the Methods chapter, have been implemented to overcome these challenges and conform to ASTM International Standards. Concurrently, this study seeks to encourage the adoption of measuring standards within the planetary science community, fostering improved data cross-referencing and contextual interpretation of future asteroid samples. This study also examined correlations among meteorite properties, with the potential to predict properties that would normally require destructive testing. This study provides a database, contributing to an enhanced grasp of the deformational characteristics exhibited by meteorites and asteroids. This knowledge advancement facilitates modeling of asteroid geology and internal structures.

ACKNOWLEDGEMENTS

Over the course of these years, I've navigated numerous personal and worldwide obstacles. I successfully completed my candidacy remotely due to the COVID-19 Pandemic, which resulted in nearly a year of restricted access to the laboratory. To have come this far is also thanks to some of the people I had the pleasure to work with. A heartfelt thank goes to Lincoln Hanton – his unwavering support in the lab, in the field, in the office walls, and his friendship have made my journey much easier. Lincoln also profoundly ingrained in me the significance of meticulous attention to detail, contributing to my growth as a scientist. I would also like to extend thanks to my supervisor, Dr. Alan Hildebrand, for his support throughout these years. I'm particularly thankful to Alan for involving me in exceptional opportunities, such as tracking fireballs, meteorite searches, and engagement in the OSIRIS-REx mission. I am also grateful to my committee supervisor Prof. Christopher Clarkson, and to Dr. Amin Ghanizadeh. Their willingness to go the extra mile to help me refine measurements, discussions, and provide invaluable suggestions has been truly appreciated. A thank also to Adnan Younis for helping with the portable XRF measurements. I also thank my committee supervisor Prof. Benjamin Tutolo for giving me access to the Tutolo Reactive Transport Group lab at the University of Calgary. I want to thank Prof. Ron Wong for giving me access to the laboratory in Engineering Faculty facilities at the University of Calgary and to the support of Dr. Yadong Zhang and Dr. Chee Wong. I am also thankful to Dr. Mahadia Ibrahim for the support in the fist years if my PhD and her life lessons. Finally, my heartfelt gratitude to my family, Bianca, and my faithful companion, Bennu. Each of them has contributed to making this journey significantly better.

I am also grateful to P.R. Heck and J. L. Holstein and the Field Museum for the Murchison sample loan. I am also grateful to M. Mazur for donating a sample of Moss. The works has been supported by a grant from the Planetary Exploration group of the Canadian Space Agency.

DEDICATION

To my Mum

Doriana

Your strength will always be my inspiration…

TABLE OF CONTENT

LIST OF TABLES

LIST OF FIGURES AND ILLUSTRATIONS

so

1: INTRODUCTION

Four point six billion years ago the Solar System was born. It began with the collapse of a cold giant molecular cloud composed mostly of hydrogen and helium, along with trace amounts of other elements often incorporated into fine dust grains. This cloud, eventually forming the Solar Nebula, started to contract under the influence of its own gravity, flattening into a spinning disk due to conservation of angular momentum. The central region of the disk became denser and hotter, leading to the formation of the Sun at its core. The Sun started to fuse hydrogen atoms (and other nuclides) releasing immense amounts of energy in the form of light and heat. [Lewis, 2004]

Around the young Sun, the remaining material in the disk began to cool after substantial mixing and homogenization in the vapor phase, leading to condensation of reprocessed nebular dust particles. These dust particles coalesced in a hierarchy of growth and collisions eventually forming planetesimals. Continuing collisions and accretion of these planetesimals formed the planets, particularly the terrestrial planets. In the inner Solar System Mercury, Venus, Earth, and Mars formed, while in the colder outer Solar System the gas giants, Jupiter, Saturn, Uranus, and Neptune also grew by gravitationally attracting gases onto their rock and ice cores. [Lewis, 2004]

But the Solar System is not just made of planets. In the inner Solar System smaller rocky objects know as asteroids are the most common objects: the biggest asteroid is Ceres with a diameter of 950 km [Michel et al., 2015]. They primarily inhabit the Main Asteroid Belt that is located between Mars and Jupiter, spanning 2.06 to 3.65 astronomical units (AU) from the Sun. The distribution of asteroids in the main belt is a result of billions of years of collisional and dynamic processes. These processes have led to the formation the extant

diffuse Asteroid Belt punctuated by asteroid families and by orbital gaps due to gravitational resonances with the other planets. When asteroids enter a resonance region within the active environment of the main belt, they can be ejected from it due to perturbations from Jupiter or other planets, such as the secular resonance with Saturn. Some of these ejected asteroids find their way into the inner Solar System and become known as near-Earth objects, posing a potential collision risk with the Earth and the other terrestrial planets. Sometimes these objects hit the Earth and, if they survive atmospheric entry, become meteorites.

Comets, on the other hand, formed in the outer regions of the protoplanetary disk and are preserved in two other reservoirs of planetesimals. One reservoir is the Kuiper Belt, which extends along the ecliptic outward from Neptune's orbit at approximately 35 AU to several hundred AU. The other reservoir is a spherical region beyond the Kuiper Belt called the Oort cloud, ranging from 10^3 to 10^5 AU solar distance. Unlike asteroids, comets contain significant amounts of water ice and other volatiles. When heated near the Sun, the subliming volatiles form a coma around the comet nucleus. The orbital evolution of comets is primarily influenced by gravitational perturbations from the gas giant planets during their formation (Jupiter, Uranus, Saturn, and Neptune), as well as by galactic and stellar perturbations as they move farther away from the Sun.

Asteroids and comets are relatively primitive objects within the Solar System offering insights into its early compositional structure, but also serving as evidence of the collisional and dynamical processes that have shaped their current distribution. The birth of the Solar System was a complex and dynamic process that evolved rapidly for millions of years but

has continued at much slower rates for billions of years. It involved the interplay of gravity, heat, and the physical properties of the materials condensed in the Solar Nebula.

1.1 What is a Meteorite?

Meteorites represent the biggest collection of extraterrestrial material that we have available to study as samples and in some contexts, in situ. Whenever celestial bodies collide in space, the resulting fragments disperse through nearby orbital space, occasionally finding their way to other planets, including Earth. When the fragments are up to 100 cm in size and they are orbiting the Sun, they have been called meteoroids. As they traverse through the Earth's atmosphere, they create a captivating visual spectacle called a meteor or, if large enough, a fireball. Should these fragments endure the atmospheric entry and be recovered from the ground, they are termed meteorites (Figure 1.1).

Figure 1.1: photo of the fireball of the Golden meteorite used in this study. [from Hao Qin]

In the realm of meteorites, it is crucial to differentiate between two terms: "falls" and "finds." “Falls”, which are far less common, refer to meteorites that are recovered after their fall (atmospheric entry) has been observed. On the other hand, “finds” pertain to meteorites that are retrieved without having been witnessed falling. One drawback of finds is that they may have been lying on the ground for an unspecified period often in extreme weather conditions (most are collected in deserts and Antarctica) enduring various levels of weathering in the terrestrial atmosphere. Consequently, they progressively less accurately represent their parent bodies. The impact of weathering becomes noticeable when examining the ratio of iron meteorites to stone meteorites among finds. Iron meteorites, despite constituting less than 5% of all collected meteorites, are more abundant among finds due to their superior resilience against terrestrial weathering [e.g., McSween, 1999].

Meteorites provide vast amounts and diverse information about the evolution and history of the Solar System and the interstellar environment. However, our access to extraterrestrial material is limited by the need to survive atmospheric entry which seems to be biased towards stronger lithologies [e.g., Lewis, 2004]. In consequence, 93.5 % of the falls on Earth are stony meteorites and just 3.6 % of them are carbonaceous chondrites [e.g., Gattacceca et al., 2011]. Cometary material is not known to have ever survived to the ground despite numerous large fireballs during cometary meteor showers. Because of their rarity, carbonaceous chondrites are some of the least understood among meteorite types.

Meteorites are classified based on their mineralogical and petrographic characteristics and their whole-rock chemical and isotopic compositions. Historically, they are divided into three major groups: Iron meteorites, stony meteorites, and stony-iron meteorites. Iron

meteorites primarily comprise nickel-iron metal alloys, while stony meteorites are predominantly composed of silicates and oxide minerals with some metal grains [McSween, 1999]. Stony-iron meteorites possess nearly equal proportions of metals and silicates, with the spectacular pallasites being a common example within this group. Currently, (non-planetary/lunar) meteorites are divided into more than three dozen separate clans with additional meteorites occurring as single or small number cases [e.g., Weissberg et al., 2006]; they are broadly divided into chondrites and achondrites which reflects the degree of geological processing on their parent bodies. This study is focused on some classes of chondritic meteorites.

1.2 Stony meteorites - Chondrites

The chondrites (almost always stony meteorites) are characterized by the presence of chondrules (typically 1-2 mm in size), spherical grains that are mainly composed of silicate minerals. These chondrules give the meteorites a distinctive texture and appearance and they are thought to the result of melting and otherwise reprocessing the first fine dust condensates from the Solar Nebula. The chondrules formed as solidified melt droplets representing processing within the disk at high temperatures. Most of the chondrites/stony meteorites originate from objects that lacked sufficient size to undergo complete melting and differentiation, thereby preserving some of their component's chemistry and structure, providing us with a glimpse into the Early Solar System dating back 4.6 billion years.

There are 15 chondrite groups including 3 Ordinary (H, L, LL), 8 Carbonaceous (CI, CM, CO, CV, CK, CR, CH, CB), 2 Enstatite (EH, EL) and R and K chondrites as described in more detail below.

1.3 Ordinary Chondrites

Ordinary chondrites are the most common among the chondritic meteorites. They are primarily composed of two main mineral groups: silicates and metals. The silicates consist of minerals such as olivine, pyroxene, and plagioclase feldspar, while the metal grains mainly include iron and nickel alloyed with minor amounts of other elements. These meteorites also contain small amounts of other minerals, including sulfides, phosphates and oxides.

To differentiate between the H, L, and LL groups of ordinary chondrites, several parameters are considered. Iron and magnesium concentrations in the silicates (e.g., olivine) are the primary discriminant, but several other factors such as metal abundances and chondrule size exhibit small, systematic variations among these groups. Also, abundances of siderophile elements serve as another useful means of distinguishing between the H, L, and LL groups. [Weisber at al., 2006]

H chondrites, also known as the High Iron group, are characterized by the presence of abundant metallic Fe-Ni (iron-nickel) grains dispersed within a fine-grained matrix of olivine, pyroxene, and plagioclase feldspar. H chondrites' olivine compositions are set as Fa20.8/Fs19.0 as the upper limit and around Fa16.0/Fs14.0 for the lower limit [Grossman and Rubin, White paper].

L chondrites, or the Low Iron group, exhibit a similar mineral composition to H chondrites but have a lower abundance of metallic Fe-Ni. Instead, and they possess larger chondrules. L chondrites have experienced varying degrees of thermal metamorphism and aqueous

alteration, indicating a more extensive history of parent body processes. The Fa22.0/Fs19.0 is set as the lower limit for L-chondrites [Grossman and Rubin, White paper]

LL chondrites, standing for the Low Iron - Low metal group, share similarities with L chondrites in terms of mineralogy and chondrule size. However, they have an even lower content of metallic Fe-Ni. The distinction between L and LL olivine compositions is less clear but it is suggested to be around Fa27/Fs23 [Grossman and Rubin, White paper].

When looking at the oxygen isotopic compositions, the Ordinary chondrites exhibit a distinct placement above the Terrestrial Fractionation (TF) line, clearly setting them apart from other chondrite groups like the Carbonaceous or Enstatite chondrites [eg. Mittlefehldt et al., 2008]. Generally, the H, L, and LL chondrites share similar petrologic characteristics and overlapping O-isotopic compositions, suggesting they are relatively closely related members of a larger group [Weisber at al., 2006].

1.4 Carbonaceous Chondrites

Carbonaceous chondrites are some of the rarest types of meteorites among all groups. Based on their bulk chemistry compositions and bulk oxygen compositions carbonaceous chondrites are divided into 8 different groups: CI, CM, CO, CR, CH, CB, CV and CK. In addition, several carbonaceous chondrites have been classified as ungrouped type (e.g., Tagish Lake meteorite). Except for the CI class that shows a lack of chondrules, the carbonaceous chondrites are generally composed of 30% of (sometimes altered) chondrules in a high abundance (70 vol.%) of matrix composed of phyllosilicates, tochilinite, carbonates, sulfides, and magnetite [Krot et al., 2005]. Their oxygen isotope

compositions lie near or just below the terrestrial fractionation line [eg., Mittlefehldt et al., 2008].

Despite the name “carbonaceous”, these types of meteorites contain relatively small carbon contents; CI class has the highest carbon content, 1 - 5 wt % but other classes like CO class have only minor carbon, 0.1 - 1.1 wt % [Macke et al., 2011].

Within the various groups of carbonaceous chondrites, the CI chondrites stand out as possessing the most primitive elemental compositions. “Primitive” implies that these compositions closely resemble that of the solar photosphere, providing a valuable insight into the composition of the earliest materials that contributed to the formation of our Solar System [Macke et al., 2011]. However, as for some other classes of carbonaceous chondrites like the CM, in the CIs the primary mineralogy and petrography were partially/completely altered by different stages of aqueous alteration on their parent asteroid/asteroids [Krot et al., 2005]. The degree of aqueous alteration for different meteorites is indicated by the petrologic type: type 2, low aqueous alteration, and type 1 strong aqueous alteration.

When considering spectra, carbonaceous chondrites encompass a collection of meteorites characterized by low reflectance. They contain abundant opaque dark components like carbon, microscopic metal and troilite particles. These opaque constituents significantly diminish reflectance, resulting in dark spectra with minimal absorption features. [Britt et al., 1992].

1.5 Enstatite chondrites

Enstatite chondrites, formed in highly reducing conditions in the nebula, are characterized by their unique mineralogy and mineral chemistry. They contain silica-poor silicates and Si-bearing metals, and elements that are typically lithophile in most meteorite groups (such as Mn, Mg, Ca, Na, K). Enstatite ($MgSiO_3$) is the dominant silicate mineral found in the chondrules of these meteorites [Weisber at al., 2006]. Olivine chondrules are rare and essentially absent in low petrologic types EH3 and EL3. Additionally, enstatite chondrites contain various uncommon sulfide, metal, and nitride phases that are not typically found in other chondrite groups. They are the only chondrites with oxygen isotopic compositions that plot along the Terrestrial Fractionation line and are close to the oxygen composition of Earth and the Moon [Clayton et al., 1984].

The E chondrites are further classified into EH and EL groups. The composition of the (Mg, Mn, Fe) S phase is a clear distinguishing factor between EH and EL chondrites. EH chondrites are more reduced compared to EL chondrites. The EH chondrites also have higher Si content (2-3 wt%) in the Fe,Ni-metal, while EL chondrites generally have less than 1.0 wt% Si in the metal. [Weisber et al., 2006]

1.6 Asteroids

Asteroids are divided into spectral classes based on albedo, slope, and absorption features in the 0.45-2.45 μm range. As of today, at least 24 different classes of asteroids have been observed in the main asteroid belt [e.g., DeMeo et al., 2009] (Figure 1.2).

S-Type asteroids show prominent 1 and 2 μm absorption features related to olivine and orthopyroxenes and they have been linked to the ordinary chondrites.

The carbonaceous chondrites have been linked with the low albedo and relatively featureless spectra of C and G-type asteroids. However, most of the CVs and COs chondrites show red slopes and albedos that put them into the K-type; most of the K-type asteroids are members of the Eos family. B type asteroids, very low albedo, have also been linked with carbonaceous-chondrite-like (CM-like) asteroids like 101955 Bennu.

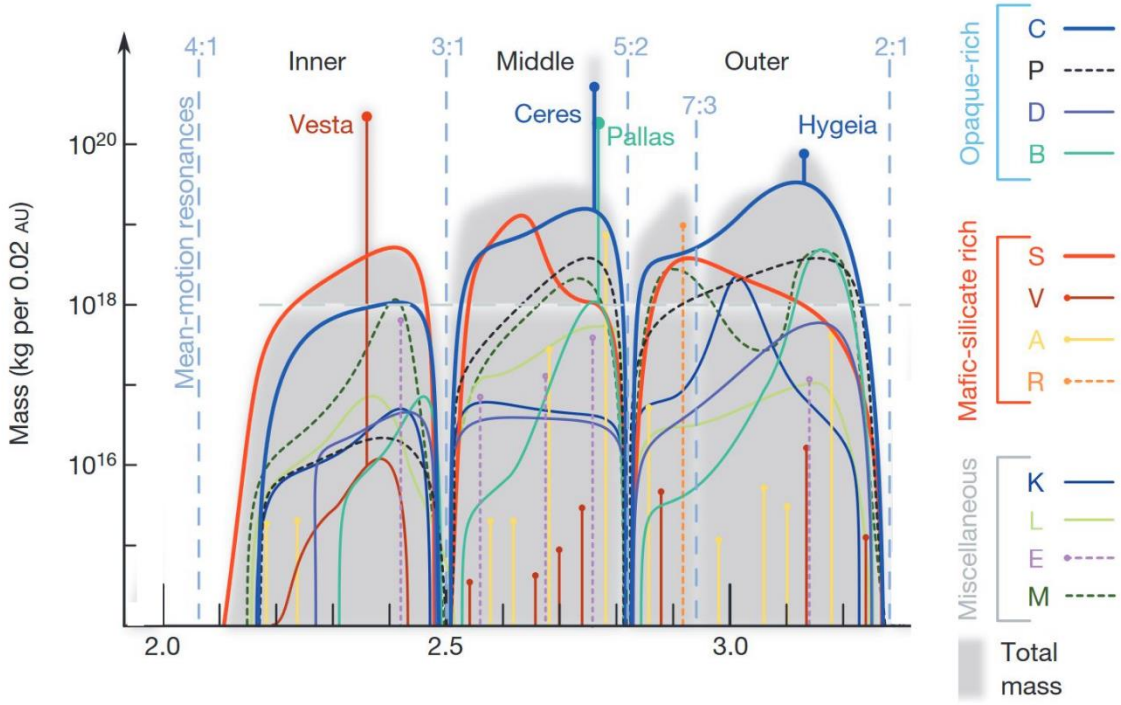

Figure 1.2: Asteroid Composition Map of the Main Asteroid Belt. The Y axis represent the distance from the Sun in Astronomical Units (AU). [Modified from DeMeo and Carry, 2014]

Even if carbonaceous chondrites represent just ≈ 3% of all the meteorites falling to the Earth the C-types asteroid are abundant in the near-Earth population [e.g. Mainzer et al., 2014] and in the main asteroid belt; they are much more abundant in the middle and outer asteroid belt than the inner asteroid belt [DeMeo and Carry, 2014]. The fact that carbonaceous meteorites are less abundant than expected from the C-type asteroid abundances in the main asteroid belt and near-Earth population, may reflect 1) relatively

low strengths that reduce their survivability in space; this is supported by the relatively short cosmic exposure ages for some of the carbonaceous chondrite classes like the CI and CM between 6 and 0.2 million years [e.g., Eugster, 2003]. However, the low recovery proportion also probably partly reflects 2) lower survivability during atmospheric entry due to lower strengths. Little is known about the strength of these meteorites to date.

Asteroids can be composed of a single intact body (Figure 1.3, A) or by a "rubble pile" (Figure 1.3, B) (the so-called rubble pile asteroids).

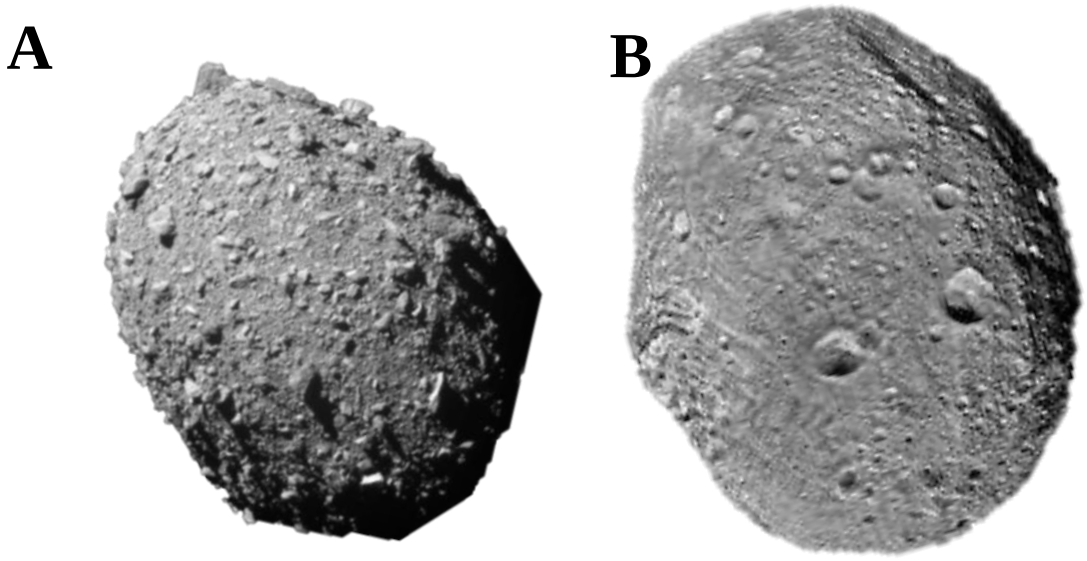

Figure 1.3: In Figure A, we observe the rubble-pile asteroid moonlet Dimorphos captured by the DART spacecraft just 11 seconds prior to impact, displaying a diameter of 160 m. The distinct features of Dimorphos in the image include its rugged, boulder-strewn surface and absence of finer materials. Figure B show a photograph of Vesta, a colossal single body asteroid measuring 525 km in diameter, representing one of the largest asteroids within the Solar System.

In the case of asteroids made by a single intact body, their physical properties like bulk density, grain density and Intraclast porosity will reflect those of their corresponding meteorite lithologies.

On other hand, the rubble pile asteroids are piles of rocks gravitationally bound together, rough surfaces with angular boulders littering the surface [e.g.,Walsh, 2018]. They are characterized by high interclast porosity (~40%) and low asteroid bulk density depending on the lithology/lithologies that compose them. Their formation is thought to result from reaccumulation of clasts following a catastrophic asteroid collision [Walsh, 2018]; more heterogeneity in terms of aggregate physical properties and compositions may be observed for these asteroids.

In general, objects with low porosity are uncommon. Apart from a few, most asteroids exhibit substantial porosity. There is a grouping of objects with porosities around 30%, while some objects exhibit much higher values; this numbers are considered total porosity (macro + micro porosity in former terminology). [e.g., Britt et al., 2003]

1.7 Asteroids sampled by spacecrafts

Just three asteroids have been sampled by spacecraft to date, 25143 Itokawa, 101955 Bennu and 162173 Ryugu.

Asteroid Itokawa

The Hayabusa spacecraft (from JAXA) performed two successful contacts with the surface of asteroid 25143 Itokawa, on November 20 and 26, 2005 (Figure 1.4). During these operations, the spacecraft collected fine grained particles from the asteroid's surface although the sampling mechanism didn’t trigger. Before sampling the asteroid, analysis

through reflectance spectrometry indicated that Itokawa has a mineralogy that is dominated by olivine and pyroxene. Moreover, based on its high olivine content and average spectral parameters Itokawa possessed a composition like that of an LL chondrite [Binzel et al., 2001].

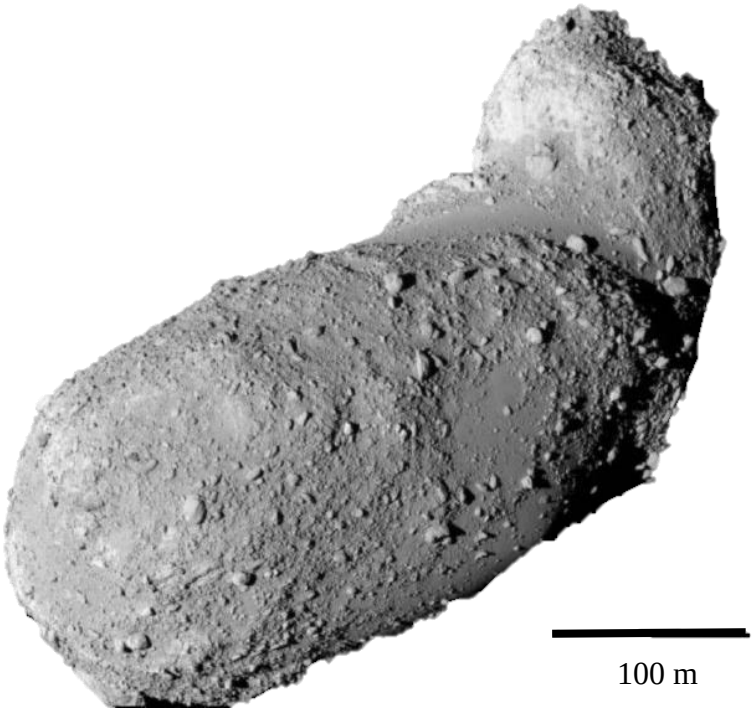

Figure 1.4: Image of Asteroid Itokawa from the Hayabusa spacecraft. [Modified from JAXA]

The primary mineral assemblage discovered in the collected sample grains comprises olivine, pyroxene, plagioclase, iron sulfide, and iron-nickel metal. By analyzing the oxygen isotope data and chemical compositions of the returned samples, Yurimoto et al. 2011, were able to determine that the material from Itokawa aligns with the classification of LL chondrites. This conclusive evidence is derived from the oxygen isotopic

composition of asteroid Itokawa, establishing a clear link between ordinary chondrites and S-type asteroids [Yurimoto et al., 2011].

Itokawa's surface can be categorized into two distinct terrains: rough terrain, characterized by numerous boulders, and smooth terrain, such as around the neck area and around the north polar region. Despite Itokawa's divided appearance, there is no significant variation in mineral composition across the entire asteroid's surface.

Itokawa has a bulk density of 1.9 g cm^3, which is notably low. Comparing Itokawa's composition to LL ordinary chondrites, which are considered reasonable analogs, and assigning an average bulk density of 3.2 g cm^3 for such chondrites, it is estimated that Itokawa has a interclast porosity of approximately 41%. [Fujiwara et al., 2006]

It is evident that Itokawa contains substantial empty space within its interior, so it is considered a rubble-pile asteroid.

Asteroid Bennu

NASA's Origins, Spectral Interpretation, Resource Identification and Security-Regolith Explorer (OSIRIS-REx) spacecraft arrived at the near-Earth asteroid 101955 Bennu in December 2018. Bennu is a low albedo B-type asteroid linked with the hydrated carbonaceous chondrites, CM type [Lauretta et al., 2019] (Figure 1.5); the OVIRS instrument on board of the OSIRIS-REx detected a near-infrared absorption feature near 2.7 µm typical for hydrated minerals, and thermal infrared spectral features that match those of the hydrated CM chondrites [Hamilton et al., 2019].

Bennu is a ≈ 500 m (maximum diameter) diamond shape asteroid, and it is the smallest object ever orbited by a spacecraft. The very low bulk density of 1.19 g/cm3 and the lack of either high surface slope or substantial topographic relief indicate that Bennu is a rubble-

pile asteroid [Walsh et al., 2019]: the surface is dominated by different sized boulders up to 56 meters long.

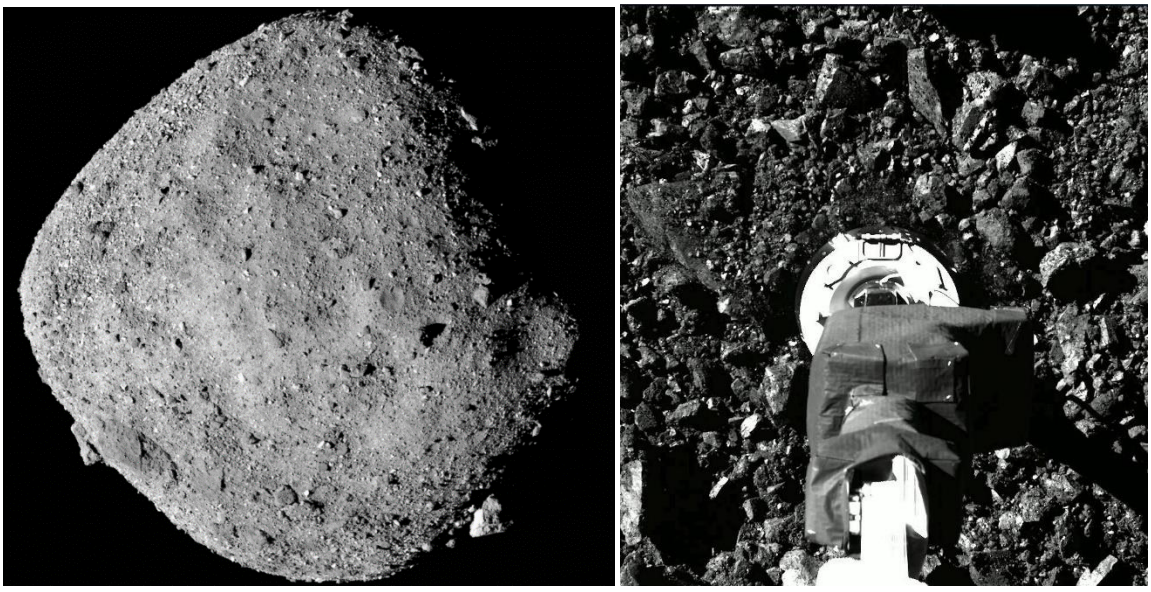

Figure 1.5: Figure A show asteroid Bennu pictured from the OSIRIS-REx spacecraft. Figure B shows the OSIRIS-REx sampling the targeted crater.

Bennu shows minor variations in albedo, spectral features, and colors [Walsh et al., 2019] between boulders confirming a heterogeneous and complex surface. The very high-resolution images of the surface of Bennu clearly show two distinct lithologies, a dark, low albedo and possibly weaker lithology and in contrast a relatively high albedo, light color, and possibly stronger lithology (Figure 1.6).

The dark boulders exhibit non-linear fractures, exfoliation-like fractures, that could be the result of the interaction between the fracture mechanism and their rock structure [Walsh et al., 2019]. The brighter boulders (7-15% albedo vs 4.5% average albedo of Bennu [Clark et al., 2019]) show multiple linear fractures that appear to split boulders into one or more pieces [Walsh et al., 2019]. Different mechanisms could be responsible for fracturing

boulders on the surface of Bennu like, thermal fracturing, large-scale impact events, micrometeoroid impacts, and solar wind ion implantation [Walsh et al., 2019; Clark et al., 2019].

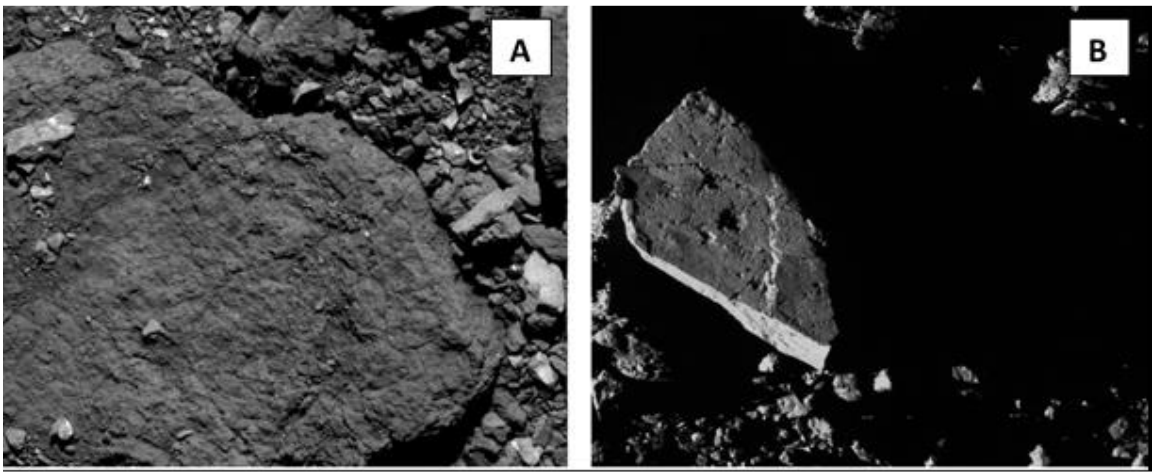

Figure 1.6: Figure 3: the figure shows a comparison between a dark, low albedo rough surfaced boulder (A) and brighter albedo, more angular shape, smooth surfaced boulder (B) on Bennu. [Images from OSIRIS-REx mission]

The OSIRIS-REx mission also detected particles with diameters from <1 to ~10 cm - diameter ejected from Bennu at speeds ranging from ~0.05 to > 3 m/s [Lauretta and Hergenrother et al., 2019], surprisingly revealing an active "geology". Some possible mechanisms responsible for the ejection events are thermal fracturing, volatile release through dehydration of phyllosilicates, and meteoroid impacts [Lauretta and Hergenrother et al., 2019]. Smaller events could be attributable to reimpacting particles.

The return capsule containing Bennu's samples is expected to land and be collected at the end of September 2023 in the Utah desert.

Asteroid Ryugu

JAXA's Hayabusa2 sample return mission arrived at asteroid Ryugu in June, 2018. Ryugu is a diamond shape ~ 1000 m (max diameter) rubble pile asteroid with a very low bulk density of 1.19 g/cm3 (same as Bennu) (Figure 1.7). It is one of the darkest objects of the Solar System with a very low visible geometric albedo (= 4.5 %) and spectral properties of the Cb-type carbonaceous asteroids. [Jaumann et al., 2019]

As for Bennu, also the NIRS3 instrument on board of Hayabusa2 detected a constant weak, narrow absorption feature centered near 2.7 µm all over the surface of the asteroid; the 2.7 µm features is relate to the presence of OH-bearing minerals. This band position is like the Mg-OH features observed for Mg-rich phyllosilicates such as serpentine or saponite which are observed in the primitive CI and CM chondrites [Kitazato et al., 2019].

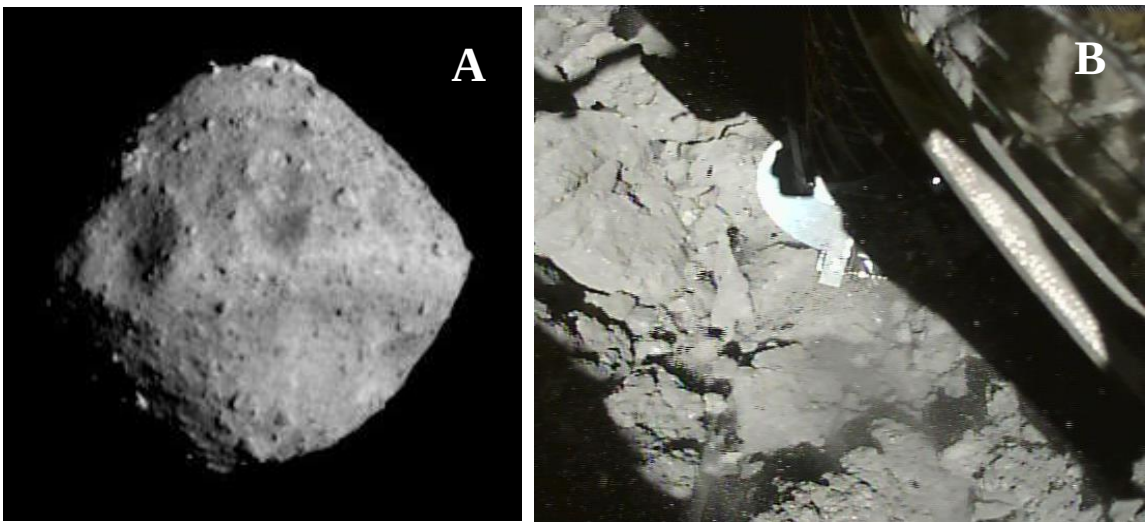

Figure 1.7: Figure A shows asteroid Ryugu imaged by the Hayabusa 2 spacecraft. The figure B is showing the spacecraft sampling the asteroid.

As for Bennu, on Ryugu, different types of clasts have been observed showing a heterogeneous surface and possibly different lithologies. Types 1 are rugged and dark

boulders with non-linear fractures, like the dark boulders on Bennu. Types 2 are bright and smooth boulders that show parallel, closely spaced, fractures. Types 3 are bright and motted boulders that do not clearly show any fracture/layers. Type 4 is the largest boulder on Ryugu, it is bright and shows very sharp edges and possibly linear fractures. [Sugita et al., 2019] (Figure 1.8).

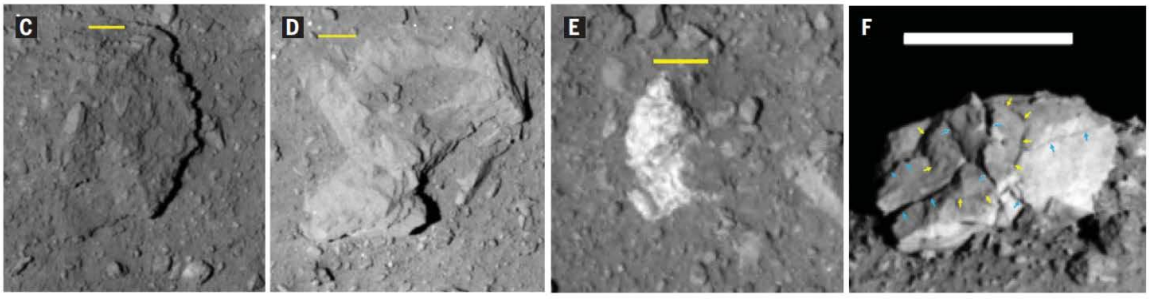

Figure 1.8: the figure shows the different boulder types on Ryugu. Type 1 (C), type 2 (D), type 3 (E), type 4 (F). The yellow and white scale bars are 10 and 100 m respectively. [Modified from Sugita et al., 2019]

The returned samples confirmed that the asteroid composition is like those of carbonaceous chondrite meteorites, particularly the CI (Ivuna-type) group but more primitive, closely resembling the composition of the Sun's photosphere. The samples also consist predominantly of minerals formed in aqueous fluid on their parent planetesimal. [Yokoyama at el., 2023]

Synchrotron X-ray computed tomography (SR-CT) has been employed to examine the samples, providing further insights. Internal cracks, predominantly irregular in shape, have been observed in most of the samples. The bulk density of these samples falls within the range of 1.7 to 1.9 g/cm3. These densities surpass the measured density of asteroid Ryugu, indicating a substantial level of interclast porosity [Nakamura et al., 2022].

In comparison, the average bulk densities of CI and CM chondrite meteorites are 2.12 and 2.21 g/cm^3, respectively. The lowest recorded density for a CI chondrite is 1.98 g/cm^3, implying that the Ryugu samples exhibit higher porosity than CI chondrites [Nakamura et al., 2022]. However, the low density recorded for the Tagish Lake meteorite (classified as C-ungrouped and sharing a similar composition with the CM and CI groups) has not been considered. Relatively pristine Tagish Lake meteorites exhibited a weighted mean bulk density of 1.64 g/cm^3 [Hildebrand et al. in 2006]. Tagish Lake's density may indicate that measured densities and intraclast porosities of CI meteorites have been affected by terrestrial weathering. The Tagish Lake bulk density measurement corresponds with a mean weighted mean intraclast porosity of 40% suggesting that Ryugu's intraclast porosity will be less than this value.

It is also crucial to consider that the densities measured for Ryugu's samples were obtained from very small samples, on the order of a few millimeters or less. Therefore, these measurements may not accurately reflect the density at larger sample sizes, which are typically used to determine the densities of meteorites.

1.8 Physical, Elastic and Mechanical Properties of Meteorites

Over the past few decades, significant progress has been made in understanding the nature of meteorites, their origins, and their arrival on Earth. However, much of the laboratory research and modeling efforts have primarily emphasized chemical properties while neglecting detailed exploration of the physical properties. The understanding of porosity, seismic velocities and density has grown for meteorites [Britt and Consolmagno, 2003, Macke et al., 2011; Ibrahim, 2012; Flynn et al., 2017, Otrowsky and Bryson, 2019],

however the mechanical and elastic properties are still very poorly constrained [e.g., Pohl and Britt, 2020].

The growth in understanding the physical properties, like porosity and density of meteorites has been set in motion by different factors. One is the development of new techniques and tools that required less materials and allow for more non-destructive analysis. 3D laser scanning, for example, that we also used in this study, is a game-changer for measuring density of irregular samples without the need to reshape them reducing material loss. [e.g., Otrowsky and Bryson, 2019]

In recent years, there has been a significant surge in interest focused on the mechanical and elastic properties of meteorites. One of the primary motivations for the increased interest into the mechanical and elastic properties of meteorites is their pivotal role in advancing our understanding of asteroids. Asteroids are of immense interest due to their potential impact hazard to Earth and their scientific value in understanding the early solar system. By studying meteorites properties, we can help to refine models that predict asteroids behavior and potential impact scenarios.

Furthermore, the mechanical and elastic properties of meteorites have direct implications for the planning and execution of planetary missions. Notable missions like Hayabusa 2, OSIRIS-REx, and DART are prime examples of how understanding these properties is essential for successfully predicting mission outcomes.

The current state of research into the mechanical and elastic properties of meteorites reveals a notable gap in systematic and comprehensive studies within the existing literature. Currently, fewer than ten meteorite groups have undergone measurements for both tensile and compressive strength. Among these, only two groups pertain to carbonaceous

chondrites (with three groups specifically focused on tensile strength). However, the existing data remains disjointed and dispersed throughout a multitude of research papers and publications.

A fundamental problem arises from the lack of the use of standardized techniques that has resulted in variations in sample sizes, dimension ratios, and strain rates across the literature. Consequently, this diversity in methodologies has diminished the reliability and ease of cross-referencing data between different sources and terrestrial rocks literature [e.g., Pohl and Britt, 2019].

Another concern when assessing the strength of meteorites arises when considering that of the few measurements existing, a big portion comes from finds. Finds are widely recognized in literature to have undergone substantial weathering, which has had a noticeable impact on their properties [e.g., Otrowsky and Bryson, 2019]. Finds are highly unlikely to accurately represent the original physical, mechanical, and elastic properties. As a result, this situation further diminishes the already limited pool of reliable existing data.

Several papers in the field also lack precision when it comes to defining certain properties. A common example is the ambiguity surrounding compressive strength, which can be either the ultimate strength or the stress observed at the point of failure. Another frequently ambiguous definitions found in literature are the definitions of porosity. Various definitions of porosity exist, each serving different purposes, however for planetary science literature these definitions are not always well described as elaborated upon in the discussion chapter of this thesis.

An additional issue pertains to the oversight in evaluating heterogeneities within meteorites. It has been established that meteorites exhibit pronounced variations in their properties. However, not enough papers evaluate the properties variations contingent upon the orientation of applied stress (e.g., strength, seismic velocities). As revealed by this study, the elastic and mechanical properties of meteorites can diverge, not only from sample to sample, but also when measured along distinct directions.

Moreover, establishing connections between porosity, seismic velocities, and strength is pivotal in aiding the prediction and comprehension of these properties on a parent body scale. Regrettably, the current literature lacks studies that have comprehensively assessed an entire set of properties for the same samples. Given the inherent heterogeneities within meteorites, deriving dependable correlations between their properties becomes very difficult from existing literature.

Lastly, essential properties such as shear strength or hardness have yet to be quantified for meteorites.

1.9 The aim of this study

The primary objective of this project is to comprehensively measure the physical, mechanical, and elastic properties of chondrite lithologies, which are currently poorly characterized, to better understand meteorites and parent asteroids' deformational behaviors. To achieve this, a combination of nondestructive and destructive analysis techniques has been employed.

The properties measured include porosity, bulk density, grain density, seismic velocity (both P and S waves), Unconfined Compressive Strength, Direct Shear Strength, Hardness

(HLD), Elastic dynamic elastic moduli (dynamic Young's modulus, Shear modulus, Bulk modulus, and Poisson's ratio), Coefficient of Restitution, Static Young's Modulus, the Proportional Limit and Elemental Compositions.

Measuring these properties accurately presented significant challenges, particularly due to the small size of the samples (ranging from 2.5 mm to 2 cm) and sometimes their intrinsic weakness. Consequently, significant efforts have been devoted in adapting existing methodologies (for a detailed description of the adapted methodologies, please refer to the Methods chapter of this study) to facilitate these measurements and to comply with standards of the relevant research community (in this case with ASTM International Standards).

In addition, this study seeks to reinforce use of existing measuring conventions/standards within the planetary science community. By doing so, it will facilitate improved cross-referencing of data in future research and provide a valuable contextual framework for interpreting samples returned from asteroids. This will pave the way for more comprehensive investigations and meaningful insights into the composition and nature of asteroids and all the phenomena operating on asteroids that involve mechanical and elastic stresses (eg, impact cratering, asteroid formations and disruptions, asteroid active geology). While extensive studies have been conducted on the mechanical and elastic properties of terrestrial rocks, it is important to recognize that most meteorites exhibit significant distinct structural differences. Meteorites can consist of metal grains of varying sizes embedded in a fine matrix of silicates, while others may primarily consist of iron and nickel. Additionally, some meteorites exhibit a combination of metal and silicate grains in an extremely porous matrix, with intraclast porosities reaching up to 40%, as seen in the case

of Tagish Lake meteorite. Finding terrestrial analogs that closely resemble these unique structures and porosities is challenging, underscoring the need for an improved database in this regard.

Another objective of this study is to explore the relations among various properties in meteorites by conducting a comprehensive suite of measurements on each sample. Previous literature has not adequately addressed this aspect, resulting in sparse data and a reduced level of confidence in understanding the relationships between these properties. By undertaking this research, I aim to bridge these knowledge gaps and enhance our understanding of the intricate relationships among meteorite properties.

1.10 Why measuring these properties?

Measuring the properties of meteorites is significant for several reasons. When two objects physically interact, the interaction generates stress, and the resulting stress response is dependent on the material's physical, elastic, and mechanical properties. Therefore, understanding and modeling various phenomena involving the physical interaction of two or more objects require these properties as essential inputs.

This systematic study on the elastic and mechanical properties chondrites' lithologies provides constraints about survivability of the weak meteorites in space and during atmospheric entry and will help us to address questions like:

Is Tagish Lake representative of the weakest material to survive atmospheric entry? Will this strength number help us better understand how many parent asteroids are represented by our meteorite collections? Do meteorites represent just the stronger part of the meteoroid?

As suggested by the abundance of C-type asteroids in the main asteroid belt and by the low cosmic exposure ages of some carbonaceous chondrites, carbonaceous meteorites may represent some of the weakest asteroidal material in the Solar System. Physical properties, particularly strength, play a critical role in determining meteoroid survivability during entry and impact.

The physical properties of the hydrated carbonaceous chondrites (like CM and Tagish Lake) will help to constrain the current state and evolution of the primitive asteroids Bennu and Ryugu and help us to answer some important questions like:

What are some of the physical properties of asteroids Bennu and Ryugu? What is causing the particle ejection events detected by the OSIRIS-REx spacecraft? What are the relations between data of physical properties measured from the spacecraft's observation and laboratory measurements? What are the physical and mechanical processes that create regolith on the surface of asteroids?

By integrating measurements of bulk density, grain density, and intraclast porosity, along with recent data obtained from the sampled asteroids Ryugu and Bennu, we can enhance our understanding of these properties on a larger asteroid scale. Furthermore, this information has the potential to provide insights into the internal structure of asteroids.

Thermal properties influenced by the physical properties of the primitive carbonaceous chondrites are required inputs to model Yarkovsky forces, the YORP effect [eg., Bottke et al., 2001; Deo and Kushvah, 2017] and to understand the dynamical evolution of asteroids in the solar system; Asteroid Bennu is a potential hazardous object that could hit the Earth within the next 200 years, modeling Yarkovsky and YORP effect will allow us to better evaluate the risk of a potential impact.

Physical properties are also useful in the planning of asteroid spacecraft missions with a sampling component.

Asteroid sample return missions like OSIRIS-REx required before launch a series of tests including testing the TAGSAM instrument (sampling device on board of the OSIRIS-REx spacecraft) on a simulated asteroid regolith [Bierhaus et al., 2018]. This asteroid regolith simulant, the HCCL-1 (Hydrated Carbonaceous Chondrite Lithologies - 1), was designed and created at the University of Calgary in order to simulate the density, porosity, strength, elastic and magnetic properties to be encountered on Bennu [e.g. Hildebrand et al., 2015; Bierhaus et al., 2018]; without knowledge of the mineralogical properties of the meteorites this would have not been possible. A deep understanding of asteroidal material will allow us to better refine future sampling missions.

Understanding the mechanical and physical properties of carbonaceous chondrites not only provides valuable context for samples returned from Ryugu and (soon) Bennu but also serves as a crucial link for predicting the mechanical and elastic properties of their parent bodies.

On September 26, 2022, at 23:14 UTC, the NASA Double Asteroid Redirection Test (DART) mission successfully executed a kinetic impact on Dimorphos, the satellite of the binary asteroid (65803) Didymos. This mission served as a planetary defense test and marked the first-ever hypervelocity impact experiment conducted on an asteroid, considering the size and velocity scales relevant to planetary defense. The primary objective of the DART mission was to validate the effectiveness of kinetic impact as a method for deflecting asteroids. [Cheng et al., 2023]

To effectively divert asteroids that pose potential hazards, it is crucial to consider various significant factors, including density, inter- and intraclast porosities, and strength, that in the case of the DART mission, were unknown [eg., Cheng et al., 2016; Flynn et al., 2020]. These factors play a pivotal role in determining the optimal approach for deflecting such asteroids. Altering target characteristics such as, strength, porosities, rotational state, and shape, researchers observed corresponding variations in the response of asteroids: for example, higher porosities result in higher deflection velocities due to reduced target masses for asteroids of a constant size. Additionally, interclast porosity reduces the risk of disruption for kinetic impacts approaching the threshold of disruption. [eg., Bruck Syal et al., 2016; Kumamoto et al., 2022]

DART is just the start. Soon more and more mission will be dedicated to planetary defense [eg., Michel et al., 2022] and knowledge on asteroid material properties will be crucial.

1.11 Brief contextual description of the meteorites used for this study

Buzzard Coulee (H4)

On the evening of November 20, 2008, a large fireball was widely observed across Alberta, Saskatchewan, and Manitoba. Meteorites were recovered in Buzzard Coulee, Saskatchewan (Figure 1.9). Numerous un-calibrated cameras documented the intense descent of this approximately 2-meter boulder. The resulting orbit reveals that the meteoroid was previously in a near-Earth Apollo-type. [Milley et al., 2009]

Based on the compositions of orthopyroxene and olivine, Buzzard Coulee is classified as an H-group chondrite. Chondrules are distinguishable, but not sharply defined. [Huston et al., 2009]

Some of Buzzard Coulee meteorites were recovered very fast (less than a month), and much of it was recovered within a year, making it an extremely fresh fall that is perfectly suited for this study.

Figure 1.9: The heaviest Buzzard Coulee meteorite on record weighs 13 kg. As depicted in the image, this meteorite created an indentation upon impact with the ground before rebounding. [photo of Bruce McCurdy, ESSF / RASC]

Golden (L/LL)

On October 3, 2021, a bright fireball was witnessed in eastern British Columbia, western Alberta, northern Idaho, and Washington. It resulted in the discovery of two meteorite

specimens (1270 and 919 g) near Golden, British Columbia (Figure 1.10). Both specimens exhibited fusion crust and contained chondrules.

Petrographic analysis revealed chondrules, metal grains, and sulfide in the matrix. Geochemical analysis classified the meteorite as an ordinary chondrite of the L/LL5 group, showing signs of light shock [Brown et al., 2023 – submitted].

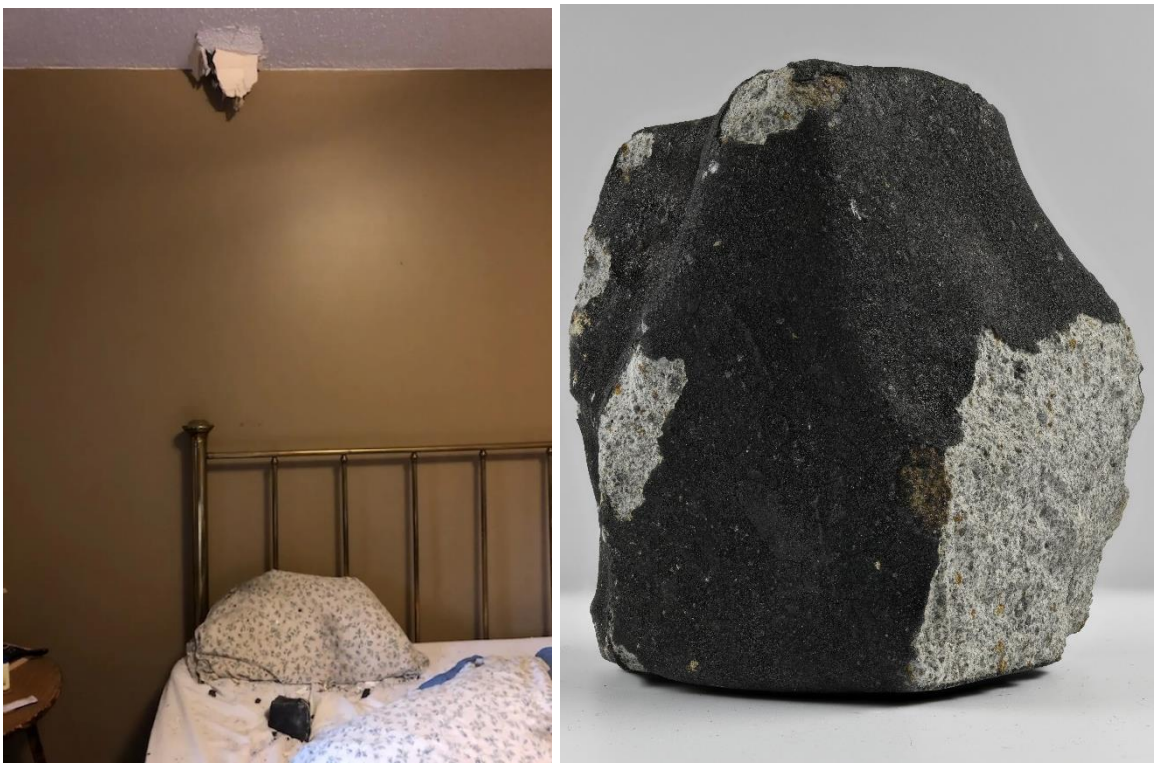

Figure 1.10: On the left side, you can observe the largest golden meteorite weighing 1.2 kg, which penetrated the roof of a residence in Golden at 11 pm on October 3rd, 2021. On the right, the smaller meteorite weighing 919 g was found a week later and serves as the subject of investigation in this study.

One of the largest meteorites to date crashed through the roof of a residence in Golden, leaving a hole in the ceiling. Surprisingly, it was discovered resting beneath a bed pillow (Figure 1.10). This event marks one of the most recent and significant meteorite falls with

the specimen being exceptionally fresh. The second meteorite, used for this study, was found on a street less than a week after the fall.

Murchison (CM)

On a clear morning, specifically on September 28, 1969, the Murchison meteorite made its descent shortly before 11:00 a.m. Despite the daylight conditions, this significant event of was observed by many in the region. [Halliday and McIntosh, 1990]

The Murchison chondrite has gained extensive attention as one of the most extensively researched meteorites and has become a benchmark for studies in extraterrestrial organic chemistry [eg., Schmitt-Kopplin et al, 2009]. The carbon content of the Murchison meteorite, specifically more than 70% of it, has been categorized as insoluble organic matter with macromolecular properties. This organic matter exhibits a wide range of organic molecules, with over 500 structures identified. Many of these structures resemble known biomolecules such as amino acids. [Schmitt-Kopplin et al, 2009]

This is possible because its quick recovery and lacking terrestrial weathering [Zolensky and Gooding, 1989] making it one of the least altered carbonaceous meteorites ever recovered.

Based on the petrographic and mineralogical characteristic, Murchison meteorite is classified as CM 2.5 suggesting that its primary lithology underwent a relatively uniform and low level of aqueous alteration [Rubin et al., 2007].

Murchison consists of fine-grained Fe-rich septechlorite, black matrix with prominent white inclusions (0.5 to 5 mm) and rare chondrules (Figure 1.11). The matrix is composed mainly by olivine, pyroxene, and other minor phases (like calcite, spinel and pentlandite). [Fuchs and Jensen, 1970]

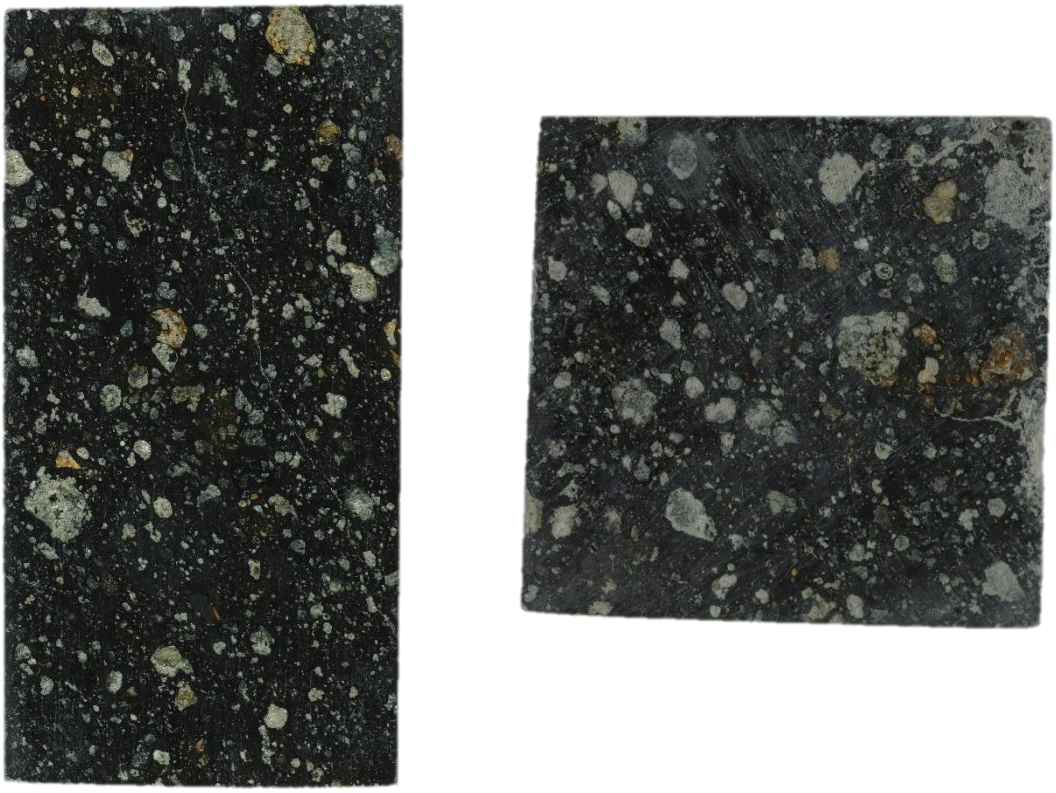

Figure 1.11: the photo shows 2 sides of a cuboid of Murchison used in this study.

Tagish Lake (C-Ungrouped)

On January 18, 2000, a meteorite known as the Tagish Lake meteorite produced a spectacular fireball. This event was notable for its exceptional brightness and was observed during twilight across the Yukon and Northwest territories, British Columbia, and Alaska. It has been estimated that the meteoroid had an entry mass of approximately 2×10^5 kg which corresponds to a pre-atmospheric radius of 4 to 6 meters [Brown et al., 2000].

Figure 1.11: The image displays a Tagish Lake meteorite, chosen for the purposes of this research. The markings along the flat surface are results of cutting the sample using a diamond wire saw.

The meteorites from this event were discovered in a mountainous region in the northwestern part of British Columbia. The initially recovered meteorites were promptly collected from the frozen surface of Tagish Lake by a local resident. However, the meteorites used for the specific study mentioned in this context were gathered from the lake in April 2001, after the snow had melted [Hildebrand et al., 2006].

The Tagish Lake meteorite belongs to the category of type 2 carbonaceous chondrites. While it shares similarities with the CI and CM chondrite groups, it is distinct from both and thus classified as a C2-ungrouped meteorite. This meteorite contains a significant amount of phyllosilicates and sparse chondrules, with common olivine grains dispersed in the matrix (Figure 1.12). It is characterized as a breccia, exhibiting at least two distinct

lithologies: a predominant carbonate-poor lithology and a less abundant carbonate-rich lithology. [Zolensky et al., 2002]

The Tagish Lake meteorite is considered one of the most primitive and physically fragile meteorites ever to have fallen to Earth [Hildebrand et al., 2006]. It represents a potential extreme in terms of low strength for surviving atmospheric entry.

Moss (CO)

The Moss meteor was observed on July 14, 2006, during local daylight time in South Norway. The event was accompanied by a loud explosion and rumbling sounds. At least five fragments were witnessed falling. Shortly after, a small meteorite was heard landing on an aluminum sheet and was subsequently recovered by a local resident. Other fragments were recovered in the region, some had hit a roof and other hit a fence and a tree (Figure 1.12). [Bilet and Roaldset, 2013]

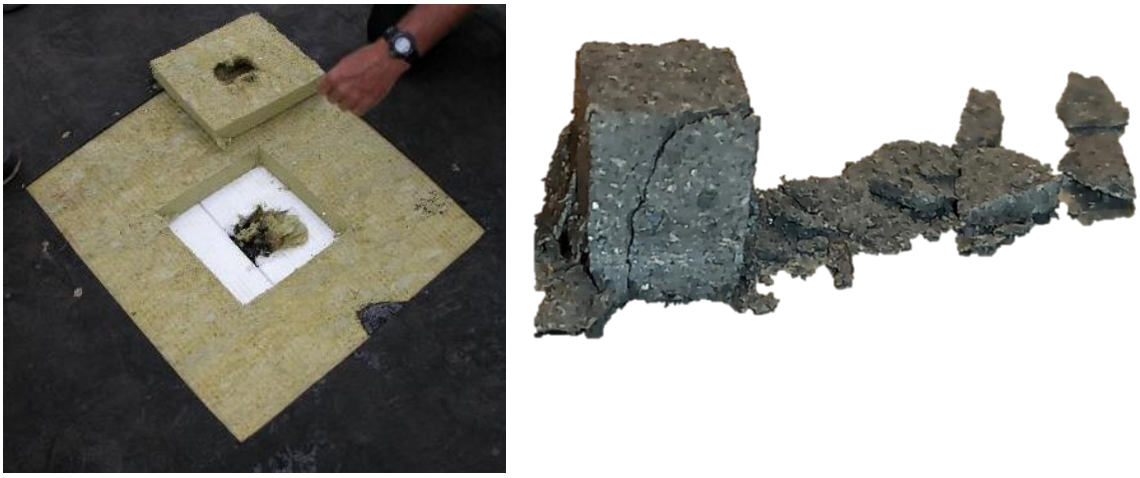

Figure 1.12: The image on the left shows the damage left on the roof of a home hit but one of the Moss meteorites. The figure on the right shows on of cuboids of Moss after a compression test.

The Moss meteorite is classified as a CO carbonaceous chondrite. It is characterized by an abundance of small chondrules, olivine aggregates, and refractory inclusions embedded in a gray matrix. The matrix exhibits mild recrystallization and is low in sulfur content. Additionally, the olivine in the matrix shares a similar composition with the olivine found in fine-grained chondrules and inclusions [Connolly et al., 2007].

In comparison to the other carbonaceous meteorites chosen for this study (Murchison and Tagish Lake), Moss has not experienced hydration processes on its parent asteroid.

The remarkably quick recovery of the Moss meteorites renders it an ideal candidate for the purposes of this study.

Abee (EH)

On June 9th, 1952, approximately 80 km north of Edmonton near Abee in Alberta, a very bright fireball was observed. Eyewitnesses were astounded by the fireball's brilliance, describing it as significantly brighter than the Moon. The fireball had a relatively consistent brightness with only minor flaring indicating a relatively strong lithology. A few days later, a local farmer found a large hole, measuring around 1.5 meters in depth and 0.7 meters in diameter, within his freshly seeded wheat field. Intrigued by this discovery, the farmer shared the information with his neighbor, a local teacher. Intrigued also by to the recent fireball sighting, the teacher assembled a group of students and commenced an excavation

of the hole. Their efforts uncovered the impressive Abee meteorite, weighing a staggering 107 kilograms (Figure 1.13). [Griffin et al., 1991]

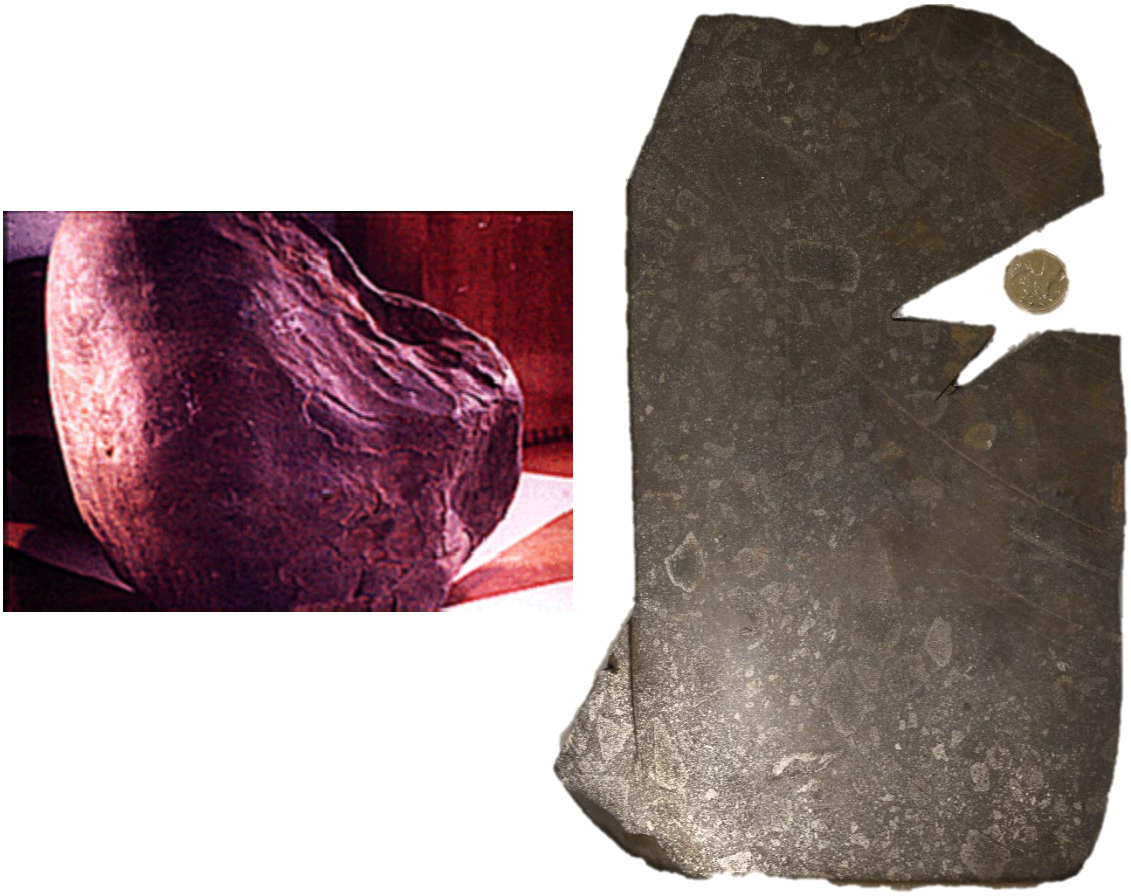

Figure 1.12: The left-side picture presents the initial Abee meteorite after its retrieval [photo from the Newbrook Historical Society]. Meanwhile, the right-side photo portrays a section of Abee meteorite, from which the cuboids utilized in this study were cut. The image on the right also reveals some angular breccia clasts surrounded by light gray rims.

The Abee meteorite has been classified as an EH chondrite impact-melt breccia (Figure 1.13). It is composed of various components, including clasts (mm to cm size) that are often surrounded by metallic Fe and Ni, dark inclusions, and a matrix. These clasts and the

matrix have undergone thorough thermal metamorphism, as indicated by their consistent mineral compositions. [Rubin and Keil, 1983]

The Abee breccia mainly consists of approximately 50% irregularly shaped clasts ranging in size from 1 mm to 6 cm and 50% matrix. The biggest clast found measured 14 × 22 cm. Both the clasts and matrix contain kamacite globules ranging from 0.1 to 1 mm in size, as well as kamacite-rich nodules with a maximum dimension of 11 mm. Many of the clasts are also surrounded by millimeter-thick kamacite-rich rims that separate them from the matrix. [Rubin and Scott, 1997]

Due to its brecciated texture, indicated strength, and the quick recovery, Abee is an ideal candidate for studying the relationship between breccia texture and elastic and mechanical properties.

2: METHODS

The relative lack of physical property measurements of meteorites (particularly carbonaceous chondrites) it is mostly due to 1) their rarity and 2) relatively large sample test requirements for some measurements and 3) concern about sample contamination. This study involved both destructive and nondestructive analysis. For the above reasons, a lot of attention has been dedicated to sample handling, minimizing contamination and careful recovery of the material left after each test. In this study we decided to only examine chondrite falls. Recovery of falls are usually well documented, allowing us to constrain the terrestrial weathering time and curation conditions. While some meteorite finds might be unique samples, their unconstrained exposure to terrestrial weathering for undetermined lengths of time reduces the level of confidence that their original physical property state has not been altered [e.g., Ibrahim, 2012]. For our tests we conformed with ASTM International (American Standards for Testing Materials International) protocols and procedures whenever possible; Appendix A has a list of ASTM Int. publications consulted. The order of taking measurements is the same as the description order in the next sections. All the samples were out-gassed overnight in vacuum (to reduce potential effects from absorbed water) before testing at ambient conditions.

2.1 Sample Preparation and Curation

Original meteorite samples are stored in cabinets placed in a clean room: the cabinets are purged with nitrogen (using a nitrogen separator, Peak Scientific Solaris 10) to reduce samples' oxidation and weathering.

Different portions of irregular (often as recovered) meteorite samples were cut into regular shapes using a diamond wire saw (Well Diamond Wire Saws, Model 3032-4) and a rotary

blade saw (Buehler IsoMet Low Speed Saw) depending on material cutting behavior; some samples tend to crumble if cut with the use of the blade saw. To minimize sample contamination and modification during cutting, no lubricating fluid was used in favor of air cooling of the wire/blade (this reduces the heating of the saw preventing wire breaking or blade overheating). Occasionally, for some samples (<15% Porosity) we sprayed alcohol during cuts on the blade to reduce the risk of blade damage and to reduce the cutting time. The cutting time varied from sample to sample but in general it took between twenty minutes to four hours for a single cut depending on lithology and size.

There are many reasons why such a significant amount of time was needed to cut our samples; 1) we do not use coolant fluid so a slow cut is needed to avoid overheating of the wire/blade; 2) some of our samples are among the weakest meteorites/rocks (e.g. Tagish Lake) and we have to reduce the force of the blade/wire applied on samples (this seems to reduce surface plucking/fracturing); 3) a lot of time is dedicated to mounting the sample on the holders to obtain parallel surfaces (parallel surfaces are required to maintain a near-perfect alignment with the platens of our compression machine).

The diameters of the diamond wire we used are 0.13 and 0.3 mm to reduce mass loss during cuts. The wire saw operated in a laminar flow bench to minimize airborne particle contamination, while the blade saw was operated within a fume hood. Aluminum foil was placed below the wire saw to recover fragments and dust formed during the cuts. Different wires and blades were assigned to cut different meteorites samples to avoid cross-contamination. The prepared cubes and cuboids were then stored in glass vials; all cutting operations with the wire saw are recorded in a dedicated laboratory notebook.

After obtaining regular shapes (cubes or cuboids), the samples were polished using a 1000 or 2000 grit (typically silica carbide) sandpaper and a custom-made sample holder (designed by and modified based upon "use experience" by the University of Calgary machine shop, Figure 2.1); this allowed a better coupling of the samples with test equipment (e.g. for measurements of volume, hardness, seismic velocities), and ensured alignment with platen surfaces in strength tests).

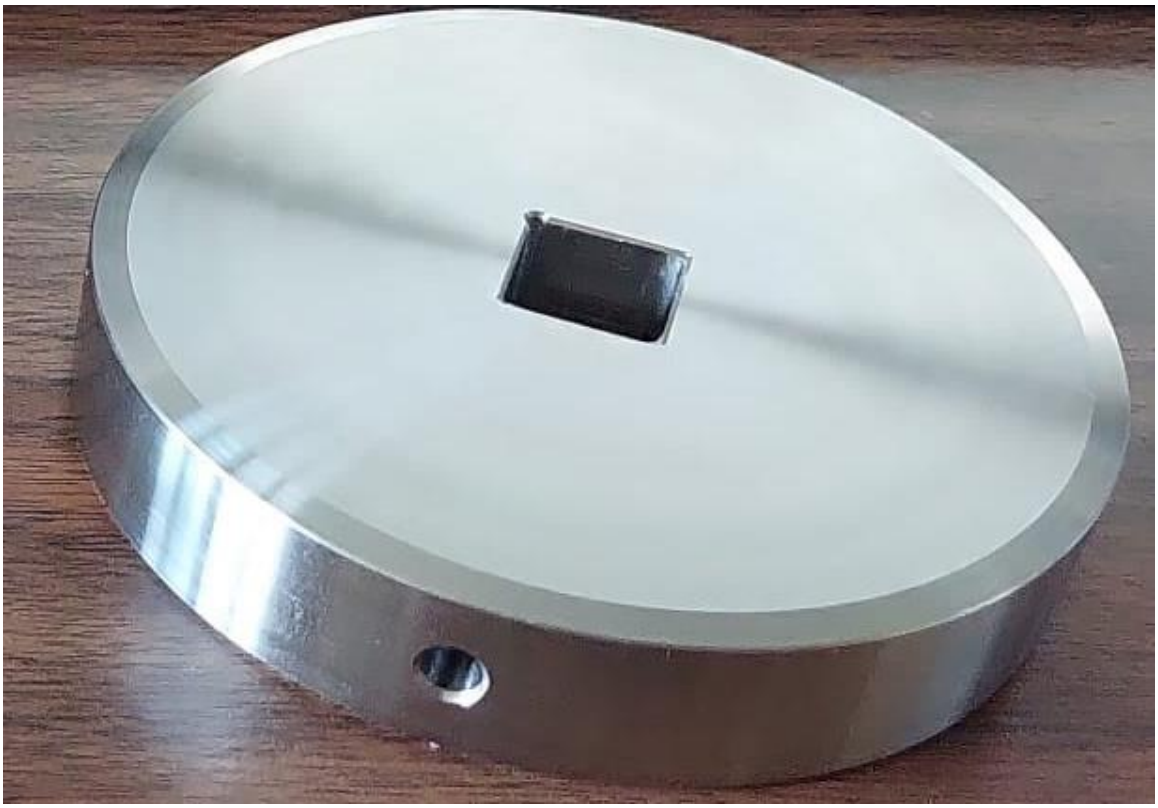

Figure 2.1: Photo of the custom-made holder for polishing parallel surfaces. The sample is placed in the central hole and secured using screws. The sample is then lowered in very small increments until the entire surface is uniformly polished. Once the first surface is uniform, the sample inside the hole is flipped, and the process is repeated.

2.2 Dimensions and Bulk Density (ρ_b)

The dimensions of the cuboids (Figure 2.2) were determined using a stainless-steel "jawed" digital caliper as they varied based on the shape, conditions, and volume of the original meteorite sample; fractured areas of the original sample were excluded to the extent possible. The samples' mass was measured with a digital mass balance. The volume of original (irregular) meteorite samples were calculated using a desktop laser scanner (NextEngine Desktop 3D Scanner Model 2020i); this method tends to overestimate the volume by 2% [Ghanizadeh A. et al., 2018] so a correction is needed (by decreasing the volume of 2%). From the volume and the weight, the bulk density (ρ_b) was:

$$\rho_b = \frac{W}{V_s}$$

Where W = weight and V_s = volume of the sample.

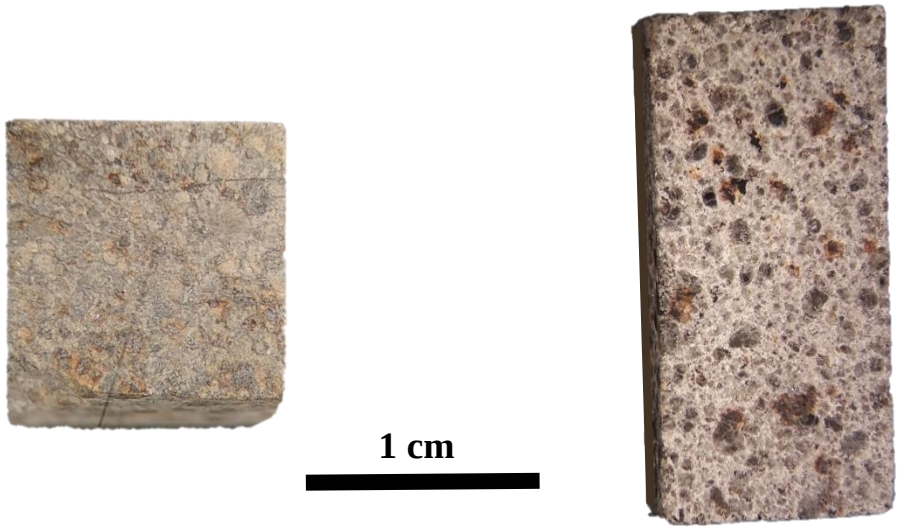

Figure 2.2: example of a Buzzard Coulee cube (on the left) and a cuboid (on the right) of Golden meteorite.

2.3 Porosity ($\emptyset$) and Grain Density (ρ_g)

Porosity is defined as:

$$\emptyset = \frac{V_p}{V_b} = \frac{V_p}{V_p + V_m}$$

Where V_p= Pores Volume, V_b= Bulk Volume and V_m= Grain Volume. For this study we measured porosity using two helium gas (helium 99.9999%) pycnometers (Quantachrome Instruments Multipyc, model: MVP-D160-E, and Ultrapyc 5000 Micro). This technique measures the Effective Porosity ($\emptyset_e$) or the connected porosity; to measure the Total Porosity ($\emptyset_t$) (whether connected or not) the samples need to be first crushed to the smallest pore size to allow opening of the pores. A brief schematic of the instrument is shown in Figure 2.3.

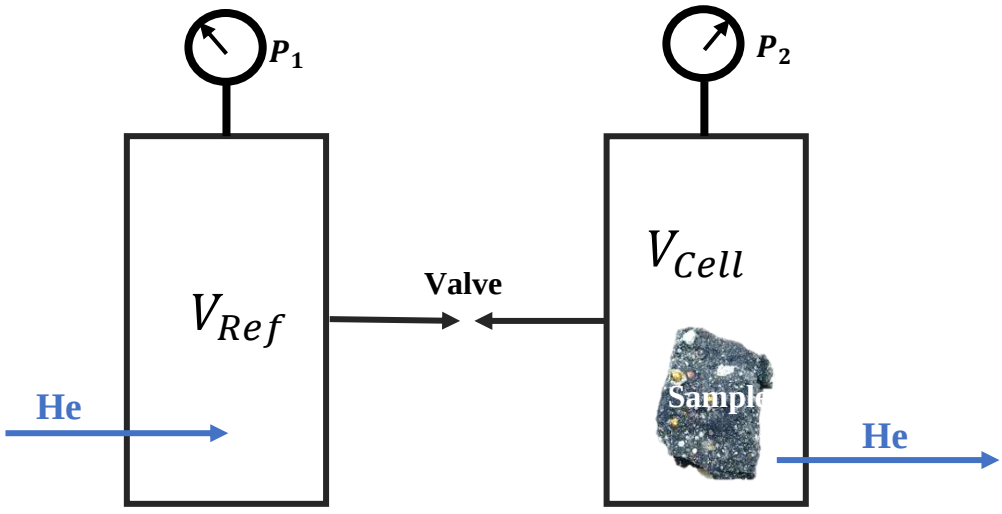

Figure 2.3: Helium is first flushed into a cell of reference of know volume (V_{Ref}) at a certain pressure (P_1). In the second stage, the valve is open to allow helium to flow into a second cell (V_{cell}). After the pressure is equilibrated (P_2), the Boyle's Law is used to measure the matrix/grain volume (V_m) of the sample.

The technique allows us to measure the matrix/grain volume (V_m) using the Boyle's Law:

$$P_1 V_{Ref} = P_2 V_{Cell}$$

From this equation we can derive the V_m as:

$$V_m = V_{Cell} - V_{Ref} * ({}^{P_1}/_{P_2} - 1)$$

From V_m we measure ρ_g as:

$$\rho_g = \frac{W}{V_m}$$

The ∅ is finally measure as:

$$\emptyset = 1 - \frac{\rho_b}{\rho_g}$$

The Boyle's Law assumes ideal gas and isotherm conditions. The manufacturer suggests turning on the machine 15 minutes prior to test, but (even without removing the sample from the sample cell) with relatively short warming times we were finding a negative trend of measured porosities from the first to the last runs of a sample. This shift in porosity though time, was corrected by: (1) keeping the machine on 24/7 so that it is always stable thermally internally and equilibrated to the room temperature, (2) placing the sample in the sample cell for at least 20 minutes prior to start of the test and (3) flushing the sample with helium at a pressure of 2.5 psi (1.5 psi more than suggested by manufacturer) to equilibrate it with the temperature of the gas.

Measurements of porosity and grain density were performed for both the original meteorite samples and the derived cuboids; this allowed us to understand the variability within the

same sample and better evaluate the consistency of our measurements. Based on the size of the sample, we added steel cylinder/cylinders (with no porosity) spacers of known volume (the number varied depending on the size of the cell and the size of the sample) in the measuring cell to reduce the unused working volume; this practice reduced measurement uncertainties. All pycnometer operations are recorded in a dedicated laboratory notebook.

2.4 Leeb Hardness (HLD)

Leeb hardness (HLD) was measured using a portable metal hardness tester (Equotip Piccolo Bambino 2). The Equotip tool response reflects a combination of the samples' elastic properties plus their plasticity. For testing procedure, we followed the manual recommendations as possible; while the tool is held against the surface with 2 fingers, the top button is pressed to release the metal rod inside the instrument which strikes and rebounds from the sample under test. From this procedure we obtain a value known as the HLD that was used to calculate the Coefficient of Restitution (by simply dividing it by 1000). The Coefficient of Restitution is the ratio of the final velocity (after rebound) and the initial velocity (before rebound) of the metal rod. The ratio ranges from 0 to 1, 1 being a perfect elastic collision. In some cases, the HLD was tested along three different orthogonal directions to evaluate possible anisotropies and relations with other properties. A schematic of the instrument is shown in Figure 2.4. As the HLD is partly an elastic property a minimum volume of material is required to avoid boundary effects; ASTM A956M - 17A recommends samples of minimum mass ~2 kg and minimum thickness of 3 mm. The meteorite samples available generally did not meet the mass requirement so meteorite slabs were firmly clamped to larger masses as compensation. Even if it is not

considered a destructive technique, indentation marks were left on sample surfaces after each test.

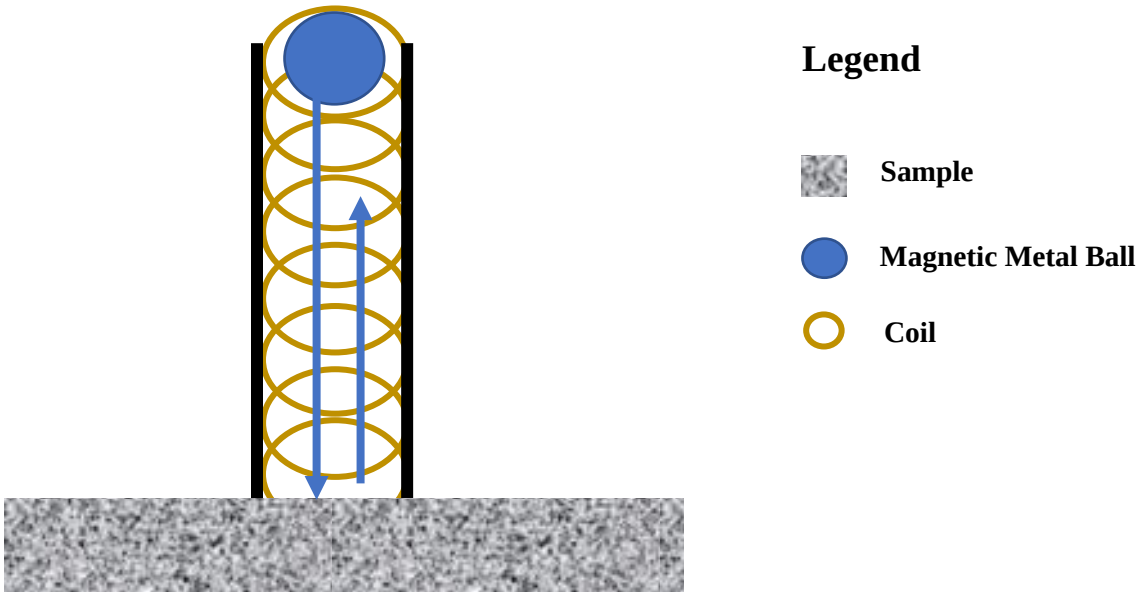

Figure 2.4: After release, the ball hit the surface and rebound. During this process, the ball passes through a coil inducing a voltage. Since the voltage is proportional to the velocity of the ball, the instrument calculates the velocity before and after the impact.

2.5 Seismic Velocities and Dynamic Elastic Moduli

Seismic velocities have been measured using a pulse generator, oscilloscope (Tektronix Model DPO2014) connected to two pairs of compressional and shear wave ultrasonic contact transducers (Olympus V133 and V156, respectively). The transducers, transmitter and receiver, are mount on custom-made wooden or teflon mounts to better control their alignment to the coaxial ideal (Figure 2.5). Although standard practice is to improve coupling between the transducers using a coupling fluid, we wanted to avoid exposing the meteorites to contamination and alteration of their physical properties due to permeating fluid. Adequate wave coupling was achieved by 1) flattening/polishing sample surfaces

and 2) pressing the transducers against the samples with certain force depending upon sample size. To reduce the risk of samples breaking and for better consistency of the measurements, we also measured the stress applied on the sample during the test by using a force transducer (Figure 2.5) placed behind and in line with the holder of one of the contact transducers.

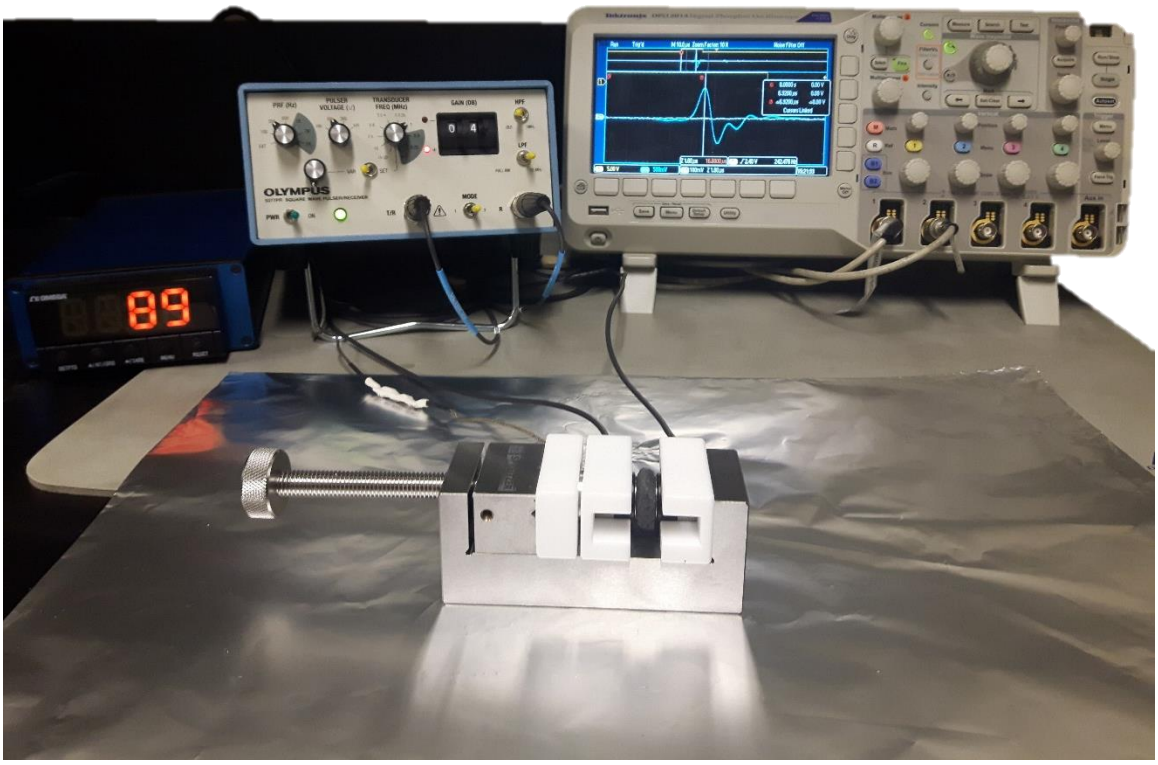

Figure 2.5: The illustration depicts the experimental arrangement employed to measure seismic velocities in this investigation. Positioned to the left is the blue apparatus, a force meter, linked to a force transducer located at the rear of the sample. Adjacent to the force meter is the pulse generator, with the two transducers – transmitter and receiver – connected. Lastly, on the far right, you'll find the oscilloscope. The sample is placed between the two Teflon blocks containing to the two transducers as visible in the center of the image.

We calculate the transducers' internal delay by placing the transducers against each other and reading the time arrival of first break. Before any tests we also performed a calibration

check by measuring the first arrival of a cylinder of PVC of known seismic velocities. The meteorite sample is then compressed between the two contact transducers at different forces depending on sample size and behavior; the transducers are pressed against the sample until no shifting of the wave's first arrival is observed; for extremely weak samples this may not always been achieved due to concern of sample breaking.

The velocities were measured on the cuboid and cube samples along 3 different orthogonal directions (3 measurements for each direction); this allowed us to characterize potential anisotropies in the samples. We considered the P-Wave first arrival as the first break and the S-Wave first arrival as the first peak or trough; we were not able to use the first break as S-Wave first arrival since S waves partially convert to P waves at any impedance boundary (Hons, 2004). The smaller the sample the harder it is to measure S-wave first arrivals because the differences in time arrivals between P-waves and S-waves are minimal in small samples (<5 mm thickness). To better identify the S-waves first arrival (first peak/trough), we first saved the waveform on the oscilloscope (used as comparison for the second step) then, we inverted the orientation of one of the transducers; since the S-waves will invert polarity, but the P-Wave will not (Figure 2.6) this allows unambiguous identification of the S wave arrival.

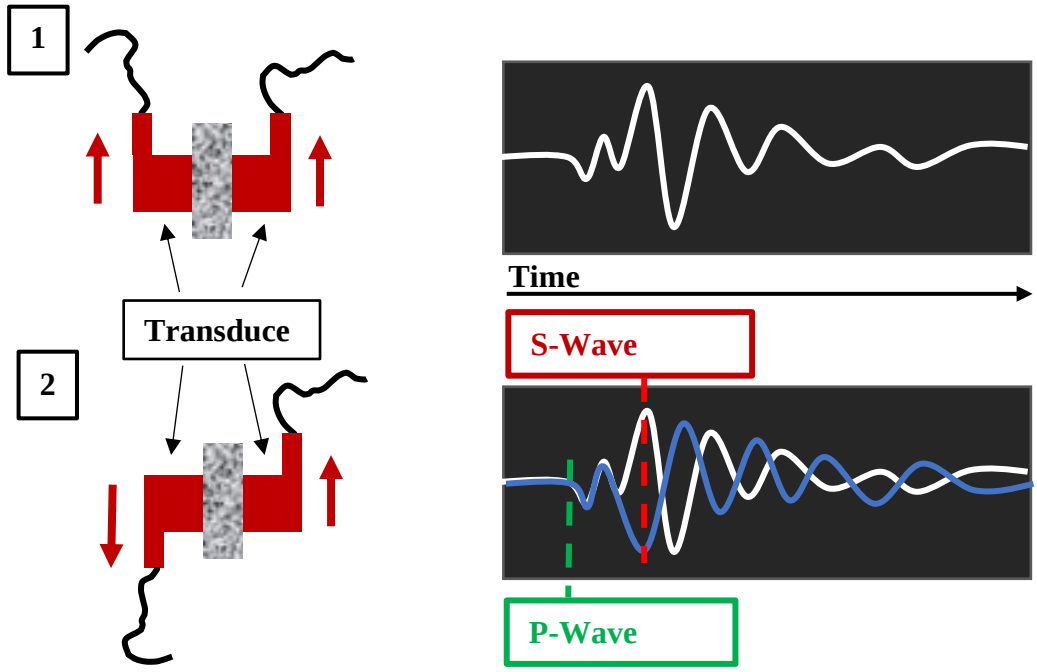

Figure 2.6: The figure shows the procedure we used to measure S-wave first arrivals.

The testing conditions, like gain, pulse voltage and transducer frequencies were recorded in a dedicated laboratory notebook. From the S wave and P wave velocities, we derived the dynamic Young's Modulus, Bulk modulus, Poisson's ratio and Shear modulus along the three different directions. The dynamic elastic moduli can be expressed as function of the P and S wave velocities and the bulk density of the material [e.g., Christaras and Mosse, 1994].

The Dynamic Young's Modulus (E_{dyn}) is also called the dynamic modulus of elasticity and it represent the stiffness of the material. It can be calculated as:

$$E_{dyn} = \rho_b 2V_s^2(1 + \vartheta_{dy})$$

Where ρ_b= bulk density, V_s= S-wave velocity and ϑ_{dy}= dynamic Poisson's ratio.

The Poisson's ratio in general, reflects the material tendency to expand in the 2 directions perpendicular to the direction of compression. In the case of the dynamic one, it effects the propagation and reflection of stress waves and it is calculated as:

$$\vartheta_{dy} = \frac{V_p^2 - 2V_s^2}{2(V_p^2 - V_s^2)}$$

Where V_p = P-wave velocity.

The dynamic Shear modulus (μ_{dy}) described the tendency of a material to shear it can be calculated as:

$$\mu_{dy} = V_s^2 \rho_b$$

The bulk modulus (K_{dy}) reflects the volumetric elasticity so it can be seen as the Young's Modulus in 3 dimensions. The dynamic bulk modulus is calculated as:

$$K_{dy} = \rho_b \left(V_p^2 - \frac{4}{3} V_s^2 \right)$$

The uncertainty for the Vp is ±1.2% and for Vs is ±2.06% (2σ standard deviation). These uncertainties were measured by repeated testing on homogeneous material.

2.6 Ultimate Compressive Strength (σ_u), Static Young's Modulus (E_s) and Proportional Limit (σ_p)

The Ultimate Compressive Strengths were measured with an electromechanical compression test machine (TestResources model 313 Q) using force transducer`s model SM-5000N-294 (TestResources) placed in a partially clean room to minimize contamination of the sample. For the uniaxial compression test, we prepared cuboids with a ≤1:2 width/length ratio to conform with the ASTM International [ASTM D7012-14]

standards. The two transducers were both certified to meet National Institute of Standards and Technology (NIST) standards in early 2023 by Test Resources using procedure based on ASTM E-4. This calibration was part of a recovery operation after the 313Q began producing anomalous extensometer displacement measurements; the fault is believed to have been located to an extensometer data handling issue in the controller during loaded tests. As part assessment validation a half dozen samples were also tested to failure in Professor R. Wong's laboratory in Engineering Faculty facilities at the University of Calgary.

For samples showing seismic wave anisotropies, compressive strengths were measured along 2 different orthogonal directions whenever possible: the 'fastest' and the 'slowest' directions measured for P-wave velocities.

The test involves the sample compressed between 2 platens until failure: the machine measures the load in Newtons (N). To conform with ASTM [ASTM D7012-14] we compressed samples at rates that resulted in failure between 2 – 15 minutes from the start of the test. From the load (F) and area (A) (of the face perpendicular to load axis), we measured the stress (σ) as:

$$\sigma = \frac{F}{A}$$

We report the Ultimate Compressive Strength as the maximum load reached during the test; this differs from the Fracture Point (failure) where usually the stress is less.

Of absolute importance for this test is a good alignment between platens and sample. This was achieved by:

1) Properly aligning the bottom and top platens. This is fundamental so that the sample load axis is parallel to the longest dimension and perfectly perpendicular to the surfaces in contact with the platens: failure to do so, we will result to an “apparent” stress and not a true stress.
2) Having parallel sample surfaces [ASTM D7012-14] in contact with the platens. Please see the section “sample preparation and curation” for details on how parallel surfaces were obtain.
3) Having polished surfaces in contact with the platens to eliminate asperities. Rough surfaces would result in an overestimation of strain for the first part of the test; this is because the load applied on the sample would crush the asperities before being in full contact with the sample.

Please see Figure 2.7 for a schematic of the apparatus.

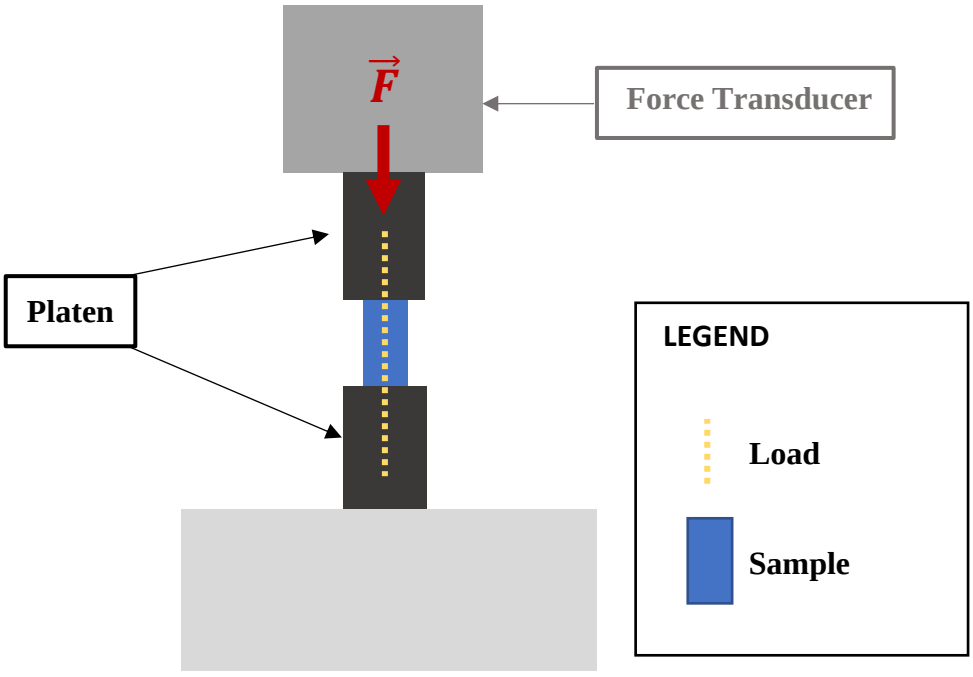

Figure 2.7: Schematic of the press we used to measure strength.

The strain was measured using an extensometer (Epsilon 3542) attached to the platens; this is different from standard measurements on cores where the extensometer is usually directly mounted on the samples (Figure 2.8).

Figure 2.8: The diagram illustrates the extensometer affixed to tabs using knife edges. This configuration enables the precise measurement of strain on very small samples. The depicted sample, an Aluminum alloy positioned between the platens in the image, serves as the designated calibration check standard material.

The extensometer was mounted on tabs attached to the platens with the use of knife edges (to obtain a firm grip with the platens and for better positioning), to adapt the technique to measure very small samples since there is not enough space to mount an extensometer directly on the meteorite samples' surfaces (Figure 2.8).

The strain (ε) is defined as:

$$\varepsilon = \frac{l_1 - l_o}{l_0}$$

where l_0= original sample length, l_1= sample length after strain.

The electromechanical press controller downloads a csv file of time (typical sampling of observables was at a 10 Hertz rate), load, crosshead displacement and extensometer displacement after each test. All testing operations were recorded in a dedicated laboratory notebook and digital data downloads are preserved for each test. Some tests were also recorded by digital camera videos to record failure fracture style and to check measured displacements.

The instrumental setup allowed calculation of the static Young's Modulus as well as the samples' UCS. We used Microsoft Excel to plot the stress vs strain data and to isolate the straight portion of the of the compression curve using method 2 described in ASTM D7012-14.

The straight portion of the stress vs strain curve, represent the proportionality between stress and strain and it is defined by the Hooke's Law:

$$\sigma = E_s \varepsilon$$

Where E_s= Static Young's Modulus.

From Hooke's Law we can then measure the Static Young's Modulus (E_s). The Static Young's modulus represents the stiffness of the material; in general, high E_s means the material will respond more rigidly to stress.

It has been demonstrated that the Static Young's Modulus has a good correlation with the Dynamic Young's Modulus (E_{dyn}); E_s is usually lower than the E_{dyn} [e.g., Ciccotti and Mulagria, 2004].

To better define the deformation response of meteorites to stress, the Proportional Limit (σ_p) was also calculated. The Proportional Limit is defined as the limit of proportionality between the stress and strain (the upper limit of the stress-strain curve where Hooke's Law is valid). The Proportional Limit can be approximated to the elastic limit, that is defined by the Yield Strength; the Yield Strength is much more difficult to identify, and it is usually measured from tensile tests. We show here in Figure 2.9, a schematic on how E_s and the σ_p are calculated.

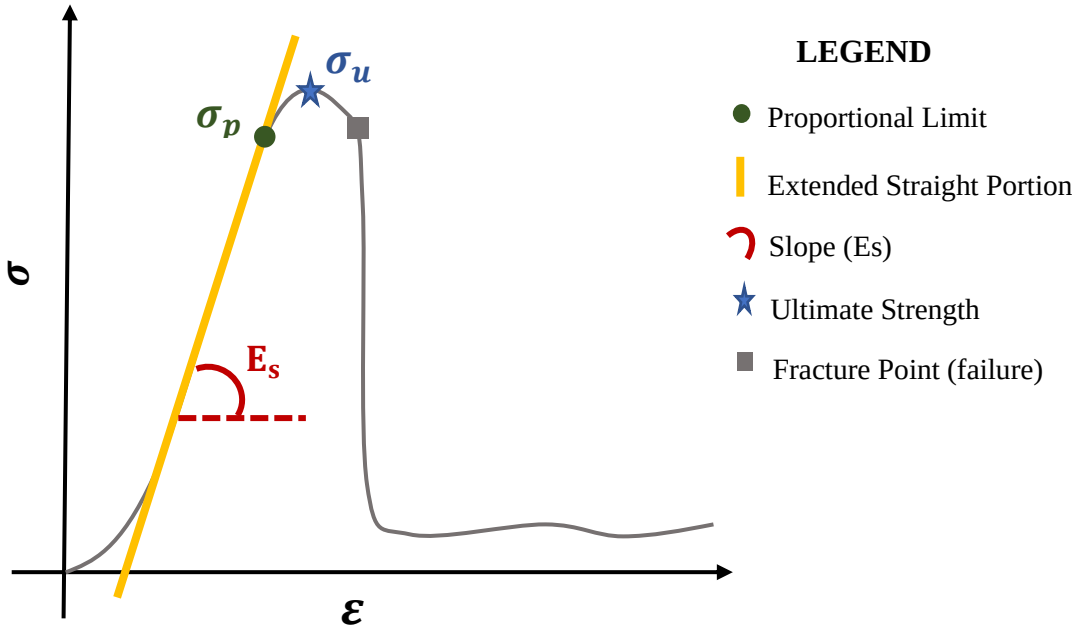

Figure 2.9: Schematic of a stress and strain curved obtained with the 313Q electromechanical press.

2.7 Shear Strength (τ)

The measurements were performed following ASTM procedures [ASTM D5607-08] and the same equipment used for uniaxial compression testing (TestResources model 313 Q and a TestResources force transducer`s model SM-5000N-294). The samples were cut into

regular cubes (2.5x2.5 mm, 5x5 mm and 10x10 mm) for direct shear using guillotine-style stainless steel fixtures also provided by Test Resources.

One side is of the sample is inserted into the first fixture and then we measure the shear test cross-section area using a stainless-steel digital caliper. After measuring the shear test area, the remaining side of the sample is inserted into a second fixture. After positioning the sample and fixtures in the center of the bottom platen the test begins: one fixture is pressed downward (and free to move) and the other is fixed; this creates the shear stress that eventually ruptures the sample (Figure 2.10).

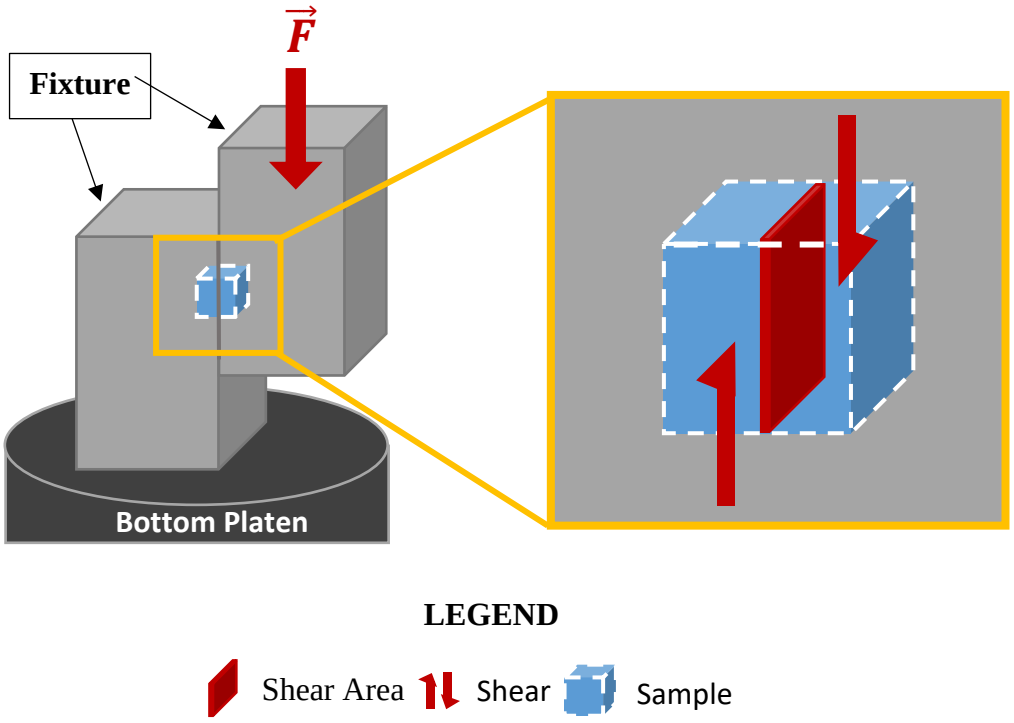

Figure 2.10: Schematic of the set up used for testing shear strength.

As for the compressive test, we select a rate so that the failure happens between 2 – 15 minutes after test start.

We measure the Shear Strength as the maximum load reached during the test. The shear strength (τ) is defined as:

$$\tau = \frac{F}{A}$$

2.8 X-Ray Florescence (XRF) Analysis

We utilized an Olympus® Delta Premium portable ED-XRF analyzer (Figure 2.11) to collect elemental composition data of our cuboids and cubes fragments collected after the shear and compression tests described above. The procedure involved placing the portable device on a holder. The fragments of meteorites are then placed on the analyzer and aligned with the beam using the analyzer's internal camera. A total of 2 to 4 measurements were taken for each sample whenever possible to account for heterogeneities in the sample.

Figure 2.11: The image shows the Olympus® Delta Premium portable ED-XRF analyzer used to measure elemental compositions in this study.

The analysis duration was set at 140 seconds. In this study, the ED-XRF analyzer generated high-energy X-rays (50 kv), enabling the analysis of a wide range of major elements (Mg, Al, Ca, K, Fe, P, S, and Si), including light elements like Mg, as well as trace elements (As, Ba, Cd, Co, Cr, Cs, Cu, Ga, Li, Mn, Mo, Ni, Pb, Rb, Se, Sr, Ti, Tl, U, V, W, and Zn). The instrument's high detection limit allowed for precise analysis down to 0.001%. [Ghanizadeh et al., 2017]

X-ray fluorescence (XRF) works based on the principle of X-ray emission and detection. The sample to be analyzed is bombarded with high-energy X-rays. These X-rays have enough energy to dislodge inner shell electrons from the atoms in the sample. When an inner shell electron is dislodged, an electron from a higher energy shell falls into the vacant inner shell. This transition releases energy in the form of X-rays. The energy of the emitted X-rays is characteristic of the element from which they originate. The emission is then detected using an X-ray detector.

The concentration of each element can be quantified by comparing the emitted fluorescence signals of the sample with those from standard reference materials. More specifically in the ED-XRF or Energy Dispersive X-ray Fluorescence the detector measures the energy of all emitted X-rays simultaneously. The energy spectrum is then analyzed to identify the elements and determine their concentrations. ED-XRF systems alo provide portability, allowing for on-site collection of elemental composition data [eg. Ghanizadeh et al, 2017] facilitating non-destructive analysis of elemental compositions in meteorites.

However, it is important to consider the limitations associated with handheld XRF measurements in dense rocks. Firstly, the collected data predominantly reflect the surface

elemental composition and may not accurately represent the composition of the entire rock, as X-rays only penetrate the rock surface to a depth of less than 5 µm. Secondly, discrepancies can arise when comparing datasets obtained using different handheld devices due to variations in factory settings and calibration, even among devices of the same model from the same vendor. [Ghanizadeh et al., 2017]

2.9 Regression analysis and statistics

Data analyses, including regression analysis and the coefficient of determination (R^2), were conducted using Prism 9 (GraphPad). For each graph, three distinct forms of regression curves: exponential, second-order polynomial, and linear, were considered.

The second order polynomial has a general equation of:

$$Y = B0 + B1 * X + B2 * X^2$$

Where B0, B1 and B2 are constants.

The exponential curve has a general equation of:

$$Y = Y0 * e^{(k*X)}$$

Where Y0 is the intercept, k is the rate constant.

The linear regression has a general equation of:

$$Y = Y_0 + mX$$

Where Y_0 is the intercept and m the slope.

However, only the form that yielded the highest R^2 value has been presented in this thesis.

3: RESULTS

This chapter represents all the results obtained in this study. To ensure clarity and coherence, this chapter is structured into distinct sections, each devoted to the examination of specific properties. This approach facilitates a systematic presentation of the results.

In the table presented in this chapter the first 3/4 letters of the ID indicate the meteorite name: MUR = Murchison, BUZ = Buzzard Coulee, GOLD = Golden, ABE = Abee, TAG = Tagish Lake and MOSS.

The contextualization and interpretation of the results will be critically evaluated in the chapter “discussion".

3.1 Bulk Density (ρ_b), Grain Density (ρ_g) and Porosity ($\emptyset$)

Understanding the fundamental properties of matter, such as density and porosity is crucial for comprehending the composition and structure of meteorites and their parent asteroids. The density of a rock is largely determined by the atomic masses of its constituent elements and their arrangement in crystalline structures. However, void spaces can occur, and these collectively known as porosity, can lower the density of a rock.

In general, the grain density (ρ_g) will closely reflect the densities of the minerals that compose the meteorite, while the bulk density (ρ_b) will reflect the mineralogy and all the pores in the rock.

The density of meteorites can be significantly influenced by various factors, including weathering processes, thermal effects, and impact shock. Among these factors, weathering plays a significant role, particularly through the process of oxidation. The oxidation of meteoritic metals leads to a substantial increase in volume, resulting in notable changes in

density. Furthermore, weathering processes often lead to the formation less dense minerals contributing to a decrease in the overall bulk density of the meteorite. However, it is important to note that the expanding volume resulting from oxidation fills the pore space, leading to a decrease in grain density and porosity. [Ostrowski and Bryson, 2019]

Porosity and density measurements provide valuable insights into the lithification processes and the formation of asteroids [e.g., Ota et al., 2023]. Understanding porosity is also particularly crucial for modeling hydration processes on parent asteroids since porosity is usually related to permeability [e.g., Bland et al., 2009].

To ensure the reliability and validity of our data and study, we focus exclusively on fresh meteorite falls, as discussed in the introduction chapter. This approach is essential for investigating and analyzing properties that are representative of asteroids on a larger scale. The data densities and porosity data from this study are summarized int Table 1.

Table 1: the provided table reports data on mass, dimensions, bulk and grain density, as well as porosity, for all meteorites investigated within the scope of this project.

ID	Mass [g]	Length [mm]	Width [mm]	Thickness [mm]	ρ_b [g/cm^3]	ρ_g [g/cm3]	Porosity [%]
ME 2640 A (small)	1.4647	2.5			2.3977	2.9355	18.3
Murchison ME 2640 A.1	4.2393	9.08			2.398		18.0
Murchison ME 2640 A.2	9.2425	9.1			2.408		18.0
Murchison ME 2640 A.3	9.5176	9.43			2.419		18.0
MUR.2021.001.01	0.0351	2.54	2.47	2.41	2.3215	2.9453	19.3
MUR.2021.001.02	0.0362	2.53	2.49	2.46	2.3359	2.9453	19.3
MUR.2021.001.03	0.0340	2.49	2.41	2.37	2.3906	2.9453	19.3

MUR.2021.001.04	0.0364	2.51	2.50	2.41	2.4070	2.9453	19.3
MUR.2021.001.05	0.2864	4.96	4.87	4.87	2.4346	2.8881	15.7
MUR.2021.001.06	0.2693	4.91	4.91	4.86	2.3524	2.8680	18.0
MUR.2021.001.07	0.2107	7.18	3.53	3.50	2.3607	2.8990	18.6
MUR.2021.001.08	0.8241	4.98	4.90	4.84	2.4055	2.8985	17.0
MUR.2021.001.09	0.2824	4.96	4.87	4.84	2.4155	2.8703	15.8
MUR.2021.001.10	0.2432	7.45	3.70	3.69	2.4009	2.8287	15.1
MUR.2021.001.11	3.6486	18.09	9.14	9.13	2.4250	2.9070	16.6
MUR.2021.001.12	0.8253	11.23	5.56	5.46	2.4408	2.9483	17.2
MUR.2021.001.13	1.7051	14.12	7.10	7.02	2.4268	2.9130	16.7
MUR.2021.001.14	1.0790	12.22	6.16	6.01	2.3978	2.8741	16.6
BUZ.001.01.2022	3.3449	10.05	9.89	9.88	3.4139	3.7221	8.3
BUZ.001.02.2022	4.2902	17.09	8.55	8.54	3.4371	3.6842	6.7
BUZ.001.03.2022	3.4166	10.01	9.91	9.83	3.5037	3.7249	5.9
BUZ.001.04.2022	6.9950	20.14	10.20	9.80	3.4574	3.7227	7.1
GOLD.001.01.2022	3.0381	9.95	9.93	9.84	3.1315	3.6069	13.2
GOLD.001.02.2022	2.9455	9.93	9.86	9.86	3.0591	3.5493	13.8
GOLD.001.03.2022	2.0224	13.91	6.86	6.80	3.1143	3.5336	11.9
GOLD.001.04.2022	0.3528	4.98	4.87	4.83	3.0485	3.5624	14.4
GOLD.001.05-1.2022	7.8878	21.90	10.78	10.76	3.1051	3.5689	13.0
GOLD.001.05-2.2022	8.2320	22.40	10.90	10.80	3.1234	3.5419	11.8
GOLD.001.05-3.2022	2.9212	9.86	9.84	9.70	3.1184	3.5700	12.7
GOLD.001.05-4.2022	2.9952	9.99	9.86	9.85	3.0902	3.5612	13.2

ABE.001.01	0.3836	5.08	4.95	4.52	3.3816	3.5405	4.5
ABE.001.02	0.4125	5.07	4.92	4.82	3.4309	3.5155	2.4
ABE.001.03	1.5263	11.84	6.04	5.95	3.5870	3.6241	1.0
ABE.001.04	1.3493	10.40	6.16	5.91	3.5637	3.6612	2.7
ABE.001.05	1.8890	12.70	6.51	6.47	3.5314	3.6378	2.9
ABE.001.06	1.8877	12.69	6.57	6.37	3.5544	3.6547	2.7
ABE.001.07	0.4080	4.97	4.92	4.56	3.6734	3.7785	2.8
TAG.001.01.2022	0.023	2.59	2.46	2.43	1.5101	2.8129	46.1
TAG.001.02.2022	0.2753	7.64	3.89	3.87	1.5983	2.8861	44.6
TAG.001.03.2023	0.4338	10.32	5.25	5.14	1.5614	2.8921	46.0
TAG.001.04.2023	0.1824	5.02	4.90	4.81	1.5474	2.8528	45.8
TAG.001.05.2023	0.1742	5.04	4.87	4.78	1.5010	2.8844	48.0
MM-01 26d	4.8930				1.5400	2.8100	46.2
PM-09	21.5410				1.5400	2.8200	45.7
PM-09 d	21.5410				1.5400	2.8200	45.7
MOSS	5.8150	16.7	0.98	11.00	2.9372	3.7172	21.0
MOSS C1		8.81	5.77	4.88	2.9372	3.7172	21.0
MOSS C2		9.07	5.02	4.82	2.9372	3.7172	21.0
MOSS C3		7.26	5.02	4.72	2.9372	3.7172	21.0
MOSS S1	5.8180	4.95	4.94	4.93	2.9090	3.7377	22.2
MOSS S2					2.9090	3.7377	22.2
MOSS S3		4.99	4.98	4.87	2.9090	3.7377	22.2

3.2 Seismic Velocities (Vp, Vs) and Dynamic Elastic Moduli

Elastic constants play a crucial role in analyzing stresses and strains within materials. Two primary methods are employed to measure these constants: the static method and the dynamic method. The static method involves measuring the deformation caused by a known force applied to a material. By quantifying the resulting deformation, the elastic constants can be determined. On the other hand, the dynamic method utilizes the measurement of ultrasonic body wave velocities. By analyzing the speed of these waves propagating through a material, the elastic constants can be derived. In this section, we present the dynamic elastic moduli data for the meteorites of this study.

Empirical relations suggest that static moduli values tend to be lower than dynamic moduli values. However, there is a significant scatter in the data, and in certain cases, the static measurements yield values that can be an order of magnitude smaller than the corresponding dynamic estimates [Ciccotti e Mulargia, 2004]. Moreover, numerous empirical relationships have been suggested to establish a connection between the dynamic and static moduli of terrestrial rocks. These relationships vary in nature, encompassing both linear and power-law forms. Most of the literature agree that these relations are different based on the type of rock [e.g., Bronson et al., 2016; Davarpanah et al., 2020] emphasizing the necessity for improved comprehension and characterization of extraterrestrial materials, given their evident structural and compositional dissimilarity from most terrestrial rocks.

It has been suggested that the disparity observed between seismic measurements and quasi-static laboratory measurements of elastic properties, can serve as an indicator for estimating

the extent of damage in a rock [Ciccotti e Mulargia, 2004]. The more damage the bigger the difference.

The elastic constants and the speed of elastic waves are strongly impacted by the volume, shape, and distribution of pore spaces [e.g., Yu et al., 2016]. This leads to distinct differences in these properties between porous meteorites providing valuable insights into the unique characteristics of meteorites and their parent bodies. [Ostrowski and Bryson, 2019]

Seismic waves passing through materials exert stress, which represents the internal resistance of an object to external forces. As these waves propagate, they transfer energy to the material, leading to strain, which describes the relative change in shape or dimensions induced by the applied stress. Materials that can readily recover their original shape or size after deformation are classified as elastic. By understanding how materials respond to stress and strain, we gain valuable insights into their elasticity and the role it plays in natural event where stresses are applied at a fast rate (e.g., impact cratering).

Measuring seismic velocities also serves as a valuable method for assessing anisotropy in rocks, as the velocity is influenced by the material composition and internal structure (such as porosity and pore shape). Consequently, we conducted measurements on all our samples along three distinct orthogonal directions (Tables 2, 3 and 4).

Table 2: This table presents the values of Vp and Vs measured along three different orthogonal directions.

ID	Vp (Length) [m/s]	Vp (Width) [m/s]	Vp (Thickness) [m/s]	Vs (Length) [m/s]	Vs (Width) [m/s]	Vs (Thickness) [m/s]
MUR.2021.001.05	3281.3	3397.0	3345.7	1767.4	1770.7	1807.5
MUR.2021.001.06	3372.3	3317.6	3337.9	1753.6	1753.6	1800.0
MUR.2021.001.07	3096.2	3223.7	3292.6	1705.5	1735.5	1798.6
MUR.2021.001.08	3184.2	3190.1	3104.7	1716.3	1737.6	1682.4
MUR.2021.001.09	3107.8	3212.4	3315.1	1641.3	1848.9	1723.2
MUR.2021.001.10	3163.5	3203.5	3309.4	1748.0	1905.3	1810.6
MUR.2021.001.12	3065.8	3234.4	3275.3	1853.7	1887.3	1833.4
MUR.2021.001.13	3215.7	3276.4	3350.8	1848.7	2048.5	2165.3
MUR.2021.001.14	3111.8	3131.7	3318.6	1800.8	1985.8	2054.0
BUZ.001.01.2022	3068.5	3200.9	3296.7	1799.9	1899.2	1880.9
BUZ.001.02.2022	3850.3	3509.9	3706.6	2263.8	2317.8	2256.4
BUZ.001.03.2022	3850.0	3887.6	4123.3	1940.7	2298.9	2255.6
BUZ.001.04.2022	3484.8	3258.8	3264.5	2396.7	2029.9	1981.9
GOLD.001.01.2022	2203.0	2065.3	2036.4	1325.7	1276.7	937.0
GOLD.001.02.2022	2100.3	1975.2	2246.8	1081.9	1188.2	896.9
GOLD.001.03.2022	2295.4	2053.9	1907.3	1022.6	1014.8	1028.8
GOLD.001.04.2022	1960.6	2430.1	2107.3	1046.2	1415.7	1083.0
GOLD.001.05-1.2022	1645.4	1638.3	1870.0	1199.7	978.8	987.7
GOLD.001.05-2.2022	1837.6	1819.7	1884.8	1371.4	1148.1	998.7

GOLD.001.05-3.2022	2331.0	2221.2	2687.0	1389.9	1240.2	1120.9
GOLD.001.05-4.2022	1978.2	1892.5	2091.3	1105.8	920.3	1044.1
ABE.001.01	6742.0	6540.7	6725.5	3039.6	2907.0	3040.5
ABE.001.02	6814.5	6671.2	6783.7	2934.0	2874.7	3120.2
ABE.001.03	6330.5	6445.7	6670.4	3098.7	2309.2	3003.0
ABE.001.04	6238.0	6406.3	6504.4	3063.8	3032.5	2957.7
ABE.001.05	6220.6	6704.5	6718.8	3166.2	3138.3	3119.0
ABE.001.06	6284.7	6582.7	6526.6	3099.3	2904.8	2965.5
ABE.001.07	6730.8	6813.2	6263.7	2902.8	2938.4	2733.8
TAG.001.01.2022		1497.6	1429.6		773.1	775.3
TAG.001.02.2022	1478.4	1604.3	1643.5	791.9	994.2	936.7
PM-09	1258.6	1255.0		805.1	790.1	
PM-09 d	1277.2	1220.6		758.3	744.9	
MOSS	1914.9	2087.6	2366.2	1215.4	1286.1	1368.9
MOSS C1	1914.9	2087.6	2366.2	1215.4	1286.1	1368.9
MOSS C2	1914.9	2087.6	2366.2	1215.4	1286.1	1368.9
MOSS C3	1914.9	2087.6	2366.2	1215.4	1286.1	1368.9
MOSS S1	1914.9	2087.6	2366.2	1215.4	1286.1	1368.9
MOSS S2	1914.9	2087.6	2366.2	1215.4	1286.1	1368.9
MOSS S3	1914.9	2087.6	2366.2	1215.4	1286.1	1368.9

Table 3: this table presents the value of average Vp, Vs and the dynamic elastic moduli calculated from the average Vp and Vs. vd = dynamic Poisson's ratio; μd = dynamic shear modulus; Kd = dynamic bulk modulus and Ed = dynamic Young's Modulus.

ID	Avg Vp [m/s]	Avg Vs [m/s]	Avg vd	Avg μd [Gpa]	Avg Kd [Gpa]	Avg Ed [Gpa]
Murchison ME 2640 A.1	3180.2	1755.6	0.28	7.4	14.4	18.9
Murchison ME 2640 A.2	3278.1	1828.8	0.27	8.1	15.1	20.5
Murchison ME 2640 A.3	3264.8	1884.9	0.25	8.6	14.3	21.5
MUR.2021.001.05	3341.3	1781.9	0.30	7.7	16.9	20.1
MUR.2021.001.06	3342.6	1769.1	0.31	7.4	16.5	19.2
MUR.2021.001.07	3204.2	1746.5	0.29	7.2	14.6	18.6
MUR.2021.001.08	3159.7	1712.1	0.29	7.1	14.6	18.2
MUR.2021.001.09	3211.8	1737.8	0.29	7.3	15.2	18.9
MUR.2021.001.10	3225.5	1821.3	0.27	8.0	14.4	20.2
MUR.2021.001.11	3037.8	1703.1	0.27	7.0	13.0	17.9
MUR.2021.001.12	3191.8	1858.1	0.24	8.4	13.6	21.0
MUR.2021.001.13	3281.0	2020.8	0.19	9.9	12.9	23.7
MUR.2021.001.14	3187.4	1946.9	0.20	9.1	12.2	21.9
BUZ.001.01.2022	3188.7	1860.0	0.24	11.8	19.0	29.3
BUZ.001.02.2022	3688.9	2279.3	0.19	17.9	23.0	42.5
BUZ.001.03.2022	3953.6	2165.1	0.29	16.4	32.9	42.2
BUZ.001.04.2022	3336.0	1981.9	0.23	13.6	20.4	33.3
GOLD.001.01.2022	2101.6	1179.8	0.27	4.4	8.0	11.1

GOLD.001.02.2022	2107.4	1055.7	0.33	3.4	9.0	9.1
GOLD.001.03.2022	2085.5	1022.1	0.34	3.3	9.2	8.7
GOLD.001.04.2022	2166.0	1181.6	0.29	4.3	8.6	11.0
GOLD.001.05-1.2022	1717.9	1055.4	0.20	3.5	4.6	8.3
GOLD.001.05-2.2022	1847.4	1172.7	0.16	4.3	4.9	10.0
GOLD.001.05-3.2022	2413.1	1250.3	0.32	4.9	11.7	12.8
GOLD.001.05-4.2022	1987.3	1023.4	0.32	3.2	7.9	8.5
ABE.001.01	6669.4	2995.7	0.37	30.3	110.0	83.4
ABE.001.02	6756.5	2976.3	0.38	30.4	116.1	83.9
ABE.001.03	6482.2	2803.6	0.38	28.2	113.1	78.1
ABE.001.04	6382.9	3018.0	0.36	32.5	101.9	88.0
ABE.001.05	6548.0	3141.1	0.35	34.8	105.0	94.1
ABE.001.06	6464.7	2989.9	0.36	31.8	106.2	86.7
ABE.001.07	6464.7	2858.3	0.38	30.0	113.5	82.7
TAG.001.01.2022	1463.6	774.2	0.31	0.9	2.0	2.4
TAG.001.02.2022	1575.4	907.6	0.25	1.3	2.2	3.3
PM-09	1256.8	797.6	0.16	1.0	1.1	2.3
PM-09 d	1248.9	751.6	0.22	0.9	1.2	2.1
MOSS	2122.9	1290.1	0.21	4.9	6.7	11.8
MOSS C1	2122.9	1290.1	0.21	4.9	6.7	11.8
MOSS C2	2122.9	1290.1	0.21	4.9	6.7	11.8
MOSS C3	2122.9	1290.1	0.21	4.9	6.7	11.8

MOSS S1	2122.9	1290.1	0.21	4.8	6.7	11.7
MOSS S2	2122.9	1290.1	0.21	4.8	6.7	11.7
MOSS S3	2122.9	1290.1	0.21	0.0	0.0	0.0

Table 4: this table presents the values of νd, Ed, μd and Kd measured for each of the 3 orthogonal directions.

ID	vd (Length)	vd (Width)	vd (Thickness)	Ed (Length) [Gpa]	Ed (Width) [Gpa]	Ed (Thickness) [Gpa]
MUR.2021.001.05	0.30	0.31	0.29	19.7	20.1	20.6
MUR.2021.001.06	0.31	0.31	0.29	19.0	18.9	19.7
MUR.2021.001.07	0.28	0.30	0.29	17.6	18.4	19.7
MUR.2021.001.08	0.30	0.29	0.29	18.4	18.7	17.6
MUR.2021.001.09	0.31	0.25	0.31	17.0	20.7	18.9
MUR.2021.001.10	0.28	0.23	0.29	18.8	21.4	20.3
MUR.2021.001.12	0.21	0.24	0.27	20.3	21.6	20.9
MUR.2021.001.13	0.25	0.18	0.14	20.8	24.0	26.0
MUR.2021.001.14	0.25	0.16	0.19	19.4	22.0	24.1
BUZ.001.01.2022	0.24	0.23	0.26	27.4	30.3	30.4
BUZ.001.02.2022	0.24	0.11	0.21	43.5	41.1	42.2
BUZ.001.03.2022	0.33	0.23	0.29	35.1	45.6	45.9
BUZ.001.04.2022	0.05	0.18	0.21	41.8	33.7	32.8
GOLD.001.01.2022	0.22	0.19	0.37	13.4	12.2	7.5

GOLD.001.02.2022	0.32	0.22	0.41	9.4	10.5	6.9
GOLD.001.03.2022	0.38	0.34	0.29	9.0	8.6	8.5
GOLD.001.04.2022	0.30	0.24	0.32	8.7	15.2	9.4
GOLD.001.05-1.2022	-0.07	0.22	0.31	8.3	7.3	7.9
GOLD.001.05-2.2022	-0.13	0.17	0.30	10.2	9.6	8.1
GOLD.001.05-3.2022	0.22	0.27	0.39	14.7	12.2	10.9
GOLD.001.05-4.2022	0.27	0.35	0.33	9.6	7.0	9.0
ABE.001.01	0.37	0.38	0.37	85.8	78.7	85.8
ABE.001.02	0.39	0.39	0.37	81.9	78.6	91.2
ABE.001.03	0.34	0.43	0.37	92.5	54.6	88.8
ABE.001.04	0.34	0.36	0.37	89.7	88.9	85.4
ABE.001.05	0.33	0.36	0.36	93.8	94.6	93.6
ABE.001.06	0.34	0.38	0.37	91.5	82.7	85.6
ABE.001.07	0.39	0.39	0.38	85.8	87.9	75.9
TAG.001.01.2022		0.32	0.29		2.4	2.3
TAG.001.02.2022	0.30	0.19	0.26	2.6	3.8	3.5
PM-09	0.15	0.17		2.3	2.3	
PM-09 d	0.23	0.20		2.2	2.1	
MOSS	0.16	0.19	0.25	10.1	11.6	13.7
MOSS C1	0.16	0.19	0.25	10.1	11.6	13.7
MOSS C2	0.16	0.19	0.25	10.1	11.6	13.7
MOSS C3	0.16	0.19	0.25	10.1	11.6	13.7

MOSS S1	0.16	0.19	0.25	10.0	11.5	13.6
MOSS S2	0.16	0.19	0.25	10.0	11.5	13.6
MOSS S3	0.16	0.32	0.29	0.0	2.4	2.3

ID	μd (Length) [Gpa]	μd (Width) [Gpa]	μd (Thickness) [Gpa]	Kdy (Length) [Gpa]	Kdy (Width) [Gpa]	Kdy (Thickness) [Gpa]
MUR.2021.001.05	7.6	7.6	8.0	16.1	17.9	16.6
MUR.2021.001.06	7.2	7.2	7.6	17.1	16.2	16.0
MUR.2021.001.07	6.9	7.1	7.6	13.5	15.1	15.4
MUR.2021.001.08	7.1	7.3	6.8	14.9	14.8	14.1
MUR.2021.001.09	6.5	8.3	7.2	14.7	13.9	17.0
MUR.2021.001.10	7.3	8.7	7.9	14.2	13.0	15.8
MUR.2021.001.12	8.4	8.7	8.2	11.8	13.9	15.2
MUR.2021.001.13	8.3	10.2	11.4	14.0	12.5	12.1
MUR.2021.001.14	7.8	9.5	10.1	12.9	10.9	12.9
BUZ.001.01.2022	11.1	12.3	12.1	17.4	18.6	21.0
BUZ.001.02.2022	17.6	18.5	17.5	27.5	17.7	23.9
BUZ.001.03.2022	13.2	18.5	17.8	34.3	28.3	35.8
BUZ.001.04.2022	19.9	14.2	13.6	15.5	17.7	18.7
GOLD.001.01.2022	5.5	5.1	2.7	7.9	6.6	9.3
GOLD.001.02.2022	3.6	4.3	2.5	8.7	6.2	12.2
GOLD.001.03.2022	3.26	3.2	3.3	12.1	8.9	6.9
GOLD.001.04.2022	3.34	6.1	3.6	7.3	9.9	8.8
GOLD.001.05-1.2022	4.47	3.0	3.0	2.4	4.4	6.8

GOLD.001.05-2.2022	5.9	4.1	3.1	2.7	4.9	6.9
GOLD.001.05-3.2022	6.0	4.8	3.9	8.9	9.0	17.3
GOLD.001.05-4.2022	3.8	2.6	3.4	7.1	7.6	9.0
ABE.001.01	31.2	28.6	31.3	112.1	106.6	111.3
ABE.001.02	29.5	28.4	33.4	119.9	114.9	113.4
ABE.001.03	34.4	19.1	32.3	97.8	123.5	116.5
ABE.001.04	33.5	32.8	31.2	94.1	102.6	109.2
ABE.001.05	35.4	34.8	34.4	89.4	112.4	113.6
ABE.001.06	34.1	30.0	31.3	94.9	114.0	109.7
ABE.001.07	31.0	31.7	27.5	125.1	128.2	107.5
TAG.001.01.2022		0.9	0.9		2.2	1.9
TAG.001.02.2022	1.0	1.6	1.4	2.2	2.0	2.4
PM-09	1.0	1.0		1.1	1.1	
PM-09 d	0.9	0.9		1.3	1.2	
MOSS	4.3	4.9	5.5	5.0	6.3	9.1
MOSS C1	4.3	4.9	5.5	5.0	6.3	9.1
MOSS C2	4.3	4.9	5.5	5.0	6.3	9.1
MOSS C3	4.3	4.9	5.5	5.0	6.3	9.1
MOSS S1	4.3	4.8	5.5	4.9	6.3	9.0
MOSS S2	4.3	4.8	5.5	4.9	6.3	9.0
MOSS S3	4.3	4.8	5.5	4.9	6.3	9.0

3.3 Hardness (HLD) and Coefficient of Restitution (e)

The Leeb hardness test measures the rebound hardness of materials and was initially designed for metals. However, various studies have established correlations between the Leeb hardness (HLD), the Unconfined Compressive Strength, and the elastic properties of rocks [e.g., Corkum et al., 2017; Ghorbani et al., 2022]. Some of the advantages of this test is that it can be conducted quickly, conveniently, and causing minor damage (a small indentation mark is left on the surface) to rock samples.

The Leeb Hardness is considered one of the rebound-based hardness tests, characterized by their dynamic nature, having broad applicability in estimating the elastic and plastic characteristics of rocks.

Karaman and Kesimal, 2015 found a strong correlation between the hardness (Schmidt Rebound Hardness, very similar to the HLD), UCS, P-wave velocities, and the P-wave/UCS ratio for different terrestrial rock types. Furthermore, the study revealed that the P-wave/UCS ratios decrease exponentially as the hardness values increase. This indicates that the P-wave/UCS ratio is dependent on the value of hardness for rocks.

Ghorbani et al., 2022 indicated a significant correlation between the dynamic Young's Modulus and the Leeb hardness in both igneous and sedimentary rocks. The same study also revealed that the presence of porosity in sedimentary rocks and intracrystalline fissures in igneous rocks considerably reduces the Leeb hardness. Consequently, these structural characteristics cause notable alterations in the propagation of longitudinal waves.

Ghanizadeh et al., 2017 observed notable correlations between elemental composition, mechanical hardness, and the Unconfined Compressive Strength (UCS) for sedimentary rocks core samples. Intervals exhibiting higher mechanical hardness tend to have higher

silicon content. In a general sense, the UCS values demonstrate two trends: 1) a decrease with increasing magnesium and calcium contents, and 2) an increase with increasing aluminum and silicon contents.

The HLD is also a valuable tool to characterize heterogeneities in rocks.

While the Leeb hardness test (HLD) has been extensively employed in traditional geology, and geotechnical engineering, it has not yet been utilized for meteorites. Considering the destructive nature of some strength measurements like the Unconfined Compressive Strength, the non-destructive nature of the Leeb hardness test makes it a potentially viable method for predicting the strength and elastic properties of meteorites. Nevertheless, the successful implementation of this approach (considering the differences in correlation among different type of terrestrial rocks) would require the establishment of a dataset specific to meteorites. Such a dataset would facilitate the correlation between HLD values, the elastic, and the strength characteristics of meteorites.

By dividing the HLD by 1000 (see methods for more details) we obtained the Coefficient of Restitution. The coefficient of restitution (COR) is a value that represents the elasticity or "bounciness" of a collision between two objects. It is a dimensionless quantity, typically denoted by the symbol "e." The coefficient of restitution is defined as the ratio of the relative velocity of separation to the relative velocity of approach between two objects after a collision. The relative velocity of approach refers to the speed at which the objects are moving towards each other just before the collision, while the relative velocity of separation is the speed at which they move away from each other after the collision.

The coefficient of restitution can range between 0 and 1, representing different types of collision; 1) 0 indicates a perfectly inelastic collision where the objects stick together after

the collision, losing all their initial kinetic energy, 2) 1 represents a perfectly elastic collision where there is no loss of kinetic energy and 3) between 0 and 1 indicate partially elastic collisions, where some kinetic energy is lost but not all.

The Coefficient of Restitution is an important parameter to study asteroid evolution [e.g., Brisset et al., 2018; Gao et al., 2022] and more practically, it has been used as a key input for analysis for lander MASCOT that bounced on the surface of asteroid Ryugu in 2018 [e.g., Biele et al., 2017]. However, studies on the Coefficient of Restitution of meteorites have never been published to date.

Here in Table 5 are presented the results for the HLD and coefficient of restitution.

Table 5: The table displays the measured data for HLD and Coefficient of Restitution (e) across all meteorites examined within this study.

Meteorite	Group	HLD	e
Abee	EH4	714	0.71
"	"	704	0.70
"	"	695	0.70
Bruderheim	L6	710	0.71
Buzzard Coulee	H4	628	0.63
Cape York	IIIAB	408	0.41
Golden	L\LL5	625	0.63
"	"	628	0.63
Millarville	IVA	403	0.40
Murchison	CM2	562	0.56

"	"	567	0.57
"	"	520	0.52
Xiquipilco	Iron	380	0.38
"	"	388	0.39
"	"	395	0.40

3.4 Ultimate Compressive Strength (UCS), Static Young's Modulus (E_s) and Proportional Limit (σ_p)

In this section we present the results for the Ultimate Compressive Strength, Static Young's Modulus and Proportional Limit for the meteorite samples measured in this study (Table 6).

Strength refers to the capacity of a rock to endure external forces without fracturing. Specifically, compressive strength denotes a rock's ability to resist loads. Various methods exist to assess compressive strength, with laboratory measurements being the most common approach. By employing theoretical models of atmospheric entry, scientists have also tried to quantify the strength of meteoroids. [e.g., Borovička et al., 2020]

Gaining a comprehensive understanding of various techniques and their implications is crucial. In the context of this study, the measured compressive strength specifically pertains to the Uniaxial Compressive Strength (UCS). The term "uniaxial" signifies that the force is exerted solely in one direction, while the other direction experiences only the atmospheric pressure present in the laboratory setting.

In traditional geology, another common measurement for compressive strength is the Triaxial Compressive Strength. This involves applying a specified confining pressure,

which enables the replication of stress axes observed in various geological settings and depths. As the confining pressure increases, it simulates different conditions found at varying depths.

This study solely focuses on the Uniaxial Compressive Strength (UCS). Undifferentiated asteroids, being relatively small objects, do not experience significant confining pressures even at maximum depths. Therefore, the UCS serves as an appropriate representation for studying any natural phenomena occurring on asteroids that involve stress (e.g., impact cratering, asteroid disruption, boulder fracturing processes, regolith formation mechanisms). The UCS also represents the strength during atmospheric entry.

This study presents the strengths (both shear and compressive) as ultimate strengths. The ultimate strength refers to the maximum stress attained on the sample, distinguishing it from the fracture point, which indicates the failure of the rock that often happens at slightly lower stresses.

In this study we also measured the Static Young's modulus, also known as the modulus of elasticity, that is a material property that describes its stiffness or resistance to deformation when subjected to an applied force.

Mathematically, Young's modulus (E) is defined as the ratio of stress (σ) to strain (ε) in a linear elastic material. The modulus indicates how much a material will deform under stress. A higher Young's modulus signifies a stiffer material that requires a larger stress to produce a given amount of strain, while a lower modulus suggests a more flexible material that deforms more easily under stress.

The Young's modulus is applicable only within the elastic deformation range of a material describe by the Hooke's Law. Once a material reaches its elastic limit, it may exhibit plastic deformation or permanent deformation.

When determining material properties, dynamic methods, which measure Young's modulus through seismic velocities, generally result in a higher value compared to static methods. This disparity can be attributed to various factors, including differences in strain rates caused by acoustic waves compared to static loading, material heterogeneity, anisotropy effects, and the varying magnitudes of induced strain. Among these factors, the primary contributing factor is the varying magnitudes of induced strain. This is because structural features such as cracks and pores may undergo significant deformations during a static experiment but remain relatively unaffected by the propagation of acoustic waves. [e.g., Kotsanis et al., 2021]

One other parameter that we present here but that may never have been previously measured for meteorites, is the Proportional Limit. The proportional limit, also known as the elastic limit, is the point at which a material transitions from being elastically deformed (able to return to its original shape upon the removal of stress) to plastically deformed (exhibiting permanent deformation even after the stress is removed). It is calculated as stress. While it is similar in concept to the Yield Strength, there is a fundamental difference. While the proportional limit is the point on the stress-strain curve where the linear relationship between stress and strain ends, the yield strength is the stress level at which a material undergoes a significant and permanent increase in strain without any additional increase in stress.

Furthermore, the proportional limit is often determined by observing the stress-strain curve and identifying the point at which the linearity ends. In contrast, the yield strength is usually determined by identifying a specific amount of plastic deformation, typically a 0.2% or 0.1% offset from the linear elastic portion of the stress-strain curve.

The incorporation of the proportional limit, along with Young's Modulus and the UCS, plays a fundamental role in establishing the elastic and mechanical characteristics of materials and rocks.

Table 6: The table displays the measured data for UCS, Es and σp across all meteorites examined within this study.

ID	UCS [MPa]	E_s [GPa]	σp [MPa]
MUR.2021.001.07	63.4	10.4	50.0
MUR.2021.001.10	96.3	9.6	67.0
MUR.2021.001.11	82.9	10.3	46.0
MUR.2021.001.12	34.0	6.9	18.5
MUR.2021.001.13	121.4	13.6	80.0
MUR.2021.001.14	50.4	10.6	
BUZ.001.02.2022	227.5	23.4	195.0
BUZ.001.04.2022	162.5	21.3	135.0
GOLD.001.03.2022	36.6	3.8	32.0
GOLD.001.05-1.2022	32.5	3.1	21.0
GOLD.001.05-2.2022	43.9	5.2	39.0

ABE.001.03	545.9		
ABE.001.04	556.4		
ABE.001.05	610.6		
ABE.001.06	609.5		
TAG.001.02.2022	10.36	0.5	7.9
TAG.001.03.2023	6.69	0.4	5.3
MOSS C1	27.8		
MOSS C2	22.3		
MOSS C3	27.2		

3.5 Direct Shear Strength (τ)

Here we present the shear direct shear strength results for the meteorites in this study (Table 7). No previous direct shear test on meteorites have been published to date to our knowledge.

Shear strength is an important parameter used in various fields, including geotechnical engineering, structural engineering, materials science, and mechanical engineering.

Primary it is used for slope stability analysis to evaluate the stability of slopes and embankments. It helps determine whether the shear stresses acting on a slope exceed the shear strength of the soil or rock, which could result in slope failure or landslides. [e.g., Barton, 2013]

Also, Shear strength is crucial in assessing the bearing capacity of soils or rocks beneath foundations. It helps engineers determine the maximum load that a foundation can support without experiencing excessive settlement or failure.

As for the UCS, the shear strength is measured with different techniques and boundary conditions depending on the application [e.g., MacDonald et al., 2023]. The shear strength in this study is considered a uniaxial direct shear strength.

In planetary science shear strength plays crucial roles in modelling asteroid geology. Different papers discussed the role of shear strength for impact cratering process on asteroid at different scale and target properties [e.g., Nolan et al., 1996; Housen et al., 2018].

Table 7: The table displays the measured data for DSS of all meteorites examined within this study.

ID	Direct Shear Strength [MPa]
MUR.2021.001.01	7.3
MUR.2021.001.02	13.9
MUR.2021.001.03	16.6
MUR.2021.001.04	7.1
MUR.2021.001.05	32.2
MUR.2021.001.06	30.1
MUR.2021.001.08	34.8
MUR.2021.001.09	29.4
BUZ.001.01.2022	35.8
BUZ.001.03.2022	59.7

GOLD.001.01.2022	18.4
GOLD.001.02.2022	6.4
GOLD.001.04.2022	10.6
GOLD.001.05-3.2022	11.4
GOLD.001.05-4.2022	10.3
ABE.001.01	129.2
ABE.001.02	122.7
ABE.001.07	148.4
TAG.001.01.2022	1.59
TAG.001.04.2023	2.24
TAG.001.05.2023	2.2
MOSS S1	10.7
MOSS S2	8.3

3.6 Elemental Compositions (X-Ray Florescence (XRF))

Here we present the elemental composition measured with the ED-XRF for our meteorite collection (Table 8).

The elemental compositions of the meteorites in this study have been reported in the literature, except for the Golden Meteorite, which has only recently been recovered.

However, previous meteorite literature has never measured the elemental composition in relation to mechanical and elastic properties. Among the properties examined in this study, the elemental composition is the most measurable from orbit and is it directly related to the

mineralogy. Consequently, comprehending the influence of major elements on these properties might provide valuable insights into the mechanical and elastic properties of the parent asteroids.

Table 8: The table displays major elemental compositions of all the sample measured in this study.

ID	Mg [%]	Al [%]	Si [%]	S [%]	Ca [%]	Fe [%]	Ni [%]
MUR.2021.001.08	9.8	1.1	11.5	1.8	0.9	23.2	1.3
MUR.2021.001.11	11.7	1.3	14.1	2.4	1.3	22.9	1.2
MUR.2021.001.12	8.8	0.9	10.4	2.3	1.6	23.2	1.3
MUR.2021.001.14	11.9	1.3	13.6	2.8	1.2	22.5	1.2
BUZ.001.01.2022	15.3	1.9	21.7	1.3	1.7	18.2	0.4
BUZ.001.02.2022	15.3	1.8	21.3	1.5	1.4	22.8	0.6
BUZ.001.03.2022	16.1	1.8	22.5	2.0	1.4	22.0	0.5
BUZ.001.04.2022	16.9	1.9	24.0	1.7	1.7	21.2	0.5
GOLD.001.01.2022	13.0	2.0	20.4	1.0	1.5	19.3	0.3
GOLD.001.02.2022	13.0	2.0	20.5	1.4	1.4	18.9	0.2
GOLD.001.03.2022	13.1	2.3	19.9	1.0	1.4	18.6	0.3
GOLD.001.04.2022	12.8	2.0	19.0	0.8	1.2	18.8	0.3
GOLD.001.05-1.2022	12.6	1.9	20.0	1.3	1.4	19.4	0.4
GOLD.001.05-2.2022	12.7	2.0	19.8	1.5	1.4	18.9	0.5
GOLD.001.05-3.2022	13.2	2.2	19.9	1.6	1.3	20.2	0.4
GOLD.001.05-4.2022	13.8	2.2	20.6	1.7	1.5	20.8	0.4

ABE.001.01	13.3	1.6	24.4	6.2	0.5	26.0	0.8
ABE.001.02	13.0	1.6	23.5	6.0	0.5	25.2	0.8
ABE.001.03	12.5	1.6	23.3	5.7	0.9	26.4	0.8
ABE.001.04	11.7	1.4	21.2	4.8	0.8	28.0	1.0
ABE.001.05	14.0	1.3	24.5	4.6	0.5	23.7	0.7
ABE.001.06	14.9	1.4	24.7	5.2	0.6	24.6	0.7
ABE.001.07	13.7	1.2	20.4	4.3	0.8	24.7	0.8
MOSS C1	12.4	1.6	14.7	0.7	1.7	28.0	1.1
MOSS C2	14.7	1.8	16.8	0.8	1.7	27.1	1.0
MOSS S1	12.3	1.6	14.6	0.8	1.3	26.1	1.0
MOSS S2	13.7	1.7	15.8	1.0	1.5	27.1	1.0

4. DISCUSSION

This chapter discuss the implications, significance, and limitations of the study. It offers a comprehensive understanding of the results and provides insights for future research.

4.1 Porosity: suggested terminology for asteroids

Before discussing the porosity, grain density and bulk density of the studied samples, porosity (and its theoretical and practical limitations) in rocks needs context/definition as porosity definitions and referencing terminology vary amongst different research fields.

Among solids in three-dimensional space/rocks, cubic packing is the least efficient arrangement for clast packing. In perfect cubic packing, the maximum achievable porosity is 47.6% for spheres of uniform size, regardless of clast size [e.g., Hook, 2003]; the minimum achievable porosity is 26% in perfect rhombohedral packing. However, 1) nonspherical clasts with 2) an extended size distribution may theoretically have much lower porosities (approaching zero); having these two conditions makes consideration of of cubic or rhombohedral packing as notionally to be expected on asteroids somewhat irrelevant. The extent of (frictional) forces between clasts as they assemble becomes more relevant as the interclast forces limit the extent to which their packing approaches the tightest possible arrangement. It is expected that asteroidal rubble material at the scale of hand samples has a theoretical maximum porosity of 47.6%. However, it should be noted that unconsolidated fine-grained regolith on airless bodies may exhibit significantly higher porosity [e.g., Szabo et al., 2022] because interclast forces become proportionally stronger relative to the clasts' masses.

Porosity, in essence, is a straightforward concept. However, due to the various methods used to measure it, it can refer to different realities. Frequently, the same terminology is employed to convey different meanings, often contingent upon the user's technical background. In the field of planetary science, which brings together scientists from various technical backgrounds, this variability in interpretations is evident in the literature discussing porosity. When discussing the porosity of meteorites or asteroids (rocky bodies), it is germane to refer to the geological definition of porosity.

One significant aspect that has not received sufficient attention in previous planetary science literature is the distinction between total, connected and effective porosity. Total porosity encompasses all pore spaces, whether connected or not, while connected porosity solely refers to the interconnected pores. The term "effective porosity" is occasionally used interchangeably with connected porosity; however, it is a more specialized term typically used in oil and gas reservoir geology, defined as the porosity connected "free of fluids" [e.g., Hooke, 2003]. In this study, as mentioned in the methods chapter, because of the technique used, we are limited to measuring connected porosity which we describe as porosity as significant amounts of unconnected pores have not been found in meteorites.

The use of the terms “macro-” and “microporosity” potentially adds to confusion within the research community because these terms refer to a specific nomenclature. The terms are defined by the International Union of Pure and Applied Chemistry (IUPAC) nomenclature [e.g., Sing et al., 1984; Thommes et al., 2015]. According to IUPAC, pores with widths exceeding about 50 nm are called macropores, pores of widths between 2 nm and 50 nm are called mesopores and pores with widths not exceeding about 2 nm are called micropores; the term nanopore is also defined and embraces the above three categories of

pores, but with an upper limit ~ 100 nm [Thommes et al., 2015]. This classification is also widely accepted in the field of geology [e.g., Anovitz and Cole, 2015]. Hence, it is useful to reduce potential ambiguity by using the terms “micro-porosity” or “macro-porosity” in accordance with their specific pore size ranges also in the field of planetary science when describing meteorites.

In addition, various geological terms have been employed in the field of geology to describe porosity (matrix porosity, intergranular porosity, interparticle porosity etc.), considering both the rock type and the temporal and spatial factors influencing its formation or modification [e.g., Choquette and Pray, 1970].

In figure 4.1 we propose a potentially unambiguous way to define asteroid porosity in the case of rubble-pile asteroids (figure 4.1, A) and monolithic asteroids (figure 4.1, B).

The porosity within the clasts that make up a rubble pile asteroid is referred to as “intraclast porosity”. It corresponds to the term “microporosity” found in current asteroid literature [e.g., Britt et al., 2002]. The geological term "clast" does not refer to a specific size, allowing for a broad description of the porosity present within the clasts in the rubble pile.

On the other hand, the empty space between the clasts that constitute a rubble pile asteroid is referred to as “interclast porosity”. It is equivalent to the term “macroporosity” used in asteroid community studies of recent decades. The appropriately combined numeric values of asteroid intraclast and interclast porosities (intraclast porosities apply only to the asteroid fractional volume that is occupied by clasts) define the asteroid total (or bulk) porosity. In the case of a monolithic asteroid, the asteroid total porosity is equivalent to the intraclast porosity.

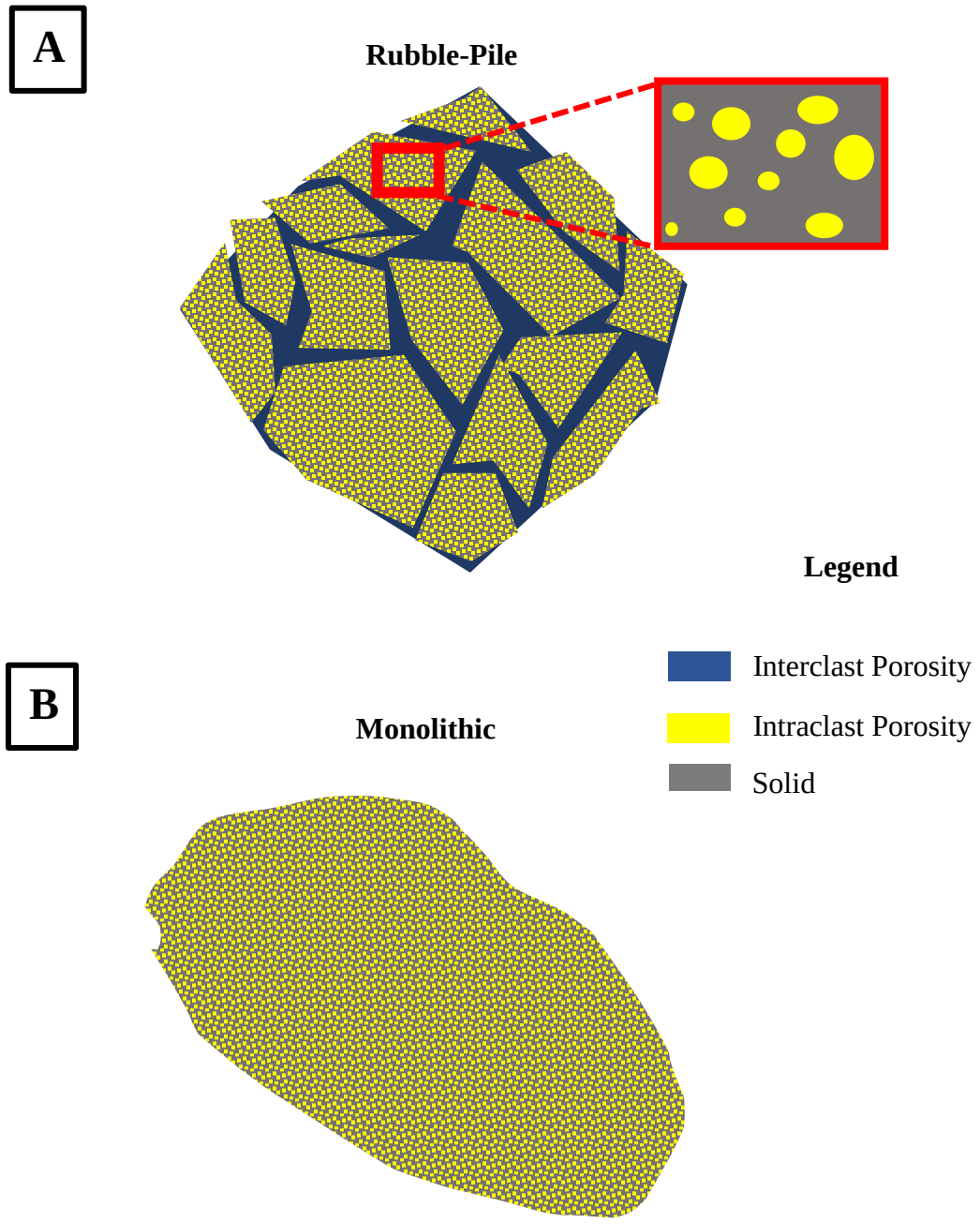

Figure 4.1: schematic of the definition of asteroid porosities for rubble-pile (A) and monolithic (B) asteroids.

4.2 Porosity, Bulk Density and Grain density

Murchison (CM)

Individual splits of the Murchison meteorite individual studied exhibited a range of bulk density values between 2.32 g/cm^3 and 2.44 g/cm^3, while the range of grain density values fell between 2.82 g/cm^3 and 2.94 g/cm^3. The average bulk density measured was 2.4 g/cm^3, and the average grain density was determined to be 2.91 g/cm^3.

The ranges and averages of bulk and grain densities determined in this study are consistent with the measurements obtained for the CM chondrites, as reported by Macke et al., 2011. The average bulk density measured in this study slightly surpassed the average of 2.31 g/cm^3 reported by Macke et al., 2011 for Murchison. On the other hand, the grain density is slightly lower than the average value of 2.96 g/cm^3 observed by Macke et al., 2011 for Murchison. Several factors may contribute to these differences (although the few percent difference isn't much larger than instrument uncertainty of our pycnometers):

1- Murchison is a breccia, implying that the variations in average values could be attributed to the heterogeneous nature of the Murchison breccia itself.
2- Differences in the weathering state of different Murchison meteorites might also influence the measured densities as the meteorite fell a half century ago and has been curated at different locations. It is well-established that weathering plays a significant role in influencing densities [e.g., Otrowsky and Bryson, 2019].
3- Discrepancies in the instrument calibrations and techniques (e.g., 3D laser scanner; Archimedes, calipered dimensions) employed by different studies (He vs. N gas) could contribute to the observed differences in density measurements.

When we consider the grain and bulk densities at different prepared sample sizes we notice a possible trend in our samples (Figure 4.2). The bulk density increases with sample size from an average of 2.36 g/cm^3 for the 2.5x2.5 mm cubes, to 2.39 g/cm^3 for the 5x5 mm cubes and to 2.42 g/cm^3 for the bigger cuboids. The average of all samples is close to the average measured just for the parent irregular sample of 2.41 g/cm^3 that is closer to the average measured for the cuboids. This implies that bulk density of samples smaller than or equal to 5 x 5 x 5 mm may not accurately represent the meteorite/parent body; this could be due to artifacts from cube preparation, such as small surface plucks, rather than any

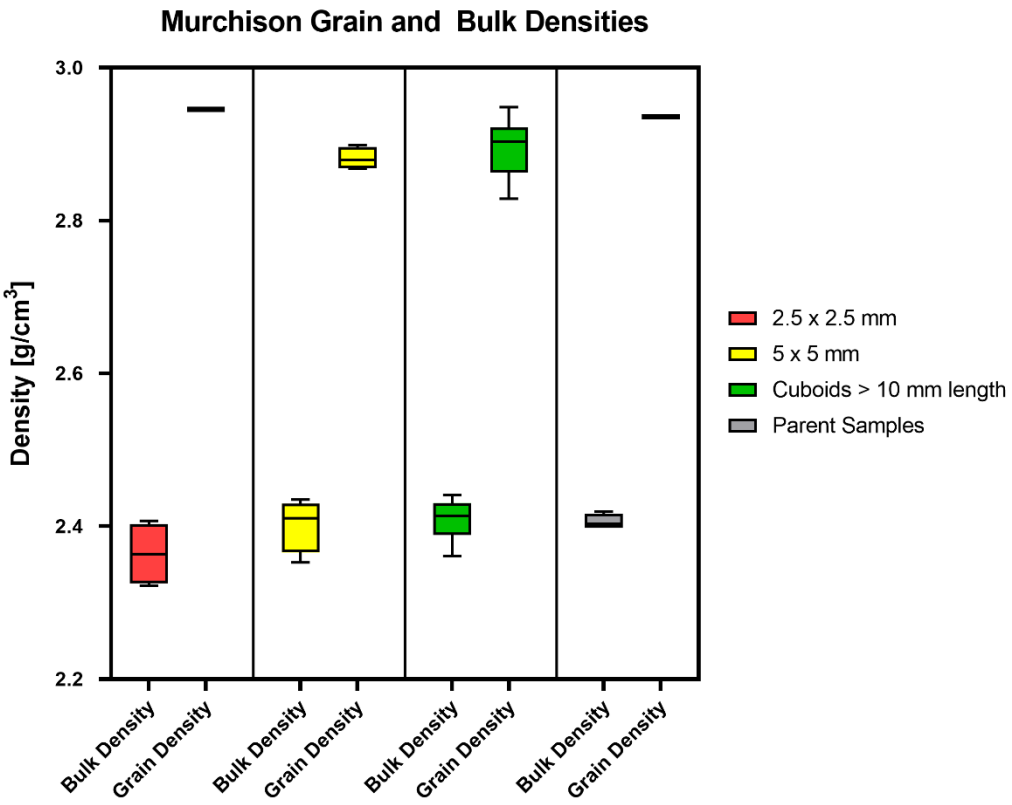

Figure 4.2: The figure presented is a box & whiskers plot illustrating the grain and bulk densities measured for all the samples of Murchison meteorite. The measurements have been grouped based on samples' sizes. The bars represent the range (Min and Max value).

material characteristic (and may reflect the inherent difficulty of working with small samples).

The grain densities show an opposite trend (Figure 4.2). The grain densities decrease with increasing the size from an average of 2.95 for the 2.5x2.5 mm cubes to 2.88 for the 5x5 mm cubes. The cuboids (> 10 mm in length) show instead an average of 2.91 that is very close to the total average of all the samples. As for the bulk density, the grain density of Murchison samples of sizes equal or less and 5 x 5 x 5 mm may be affected by sample preparation artifacts that result in overestimation of volume.

The average porosity of Murchison is approximately 17.6%. This value is quite similar to the average porosity of 17% reported for all carbonaceous chondrites but lower than the average of 24.7% for the CM chondrites [Otrowsky and Bryson, 2019].

The porosity range observed for Murchison samples spans from 15.1% to 19.3%. It is worth noting that the average porosity measured is significantly lower from that reported by Macke et al., 2011 for Murchison occurring at the lower end of their range. Macke et al. found the average porosity to be 22.1%, with a range of 18.7% to 24.9%. This difference, like those for the grain and bulk density, could be attributed to different factor like the brecciated nature of Murchison, and the weathering state of the samples.

When looking at porosity at different sample sizes (Figure 4.3), the smallest 2.5 x 2.5 mm cubes show the highest average porosity of 19.3 % while the 5 x 5 mm show the lowest of 16.6 % and the biggest range among size classes between 15.7 % to 18 %. The cuboids > 10 mm in length show an average porosity of 16.8 % that is lower than the average of all the samples. If we exclude the smallest cubes (2.5 x 2.5 mm) the average porosity for all

the samples would be 17.1% that is close to the average measured for the biggest cuboids. This might suggest that the biggest cuboids (> 10 mm in length) better represent porosity at meteorite scale.

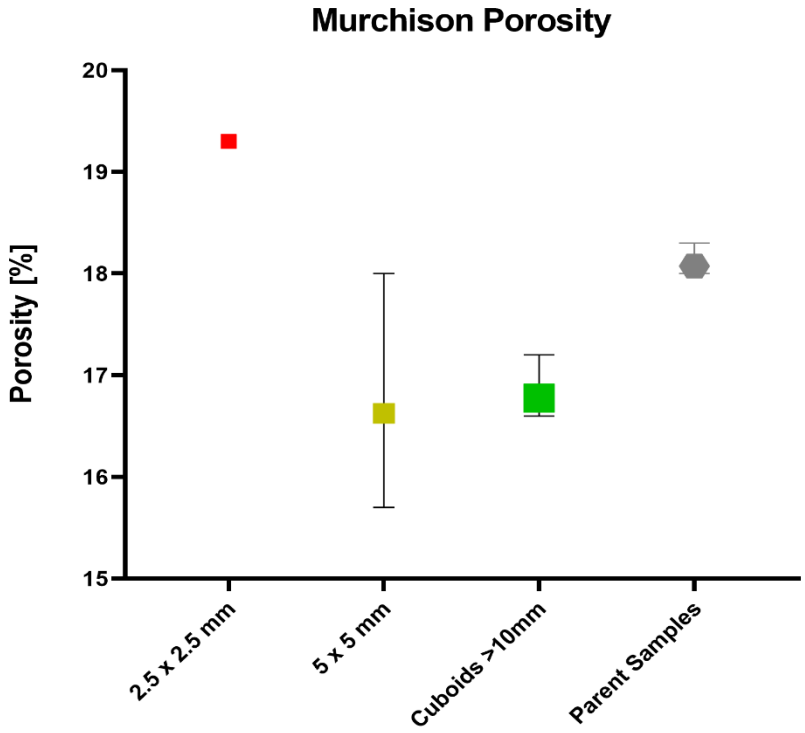

Figure 4.3: The plot illustrates the relationship between porosity and class size. Each symbol on the plot represents the average value for a particular class size, while the bars depict the range of all measurements within each class size.

Murchison shows an inclusion-rich texture with coarse inclusions in a fine-grained matrix. The inclusions are often porous and weak suggesting that the porosity variations may reflect sample sizes too small to average the bulk matrix to inclusion ratio.

Moss (CO)

The measured Moss average bulk density is 2.93 g/cm^3 while the average grain density is 3.73 g/cm^3. The bulk density range is between 2.91 g/cm^3 to 2.94 g/cm^3 while the range for the grain density is 3.72 g/cm^3 to 3.74 g/cm^3.

The average Moss bulk density reported for one sample by Macke at al., 2011 is 3.04 g/cm^3 that is significantly higher than the value and range obtained in this study. On other hand, the grain density is almost the same, 3.74 g/cm^3. The fact that the grain density is the same, but the bulk density lower could reflect minor heterogeneities in the parent meteoroid rather than other factors (e.g., weathering state) – Moss fell July 14, 2006, and was rapidly recovered.

The average porosity measured in this study is 21.5 % and ranging from 21 % to 22.2 %. This number, as expected by the lower bulk density (and same grain density), is significantly higher that the value reported by Macke at al., 2011 of 18.6%. Moss parent meteoroid could have been significantly heterogenous in porosity at the meteorite scale while having a relative uniform mineralogical composition.

Both densities and porosities are within the range reported for the other CO falls [Britt and Consolmagno, 2003; Macke et al., 2011b].

Tagish Lake (C2-Ungrouped)

Tagish Lake samples in this study measured an average bulk density of 1.54 g/cm^3 and a range between 1.50 g/cm^3 to 1.60 g/cm^3. Both average and range are lower than what previously reported by Hildebrand at al., 2006 (1.64 g/cm^3 and 1.58-1.71 g/cm^3 respectively).

The average grain density is 2.85 g/cm^3 that is higher than average value of 2.71 g/cm^3 previously reported by Hildebrand at al., 2006. However, the range measured in this study between 2.81 g/cm^3 to 2.89 g/cm^3 is in good agreement with the upper range of 2.56-2.91 g/cm^3 measured by Hildebrand et al., 2006.

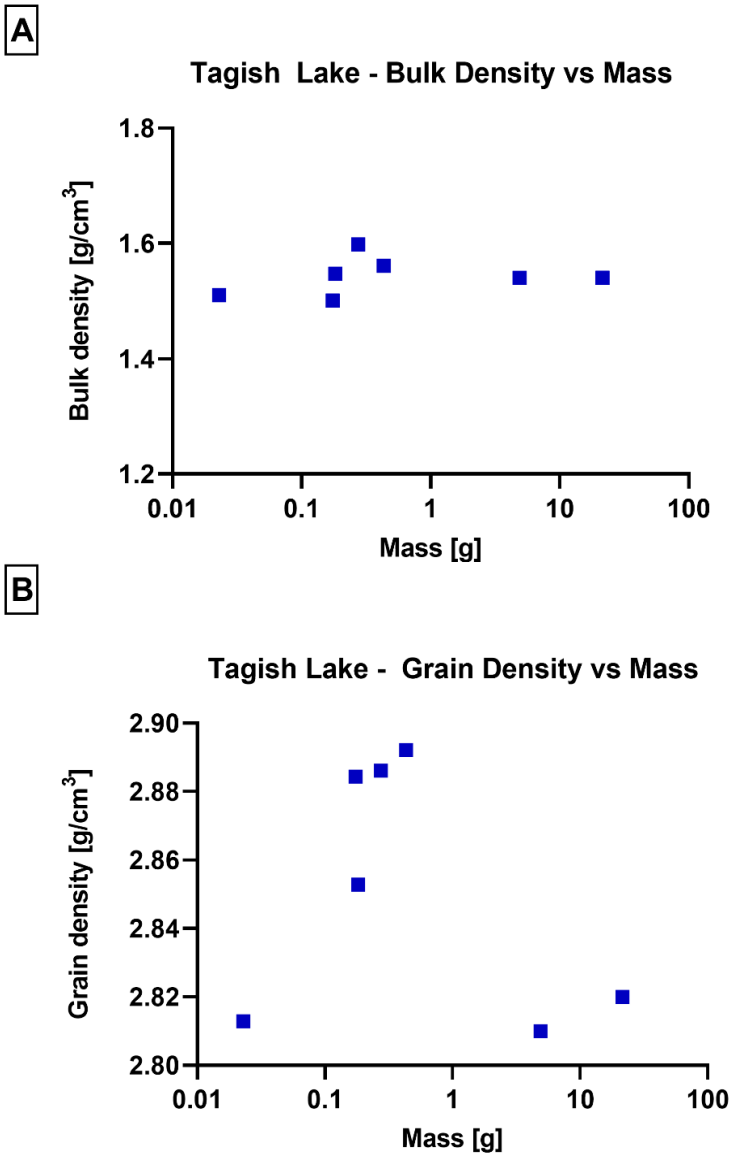

Figure 4.4: A) the plot show the bulk density of Tagish Lake vs the size expressed as mass. B) the plot show the grain density of Tagish Lake vs the size expressed as mass.

No particular trends of bulk/grain density and size has been observed for Tagish Lake (Figure 4.4).

Tagish Lake has an average porosity of 46%, with a range of 45.7% to 48%. The porosity measurements obtained in this study, both in terms of average and range, deviate

significantly from those previously reported in the literature by Hildebrand et al. (2006), who recorded a mean value of 39.3% and a range of 35% to 42%, respectively. The relatively high porosity and low density measured in these Tagish Lake samples can be attributed to their 1) significant fracturing and 2) small size. The much larger (up to ~110 g) Tagish Lake individuals measured by Hildebrand et al. were relatively pristine – some not having been exposed to liquid water; the samples measured in this study had been water saturated after their fall so that the saponite clay had gone through at least one expansion-contraction cycle leading to commonly observed shrinkage cracks in the curated specimens. The water-cycled meteorite is particularly friable so prepared cubes often showed some surface plucking (so measured volumes would be slightly too large). Finally, the once water saturated samples show lower concentrations of Na, H, Cl, and Br suggesting minor mineral components had been leached (Alan Hildebrand, P.C.). The discrepancies in discussed measured values could all result from the cuboids' volumes being slightly too large due to these effects and the those measured on the larger pristine samples are more likely to be representative.

Hildebrand et al. (2006) used glass beads to calculate the sample volume, whereas this study utilized a laser scanner or caliper measurements for regular-shaped samples. The use of glass beads may have resulted in an overestimation of volume due to the wall effect although the large size (83.7 to 110.2 g) of the pristine Tagish Lake samples would have minimized this effect.

Tagish Lake is a breccia. The discrepancies observed between the studies may be also attributed to the inherent variability present within the Tagish Lake breccia.

In comparison to meteorites from other groups, Tagish Lake exhibits the highest porosity among all falls, making it a possible candidate for representing the upper limit of intraclast porosity in asteroidal material. The grain density falls within the range of 2.57 to 2.87 g/cm³, consistent with CM chondrites [Britt and Consolmagno, 2003]. Notably, Tagish Lake possesses the lowest bulk density among all meteorite groups. Consequently, Tagish Lake may represent the extreme limits of both bulk density and porosity for meteorites that can survive atmospheric entry.

Buzzard Coulee (H4)

Buzzard Coulee recorded an average bulk density of 3.45 g/cm³ and a range of 3.41-3.50 g/cm³. The average grain density is 3.71 g/cm³ and the range is 3.68-3.72 g/cm³. The average porosity is 7 % and the range is 5.9-8.3%.

The bulk and grain density values, as well as the porosity, obtained in this study are consistent with the averages and ranges reported in previous literature for Buzzard Coulee [Fry et al., 2013]. This agreement suggests that the parent meteoroid of Buzzard Coulee was relatively uniform in composition and physical properties.

The bulk and grain density, as well as the porosity, measured for Buzzard Coulee, align well with the range reported among other H chondrites [e.g., Britt and Consolmagno, 2003].

Golden (L/LL)

Golden is a remarkably fresh and recent meteorite fall (fell Oct. 3, 2021), exhibiting minimal degrees of terrestrial weathering (the individual studied was recovered one week

after its fall). This characteristic enhances its value for scientific study, as the properties observed in Golden are expected to closely resemble those of its parent asteroid.

Golden meteorite recorded an average bulk density of 3.10 g/cm³ and a range of 3.05-3.13 g/cm³. The average grain density is 3.56 g/cm³ and the range 3.53-3.61 g/cm³.

Golden average porosity is 13.0% and the range is 11.8-14.4%.

Compared to the L and LL chondrites, Golden has the same grain density average recorded for all the L falls of 3.56 g/cm³ while the bulk density is in good agreement with the lower limit measured for the LL chondrites of 3.09 g/cm³ [Consolmagno et al, 2008]. The average porosity however is higher than both L and LL chondrites (5.6 % and 8.2 % respectively) but in agreement with the upper limit measured for the LL of 13.7 % [Consolmagno et al., 2008].

Golden meteorite falls within the range of physical properties that correspond with its classification, occupying a position between the L and LL meteorites. Nevertheless, it stands out as having the highest porosity among the LL and L falls. This remarkable characteristic could be attributed to the meteorite's exceptionally pristine condition, which enhances possible validity of the measured data. Alternately, the chondrites generally show a range of porosities that may reflect as yet unknown parent body processes.

Abee (EH)

The average bulk density measured for Abee is 3.53 g/cm³ and the range is 3.38-3.67 g/cm³. The average grain density is 3.63 g/cm³ and the range is 3.52-3.78 g/cm³.

Both Abee's average grain and bulk density are in good agreement with the data reported previously in literature, respectively 3.63 g/cm³ and 3.50 g/cm³ [Macke et al., 2010]. The ranges of bulk and grain density are also in good agreement with the ranges reported previously in literature for the EH chondrites by Macke et al., 2010.

Abee measured an average porosity of 2.7 % and a range of 1-4.5%. This is in good agreement with the average porosity of Abee reported by Macke et al., 2010 of 3%.

To assess the heterogeneity within the Abee breccia, cubes and cuboids were cut from different sources, including clasts, matrix, and one specifically from a clast/matrix boundary.

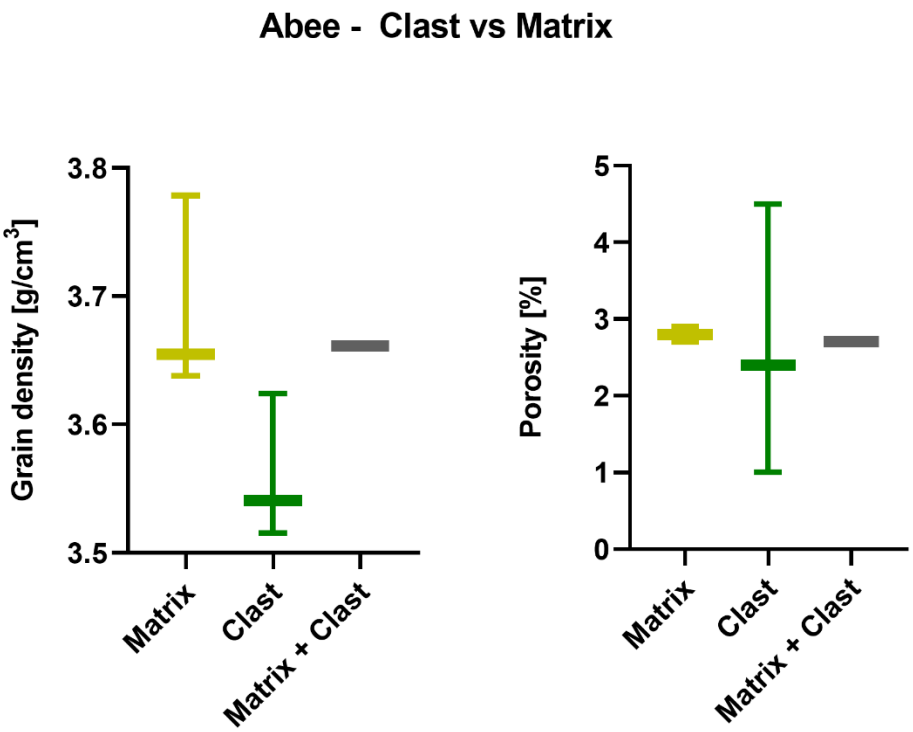

Figure 4.5: The figure depicts the disparities in densities and porosities between the clasts and the matrix in Abee breccia. The left plot presents the average (represented by a horizontal line) and the ranges (indicated by bars) of grain density. The right plot displays the average and range of porosity.

The grain density of the matrix is significantly higher than that of the clasts (refer to Figure 4.5). Additionally, both the matrix and clasts exhibit relatively large ranges in their respective grain densities.

On the other hand, while the average porosity of both clasts and matrix is similar, there is a notable difference in their respective ranges. The Abee matrix displays a higher level of uniformity in porosity compared to the clasts, which exhibit a significantly broader range of porosity values.

The variation between clasts and matrix is further evident in the bulk chemical composition measured with XRF in this study (refer to Figure 4.6). When examining major elements, Abee displays a distinct separation between clasts and matrix (same clast and matrix cuboids and cubes used to measure porosity and grain density), particularly in terms of S % and the Mg/Fe ratio (refer to Figure 4.6).

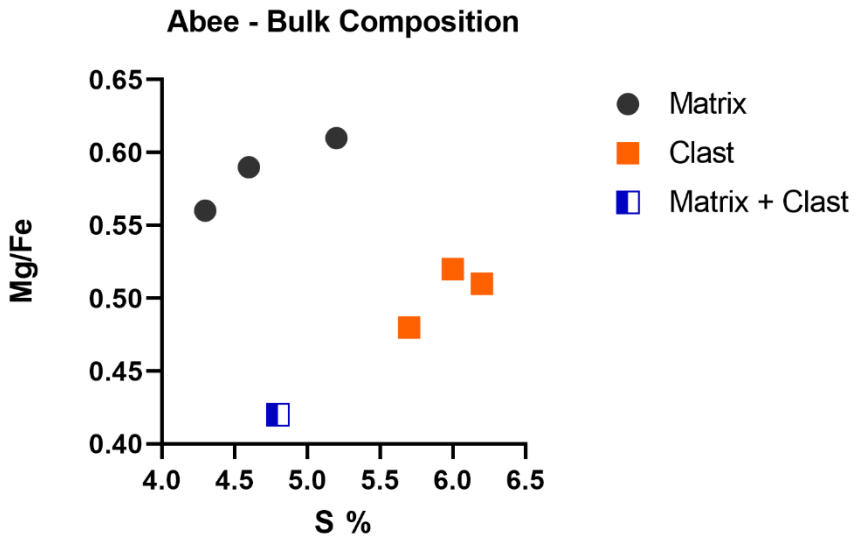

Figure 4.6: the plot illustrates variations in elemental composition (Mg/Fe and S) among the Abee clast, matrix, and clast/matrix boundary. The elemental composition data is also derived from this study.

4.2.1 Comparing densities and porosities.

The meteorite lithologies analyzed represent a range of parent-body compositions and "geologic" histories. The comparatively low grain densities of Tagish Lake and Murchison reflect their history of parent body hydrothermal alteration and resulting hydrated mineralogy. However, their porosities differ significantly possibly due to its more extensive alteration, with Tagish Lake being the most porous meteorite in this group (refer to Figure 4.7). As already discussed in previous literature, carbonaceous chondrites, particularly the hydrated lithologies, are notably distinct from other groups due to their higher porosity, and this will significantly influence elastic and strength properties.

As the other carbonaceous chondrite, Moss displays a grain density comparable to that of ordinary chondrites (Golden and Buzzard Coulee) and Abee (EH) due to relatively mild hydration. Nevertheless, it possesses the second highest porosity among the meteorites examined in this study (refer to Figure 4.7).

The ordinary chondrites have relatively similar silicate mineralogy such that Buzzard Coulee exhibits a grain density that falls within the range of Abee and Golden, but it displays a slightly higher porosity than that of Abee while Golden has a significantly higher intraclast porosity than both. The controls on intraclast porosity in ordinary chondrites remain to be understood. (Figure 4.7)

Interestingly, both Abee and Murchison, being distinctly brecciated meteorites, exhibit the widest range in both intraclast porosity and grain density. This substantial range may be a tentative indicator of the significant heterogeneity present within the breccias.

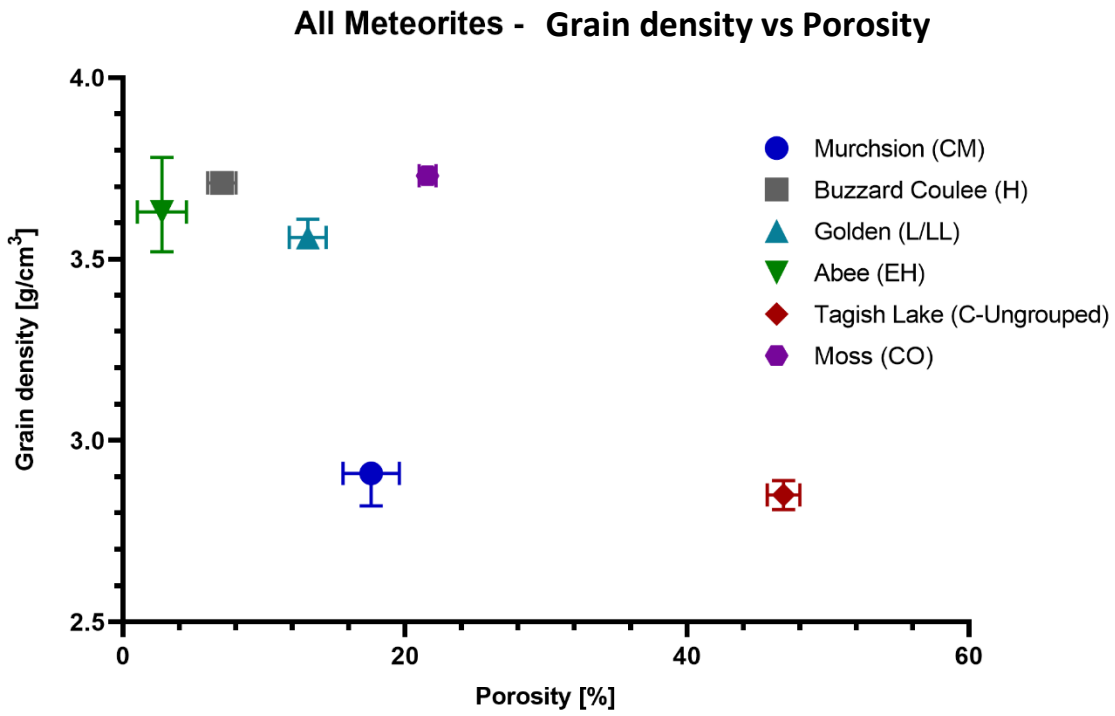

Figure 4.7: The figure illustrates the variations in grain densities and porosities among the meteorite groups in this study. The bars display both the range of porosity and grain density for each meteorite.

4.4 Seismic Velocities

P-waves and S-waves are two fundamental types of elastic body waves. P-waves, also called compressional waves, travel by causing particles to move in the same direction as the wave's propagation. They are the fastest seismic waves and can travel through both solid and fluid mediums. On the other hand, S-waves, known as shear waves, move particles perpendicular to the direction of propagation. These waves cannot travel through fluids and are slower than P-waves, but they provide valuable information about a medium's structural properties.

By studying seismic velocities in meteorites, we can derive essential material properties such as dynamic Poisson's ratios, Shear modulus, and Young's modulus. These characteristics provide valuable insights into the structural and mechanical properties of meteoritic materials.

In this study, we conducted measurements of seismic velocities in meteorites along three orthogonal directions whenever feasible, to assess possible anisotropy. This approach has not been utilized in prior literature, but it holds fundamental importance in comprehending the diverse mechanical and elastic responses exhibited by meteorites/parent asteroids.

4.4.1 Elastic response and stress orientation

While in some cases the velocities of seismic waves are isotropic, the values can change based on the orientation of the geological features through which the waves are traveling. This anisotropic behavior is commonly observed in certain types of rocks and sediments, particularly in layered or fractured formations at all scales (up to regional scale).

Seismic velocities are intricately connected to the elastic properties of materials, and the way rocks respond to mechanical and elastic stress is contingent upon the orientation of the stress itself. In the case of seismic velocities, this orientation of stress is directly related to the direction of wave propagation.

Figure 4.9 presents the measurements of Vp (A) and Vs (B) obtained along three orthogonal directions. To enhance the visualization of the data's variability and mean values for each propagation direction, we have ordered the data from fastest to slowest and then binned them to create the box and whisker plots. This method provides a clearer

representation of the distribution of data points and allows for a more insightful analysis of the measurements in different directions of propagation.

Among the meteorites studied, Abee exhibited the highest recorded speeds for both P-wave and S-wave. As detailed in the following section, these high speeds are primarily associated with the low porosities observed in the Abee samples. While investigating the discrepancies between clasts and matrix, clear distinctions in seismic velocities are not apparent. However, the matrix demonstrates the most significant variation compared to clasts; this disagrees with the differences seen in the porosities where the matrix appears to be more uniform (Figure 4.8).

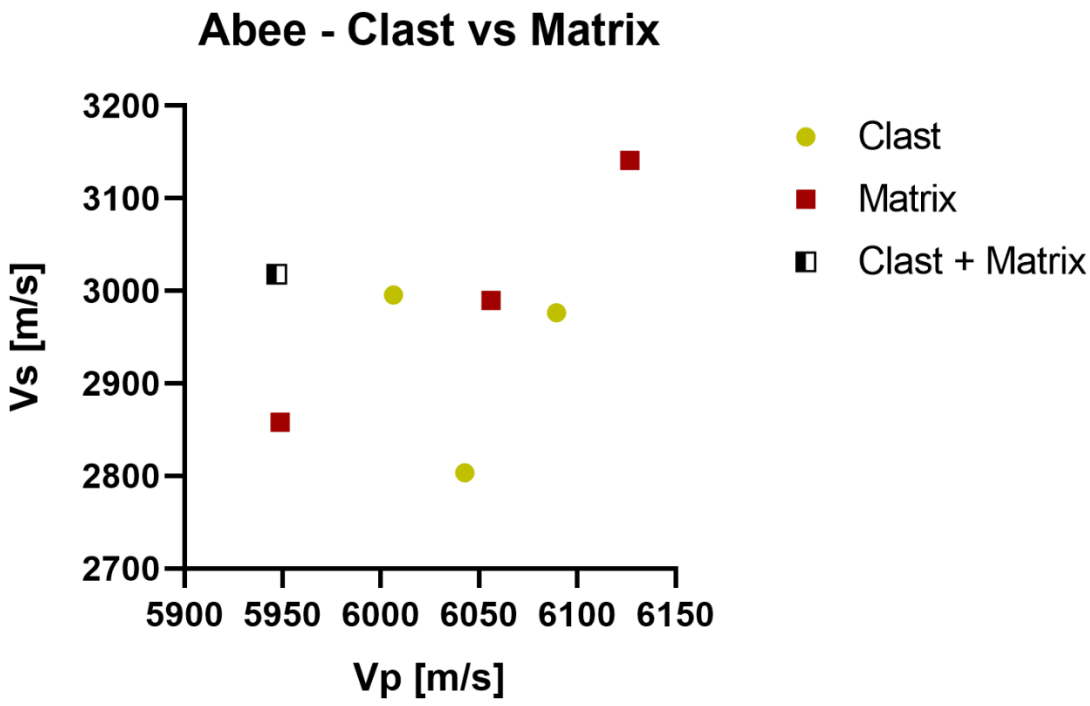

Figure 4.8: the plot illustrate the Vp vs Vs measured for Abee clast (yellow), matrix (red) and clast/matrix boundary (black). Not a significant difference has been observed between these different components for Vp and Vs.

On the other hand, due to its extremely high porosity, Tagish Lake exhibited the slowest velocities for both P and S waves. Interestingly, seismically, due to its grater porosity, Tagish Lake is notably distinct from Murchison, a CM meteorite that shares mineralogical affinities.

Although Tagish Lake's S-wave velocities are more similar to those of Golden and Moss, which have significantly different mineral compositions, it suggests that mineralogy is not the primary discriminant affecting seismic velocities. Golden and Moss display varying porosities, indicating that porosity itself, while correlating with seismic velocities as described in the next section of this chapter, is not the sole contributing factor.

Upon analyzing the velocities along three orthogonal directions, we observe that Golden and Moss exhibit the most notable variations. In the case of Golden, the differences are most likely to be statistically significant. However, when it comes to Moss, we would require more data to draw a definitive conclusion. Currently, only one sample of Moss has been measured along the three directions, which is insufficient to establish a robust assessment of its velocity variations.

Abee also exhibits a prominent slowest direction with a substantial range of speeds. Given that there are no clear distinctions in seismic velocities between clasts and matrix, the slowest direction observed in Abee may be linked to a uniform structural feature within the parent meteoroid/body. This uniform structural characteristic could be responsible for the variations in seismic velocities along this specific direction (e.g., preferred orientation of minerals/pores; pore size distributions; pore connectivity; fractures)

When considering the overall variability in the data, it is evident that Buzzard Coulee stands out as the most heterogeneous in terms of seismic velocities (this meteorite has a cryptic breccia texture). However, despite this significant variability, the average velocities for each direction are very similar.

Among the meteorites in this study, particularly the ordinary chondrites and Abee, appear to exhibit greater heterogeneity compared to the carbonaceous chondrites.

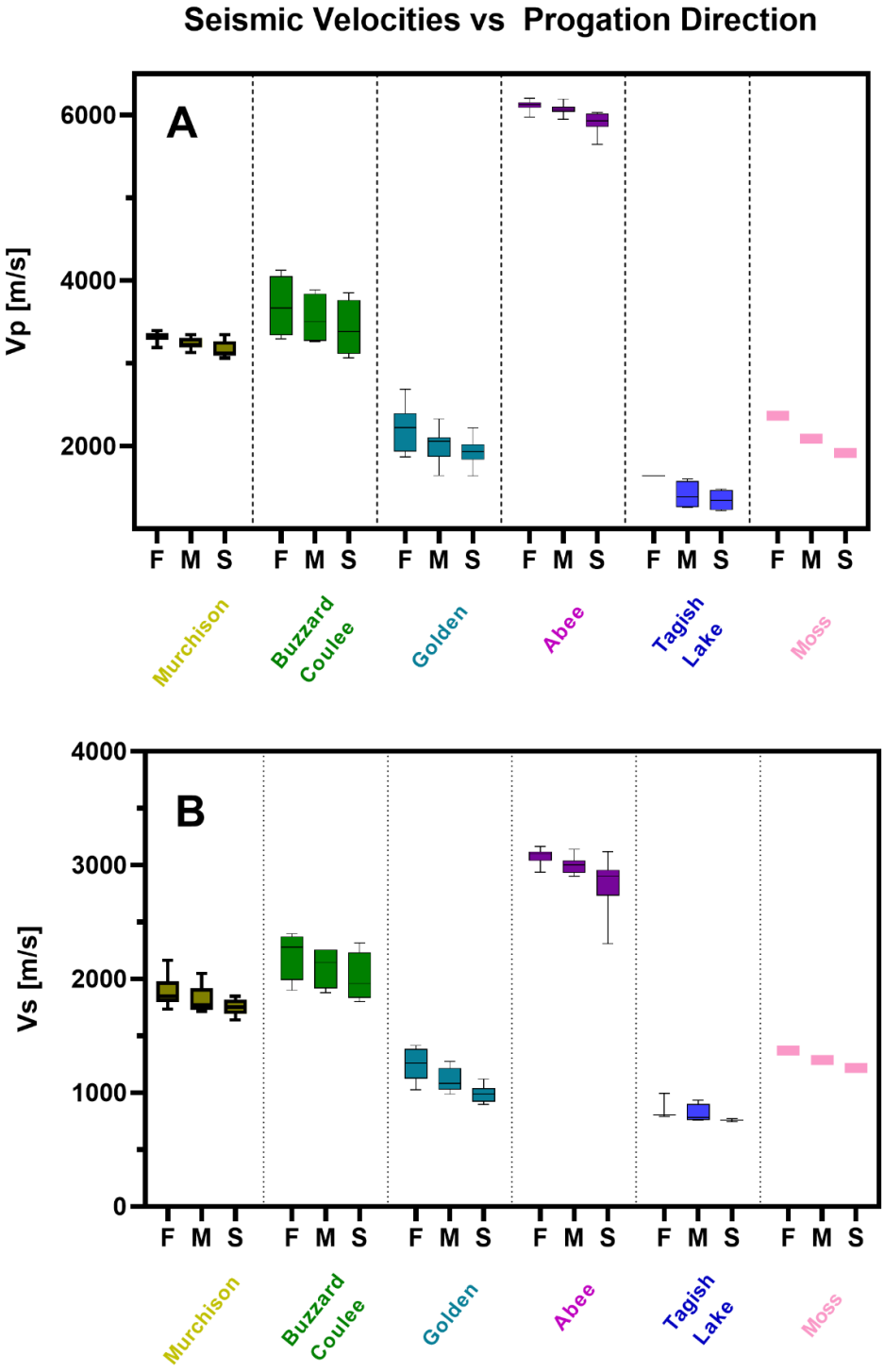

Figure 4.9: The illustration consists of box and whisker plots representing the measured Vp (A) and Vs (B) values for each meteorite. The data for each sample has been categorized into three groups based on their Vp and Vs measurements: fast (F), medium (M), and slowest (S).

4.4.2 Porosity correlates with Seismic Velocities

The compressional wave velocity is generally lower in more porous rocks due to the slower transmission of wave energy through the "empty" spaces present in the rock matrix. In contrast, in a more compacted medium, the wave travels faster compared to a rigid rock body since the rock is less compressible. This difference in wave velocity arises from the effect of porosity on the overall stiffness and compressibility of the rock, affecting the speed of seismic waves propagating through it.

The most pronounced impact empirically demonstrated, is observed at porosities below 10%, where both P-wave and S-wave velocities exhibit an exponential increase. However, as porosity exceeds 10%, the increase in Vp and Vs becomes more gradual and follows a linear trend. The R^2-values (coefficient of determination) reflect the sum of the distance the data deviates from the best-fit line.

In Figure 4.10, it is evident from both plot A and B that Murchison and Golden meteorites slightly deviate from the trend line. Murchison lies above the trend line, while Golden sits just below it. This divergence is intriguing since both meteorite groups have similar porosity. The disparity could be attributed to differences in mineralogy that also play a role in determining the seismic velocities.

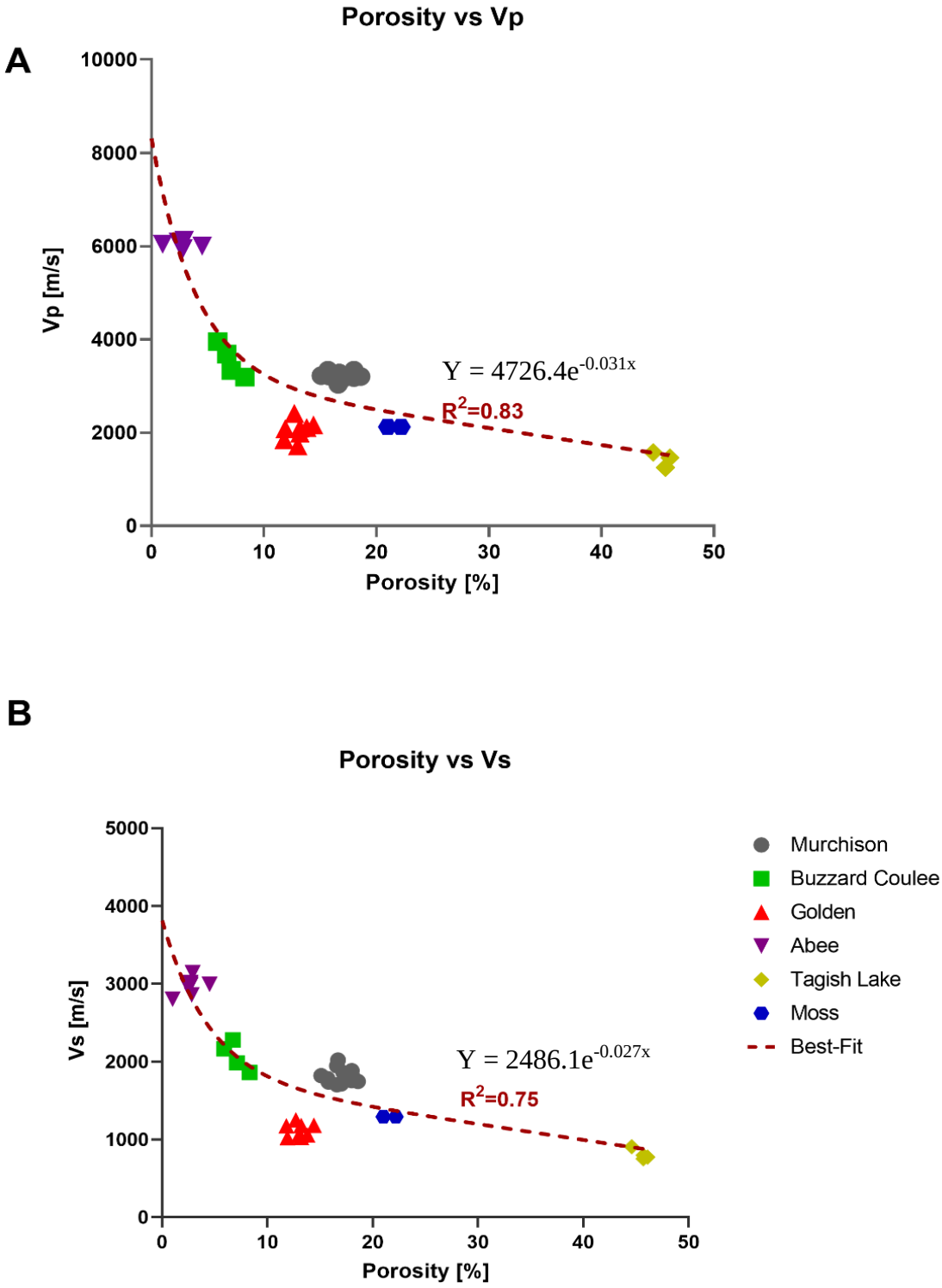

Figure 4.10: A) plot of the exponential correlations observed between Vp and porosity with an R-value of 0.83. B) plot of the exponential correlation observed between Vs and porosity with an R-value of 0.75.

4.4.3 The Vp/Vs ratio

The Vp/Vs ratio of terrestrial rocks has been frequently discussed [e.g., Lee, 2003]. The velocity ratio has proven to be a versatile metric, serving various purposes, including indicating lithology, assessing the degree of consolidation, identifying pore fluid, and predicting velocities [e.g., Lee, 2003; Hamada and Joseph, 2020]

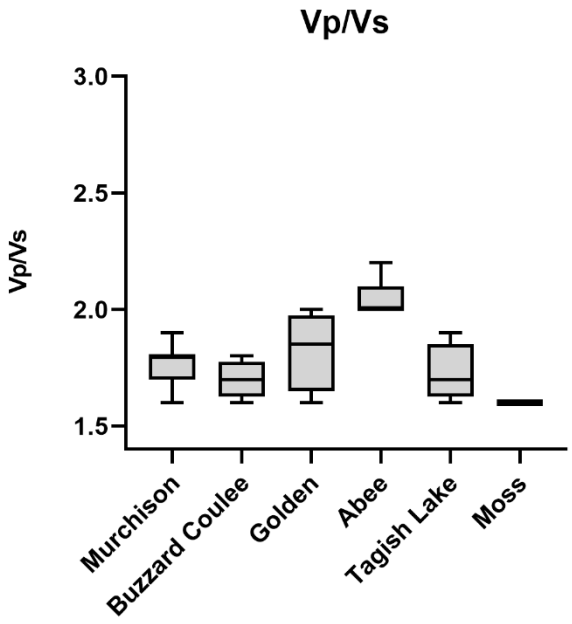

Figure 4.11: the figure illustrates the Vp/Vs ratios measured for each meteorite of this study. The bars show the range.

In this study, the Vp/Vs ratio was measured for our meteorites, revealing significant variations (Figure 4.11). The use of Vp/Vs ratio as a discriminant for lithologies is well-established in terrestrial literature (Limestones having some of the lowest ratio of 1.5 and shales having some of the highest of 2.0 among rocks in dry conditions). Therefore, the observed range of Vp/Vs ratios in meteorites might be indicative of inherent heterogeneities. [e.g., Castagna et al., 1985; Lee 2003]

Particularly noteworthy is the high range of ratios observed in Golden meteorite. The range could be an indication of significant heterogeneities in the rock.

In the terrestrial literature, the Vp/Vs ratio exhibits a correlation with porosity. The nature of this relationship is primarily empirical and subject to variations based on lithology and fluid content within the rocks. As a prevailing trend, there exists an inverse correlation

between the Vp/Vs ratio and porosity. Nevertheless, it is important to note that for high porosity values (> 45 %), the ratio is projected to increase exponentially [e.g., Lee et al., 2003].

There is a weak correlation between porosity and the Vp/Vs ratio (Figure 4.12). As porosity increases up to 15%, the ratio exhibits a declining trend. Once the porosity surpasses this threshold, the ratio stabilizes and remains consistent. Nevertheless, it is worth noting that the data displays significant scattering, necessitating the collection of additional data to gain a more comprehensive understanding and interpretation of the relationship between porosity and the Vp/Vs ratio.

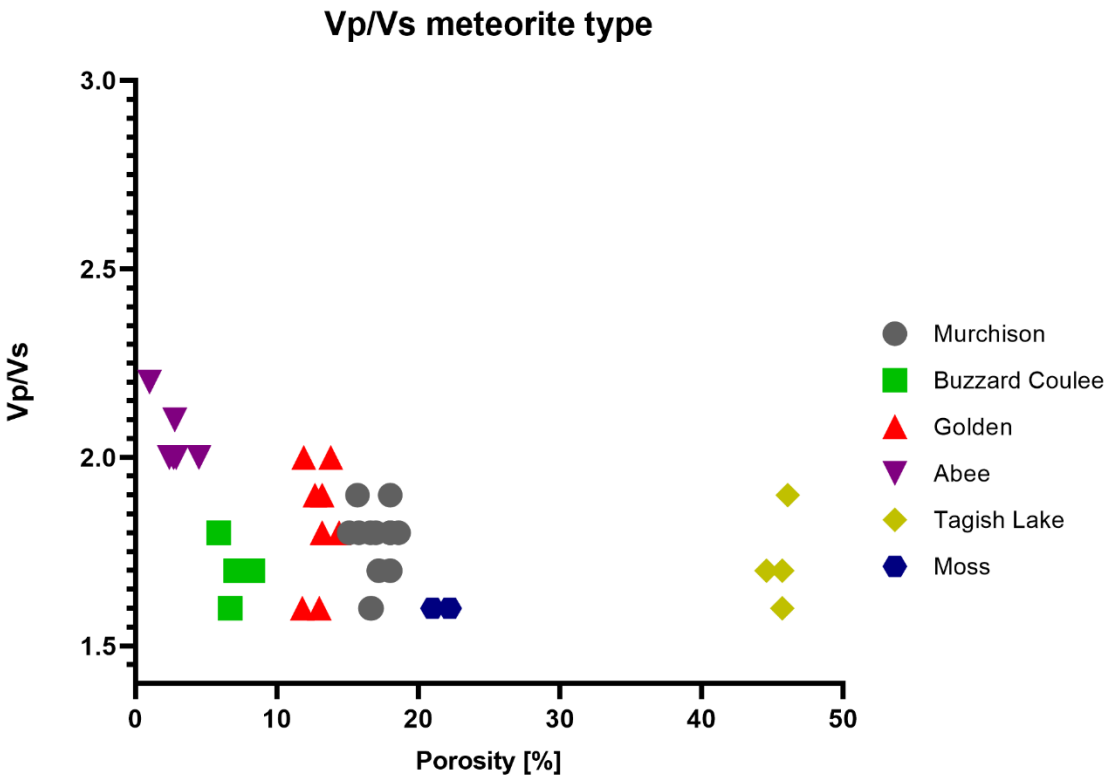

Figure 4.12: The graph depicts the relationship between the Vp/Vs ratio and porosity. Although a potential trend could emerge, the data points exhibit considerable scattering.

Among the recorded Vp/Vs values, the highest is observed in Abee. It is noteworthy that the lowest ratio measured in this study is measured to be 1.6 (measured for all the meteorites, beside Abee) which aligns well with the lowest 1.5 ratio ever documented for sedimentary rocks. [e.g., Castagna et al., 1985; Lee 2003].

4.5 Mechanical and Elastic Properties

Rock strength refers to the ability of a rock material to resist deformation or failure when subjected to external forces. These forces can be compressive, tensile, or shear in nature, and the strength of rock is typically measured in terms of its ability to withstand such forces without fracturing.

The strength of rock is influenced by various factors, including its mineral composition, grain size, texture, porosity, and the presence of fractures or other structural weaknesses. Additionally, environmental factors like temperature, pressure, and water saturation can also impact the strength of rocks. In this section we discuss strength of meteorites and the relations with other properties measured in this study.

The elastic properties of rocks also play a crucial role in determining their response to stress and deformation. These properties, alongside mechanical characteristics, collectively define the deformation behavior of rocks. Understanding these fundamental attributes is essential for comprehending how meteorites behave under external forces also at the parent body scale.

4.5.1 Hardness/Coefficient of Restitution and correlations

In previous studies, the Leeb hardness and coefficient of restitution for meteorites have not been measured. Nevertheless, as discussed in the results chapter, these tests are

nondestructive and have shown correlations with strength in the terrestrial rock literature. This suggests that hardness could be a valuable non-destructive technique with the potential to predict the strength of meteorites.

Throughout this research, we conducted measurements of the Leeb Hardness and the coefficient of restitution on different meteorite samples. However, we refrained from performing these measurements on the cuboids and cubes due to their small sizes. The reason behind this decision is the potential for interference from boundary effects and reflected seismic waves when dealing with samples that are too small.

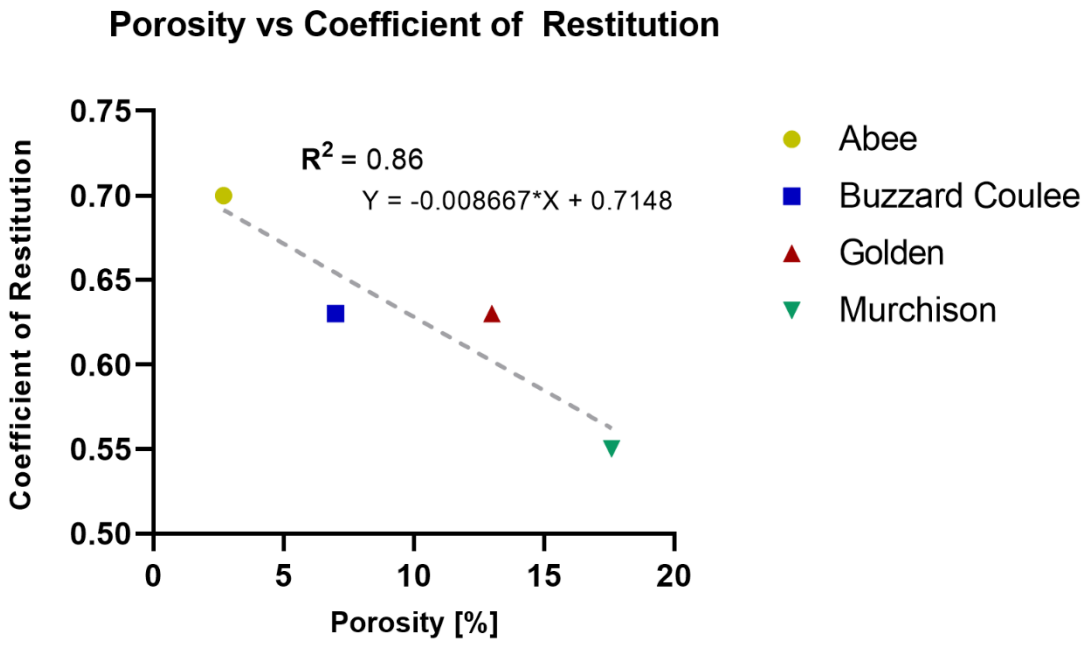

Figure 4.13: the plot shows the correlation between the coefficient of restitution and porosity, indicated by an R-value of 0.86.

Figure 4.13 illustrates the inverse relationship between porosity and the coefficient of restitution. The data used to establish this correlation represents average values for both porosity and the coefficient of restitution.

Notably, the coefficient of restitution increases as porosity decreases. Despite having a limited dataset of only four data points, we have a good level of confidence in this correlation, as similar trends have been previously observed in the literature concerning terrestrial rocks. [e.g., Yasar and Erdogan, 2004]

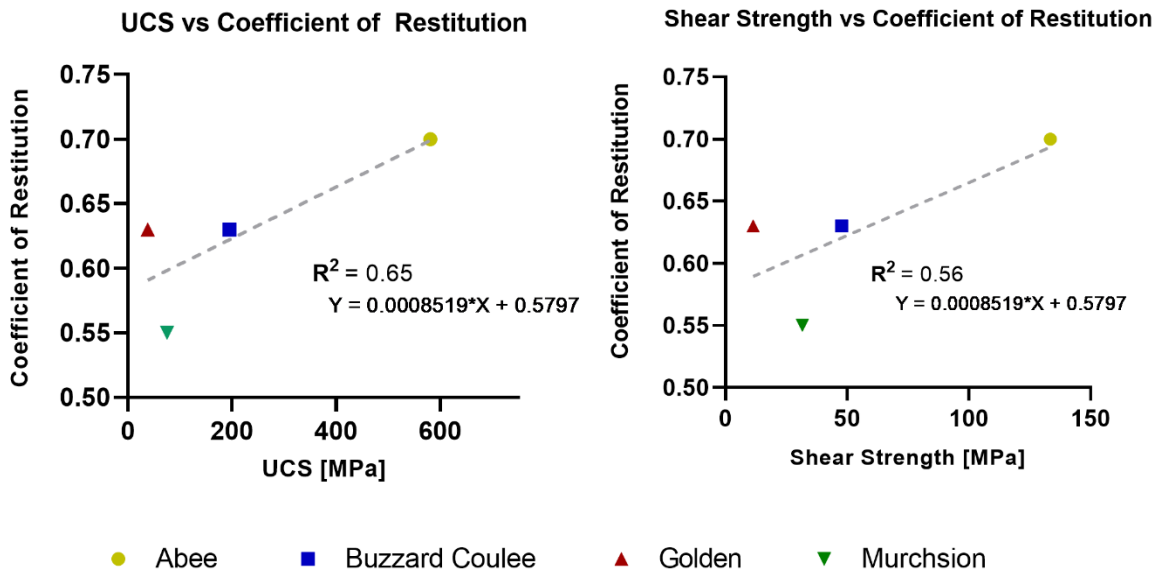

Figure 4.14: The diagrams display the potential correlations between UCS and the coefficient of restitution (left), as well as between shear strength and the coefficient of restitution (right).

Figure 4.14 presents a potential correlation between the Unconfined Compressive Strength (UCS) and the coefficient of restitution. This relationship has been previously documented in the context of terrestrial rocks [e.g., Corkum et al., 2018; Ghanizadeh et al., 2017, Ghorbani et al., 2022]. However, it's important to note that further data are required to thoroughly assess this correlation for meteorites as the latter include a spectrum of diverse mineralogies.

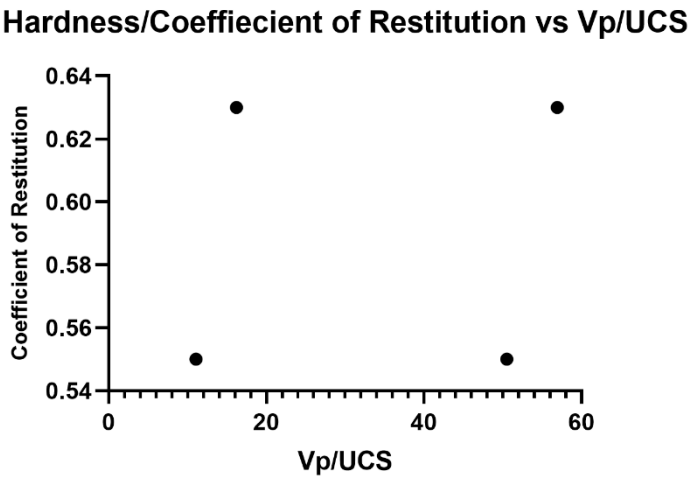

Figure 4.15: no correlation is observed between the coefficient of restitution and the Vp/UCS ratio.

Figure 4.14 also reveals a less pronounced (R-value = 0.56) correlation between the coefficient of restitution and shear strength.

When looking at the elastic properties in the context of the hardness/coefficient of restitution, our data disagree with previous literature. As previously mentioned in the results chapter, Karaman and Kesimal (2015) reported a robust correlation between hardness, P-wave velocities, and the P-wave/UCS ratio for terrestrial

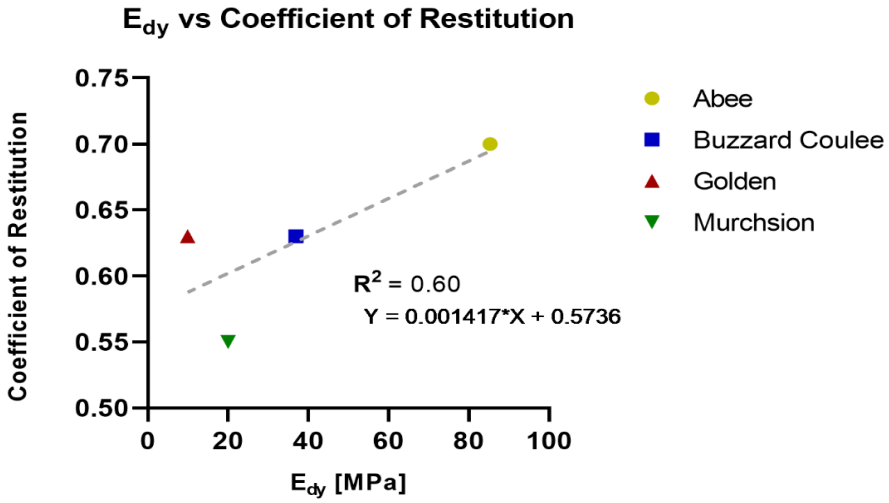

Figure 4.16: the plots show the correlation between the coefficient of restitution and the dynamic Young's Modulus (E_{dy}).

rocks. In contrast, our data does not exhibit such correlations (Figure 4.15). This discrepancy might be attributed to the limited size of our dataset or differences in rock type.

Further investigations with a larger and more comprehensive dataset may be necessary to explore and validate these relationships in greater detail. Nonetheless, we have identified a potential correlation between the coefficient of restitution and the Dynamic Young's Modulus (Figure 4.16).

4.5.2 Unconfined Compressive Strength (UCS)

The unconfined compressive strength (UCS) is a critical mechanical property used to assess the strength and load-bearing capacity of materials under compression.

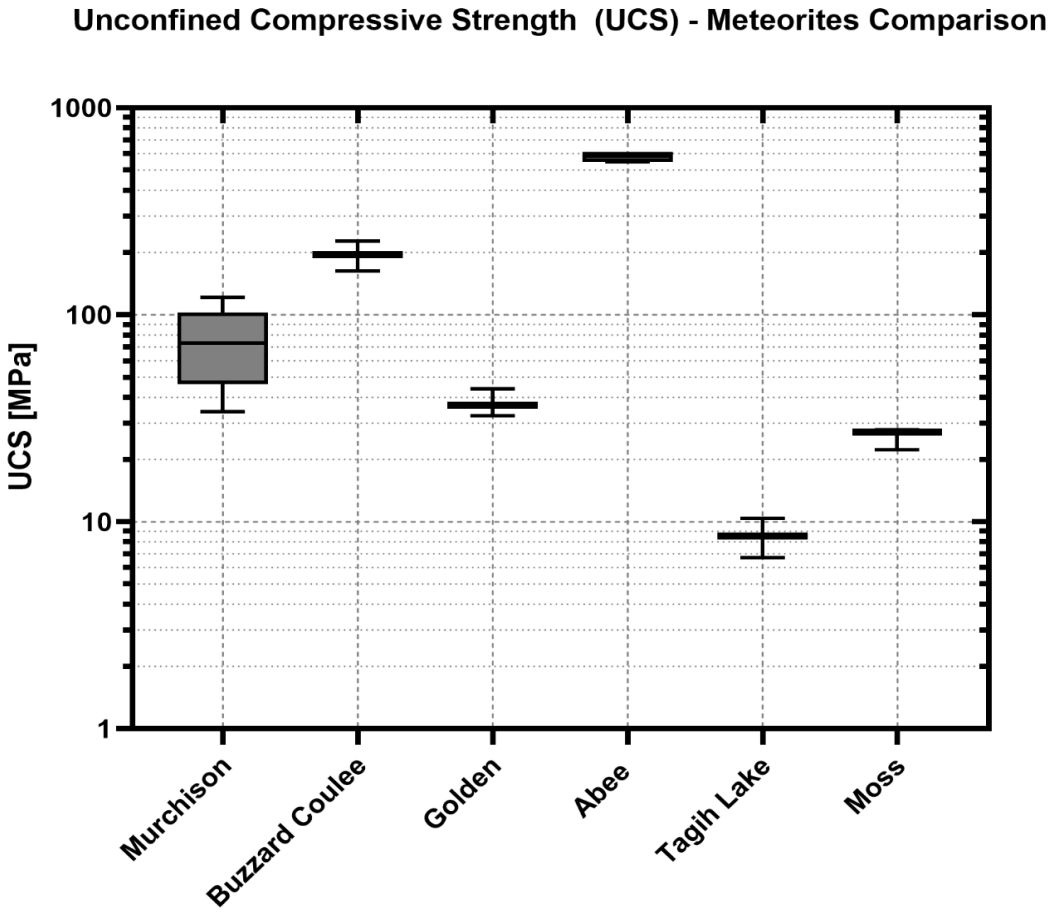

Figure 4.17: Box and whisker plot illustrating the UCS measurements for each meteorite included in this study. Please note that the y-axis is in logarithmic scale.

UCS is a measure of a material's ability to resist axial compressive forces without lateral confinement. To the present, only 13 different falls have been measured for UCS, 10 of them are L, LL and H chondrites.

4.5.3 Samples comparison

Abee (EH)

Abee (EH) is the strongest meteorite among the samples of this study with a mean recorded UCS of 580.6 MPa and a range of 545.9-610.6 MPa (Figure 4.17). There is a clear distinction between clasts and matrix with matrix being the strongest component recording a mean UCS of 610.05 and the clasts recording a mean UCS of 551.15 MPa.

Prior to this study, no EH chondrites had undergone UCS measurements. The UCS of Abee, which falls near the upper limit reported for iron meteorites at 700 MPa [Pohl and Britt, 2020], establishes it as one of the strongest meteorites ever collected.

It's important to note that the UCS measurement of 700 MPa was obtained from a sample of the Hoba meteorite, which is considered the largest single meteorite ever discovered on Earth. The Hoba meteorite is estimated to have fallen on Earth over 80,000 years ago, and as a result, its mechanical properties may not accurately represent those of the original meteoroid. Hoba, in fact, has undergone electrochemical corrosion due to the high humidity occurred during the moist climates that prevailed in Africa in the last 80,000 years ago (where the meteorite is located) [e.g., Golden et al., 1992].

The UCS measurement of Abee sample located at the border between a large clast and the matrix, yielded a value of 554 MPa, that is between the UCS compressive strength values of the clasts and the matrix. Considering that Abee recorded one of the highest mean UCS

values among meteorites and terrestrial rocks, this suggests that brecciation does not necessarily reduce the UCS significantly although may create some/minor internal variability.

Buzzard Coulee (H4)

The mean UCS of Buzzard Coulee (H4), which is 195 MPa, surpasses the reported mean value of 149 MPa for H chondrites by Pohl and Britt (2020). However, it is worth noting that the range and mean reported by Pohl and Britt (2020) included both "finds" and "falls". When we consider only the falls, only 2 H chondrites have been measured for UCS, Tamdakht (range 25.9-247.4 MPa) and one sample of Pultusk (213 MPa). In the case of Tamdakht, of the 13 samples measured, the lowest strength recorded of 25.9 MPa is an outlier considering that the other 12 samples recorded a UCS above 80 MPa.

Considering the mean value of the H falls an excluding the lowest 25.9 MPa strength, the H falls recorded a mean UCS of 138.6, placing Buzzard Coulee significantly above.

The UCS range for Buzzard Coulee is 162-227.5 MPa (Figure 4.17), indicating a notably wide variation as recorded for Tamdakht. This variation does not appear to be connected to differences in sample sizes. Although the porosity and grain/bulk densities of Buzzard Coulee, as detailed in previous sections, exhibit uniformity. The elastic (seismic velocities) and mechanical properties show heterogeneity. Buzzard Coulee is a cryptic breccia so it may reflect matrix/clast contrast. It is reasonable to speculate that these differences in seismic velocities and strength may be attributed to rock structural differences rather than mineralogical distinctions, such as variations in pore shape and distribution, as well as preferential pore or mineral orientations.

Golden (L/LL)

Golden (L/LL) meteorite exhibited a mean UCS of 37.7 MPa, with a range of 32.5-43.9 MPa (Figure 4.17). Notably, this mean UCS value significantly differs from the reported mean UCS values for L and LL chondrites, which are 289 MPa and 86 MPa, respectively [Pohl and Britt, 2020]. However, it is important to mention that the range provided by Pohl and Britt, 2020 for the L and LL chondrites does not differentiate between "find" and "falls". When considering only the falls, only 2 LL meteorites have been measured for UCS, Chelyabinsk and Krymka with a range of 45-160 MPa and a mean of 85.5 MPa. In the case of the L's, 6 falls have been tested for UCS reporting a range 20-265 MPa and a mean value of 100 MPa.

Considering Golden strength, the L/LL chondrites might be the weakest ordinary chondrite lithology.

Golden's mean value of UCS is significantly different than that of the other only L/LL measured previously in literature of 6.61 MPa [Buddhue, 1942]. This value was recorded for the Holbrook meteorite that fell in 1912. Some of the meteorites were collected decades after the fall and they recorded substantial terrestrial weathering. It is not specified what sample and size have been used to measure the UCS by Buddhue (1942) so the value of comparison is uncertain.

Moss (CO)

Moss (CO3) recorded a mean UCS of 25.8 MPa and a range of 22.3-27.8 MPa (Figure 4.17). Prior to this study no CO chondrites have ever been measured for UCS. The only reported value for CO chondrites is 31 MPa for tensile strength for the Kainsaz meteorite

[Svetsov et al. 1995]. This is significantly too high based upon our measurements of UCS: this likely reflects that the tensile strength for Kainsaz was derived from a theoretical model of atmospheric entry.

Murchison (CM)

Murchison displayed a mean UCS of 74.7 MPa, showcasing a remarkable range of 34-121 MPa (Figure 4.17). In earlier literature, two samples of Murchison were subjected to UCS measurements, resulting in a mean value of 50 MPa [Miura et al., 2008], which falls within the range obtained in this study. The sample sizes used by Miura et al., (5x5x10 mm) were also similar to those employed in this study allowing for a more valid comparison. However, it is worth noting that Miura et al., 2008, claimed "highly reproducible results" for Murchison “despite its heterogeneous, fragile, and high-porosity characteristics”, which contradicts our data.

Murchison exhibits considerable heterogeneity across various properties such as porosity, grain, and bulk densities, and UCS values. The perceived high reproducibility reported by Miura et al., 2008, may be coincidental, considering the complexities of Murchison's composition and structure. Murchison is a breccia and Miura et al., 2008, may have sampled a particularly uniform breccia clast/meteorite.

Another potential reason for the significant variation in UCS measurements could be related to the sizes of the grains in relation to the cuboid sizes. Established principles dictate that for UCS measurements to be representative, the sample size should be at least 10 times larger than the grain size. Murchison comprises grains and chondrules in the millimeter size range, and some samples may have had grain sizes that were too large for the sample

size used in this study, contributing to the observed discrepancies, although the inclusions are typically weaker than the matrix, so it remains somewhat puzzling why this study found a mean UCS ~50% greater than Miura et al. (2008).

When comparing the Murchison UCS range with the C-chondrites [Pohl and Britt, 2020] measured previously in literature, Murchison stands out as the strongest carbonaceous chondrite measured to date; however, strength data of carbonaceous chondrites are very limited (only 3 C-chondrites have been tested for UCS).

Tagish Lake (C2-Ungrouped)

The mean UCS of Tagish Lake is 8.5 MPa, with a range of 6.7-10.4 MPa (Figure 4.17). It is important to consider that this range is derived from only two samples. Among them, the weakest sample of 6.7 MPa exhibited substantial fracturing even before the test. Many of these fractures were oriented parallel to the direction of compression, leading to a lower UCS value.

Given these observations, the UCS value of 10.4 MPa is a more accurate representation of Tagish Lake's strength than the mean value. These variations in UCS values, influenced by the presence of fracturing, offer valuable insights into the impact of such fractures on the strength of meteorites and their parent bodies.

Despite the extreme high porosity (> 45%) and the fragile nature of Tagish Lake samples during handling, they exhibited a surprising UCS although their strength is 3 times lower than the weakest Murchison (approximately 30 MPa) sample and just 2 times lower then Moss (approximately 22 MPa) which have much lower porosities and much more competent general aspect.

When examining previous literature, Tagish Lake stands as the second weakest meteorite in terms of UCS ever recorded, as reported by Pohl and Britt in 2020, with only the Holbrook meteorite (~ 6.7 MPa) displaying lower strength. However, it is essential to consider the context, as discussed earlier for Golden. The measurements of the Holbrook meteorite conducted in 1942 by Buddhue lack sufficient contextual information, which decreases the level of confidence in the comparison.

Before this study, there were no UCS values reported for the Tagish Lake meteorite. However, Tsuchiyama et al. in 2008 conducted measurements of the tensile strength of Tagish Lake grains (100 microns in size), revealing two distinct mean values. The carbonate-poor lithology exhibited a mean tensile strength of 0.8 MPa, while the carbonate-rich lithology displayed a higher mean tensile strength of 6.7 MPa. Considering that the 10.4 MPa UCS reported in this study is measured for the carbonate-rich lithology, the mean 6.7 MPa of Tensile measured by Tsuchiyama et al., 2008, is not compatible with our findings; tensile strength is normally 10/15 times smaller than the UCS as evidenced in terrestrial rocks literature when excluding foliated rocks [e.g., Perras and Diedrichs, 2014]. They may have measured a nonrepresentative clast that was primarily composed of a carbonate crystal. Based on the relation observed for terrestrial rocks, Tagish Lake will likely have a tensile strength of ~ 1 MPa.

In their study, Tsuchiyama et al. in 2008 utilized micro compression technique, which significantly differs from our method, especially concerning the sample scale. To adequately discuss and compare the micro compression data of meteorites, as well as the more conventional "traditional" methods at the centimeter scale, additional data are required. Micro and nano techniques will always have sample size complexities in

upscaling to the sample sizes of traditional measuring techniques. Meteorites are particularly challenging compared to most terrestrial rocks because of very divers mineralogy. Obtaining a broader range of measurements will facilitate a comprehensive understanding of the mechanical properties of meteorites and allow for meaningful comparisons between different studies and techniques.

4.5.4 UCS and correlations

A significant correlation exists between UCS and porosity, as illustrated in Figure 4.18. This correlation has previously been noted for terrestrial rocks, and it exhibits distinct characteristics across various lithologies.

For meteorites as porosity decreases to below 10%, the UCS shows a rapid exponential increase, but as porosity approaches 30%, the UCS growth levels off, nearly reaching a plateau. Given the significant correlation observed between UCS and porosity and taking into account that Tagish Lake has a porosity approaching the maximum possible for rocks, it can be inferred that Tagish Lake may represent the lowest achievable UCS for intact extraterrestrial rocky materials (excluding regoliths).

A robust correlation exists between the uniaxial compressive strength (UCS) and both compressional wave velocity (Vp) and shear wave velocity (Vs) (see Figure 4.19 A and B). Notably, the correlations are strongest when considering Vp and Vs measured for the direction parallel with the direction of compression. However, it weakens when considering measurements in the two orthogonal directions. Figure 4.19 highlights the correlation between Vp and Vs values when measured in the same direction as the compression axis. The observed correlation instills greater confidence in the findings.

Additionally, both Vp and Vs exhibit exponential correlations, wherein seismic velocities experience exponential growth with increasing UCS.

The correlations between Vp, Vs and UCS have been observed already for terrestrial rocks [e.g., Liu et al., 2022]. In general, the characteristics of the correlation (e.g., type, slope, R-value) change with changing rock type [e.g., Misha and Basu, 2013; Liu et al., 2022].

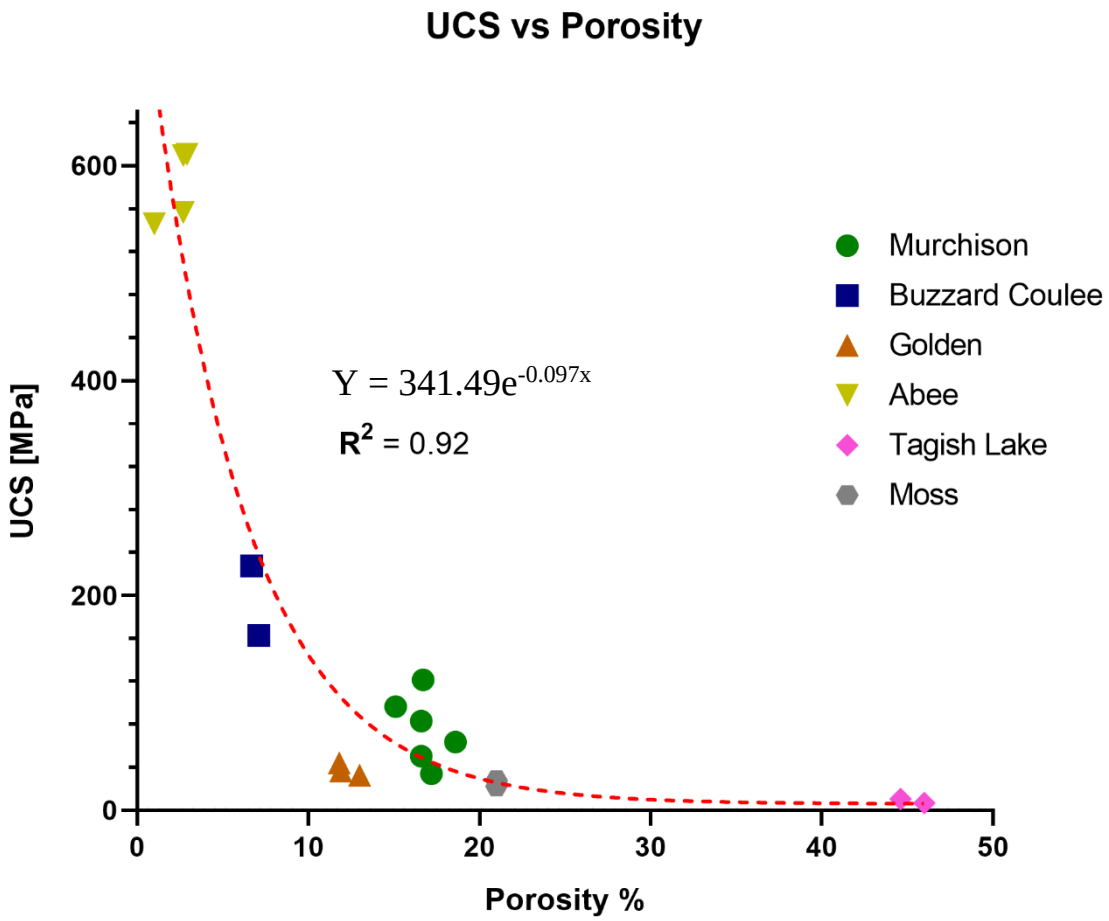

Figure 4.18: The graph illustrates the robust correlation (R^2 of 0.92) discovered between UCS and porosity.

Misha and Basu, 2013 conducted a study on granites, sandstones, and shists, revealing a linear correlation between Vp and UCS for Granite and Sandstone, while schists exhibited a non-linear correlation. Conversely, Liu et al., 2022 discovered a second-order polynomial

correlation between UCS and Vp for sandstones and an exponential correlation for mudstones.

In this study we observe an exponential correlation between both Vp and Vs and the UCS for all the meteorites. Interestingly, this finding aligns more closely with the correlation observed for mudstone by Liu et al., 2022.

To summarize, our analysis indicates that porosity, Vp, and Vs are the major predictive variables for the uniaxial compressive strength (UCS) of meteorites. These findings are consistent with the existing terrestrial rock literature. No evident correlations with other properties like grain density have been observed in this study.

Given the broad spectrum of observed UCS (a factor of ~50) and porosity values in meteorites, and the observed plateau of UCS for porosities exceeding 30%, it appears that the atmospheric entry does not entirely favor stronger lithologies over weaker ones. Consequently, the perception that meteorites represent the strongest parts of a meteoroid, likely to survive entry into the atmosphere, may not hold true if the strength variations are modest. If there were indeed a preference for stronger lithologies during the selection process, one would not anticipate encountering the entire spectrum of elastic, mechanical, and physical properties found in meteorite collections. However, for terrestrial entry velocities, there is likely be a distinct cutoff point beyond which meteorites with certain properties, like UCS and porosity, may no longer survive entry.

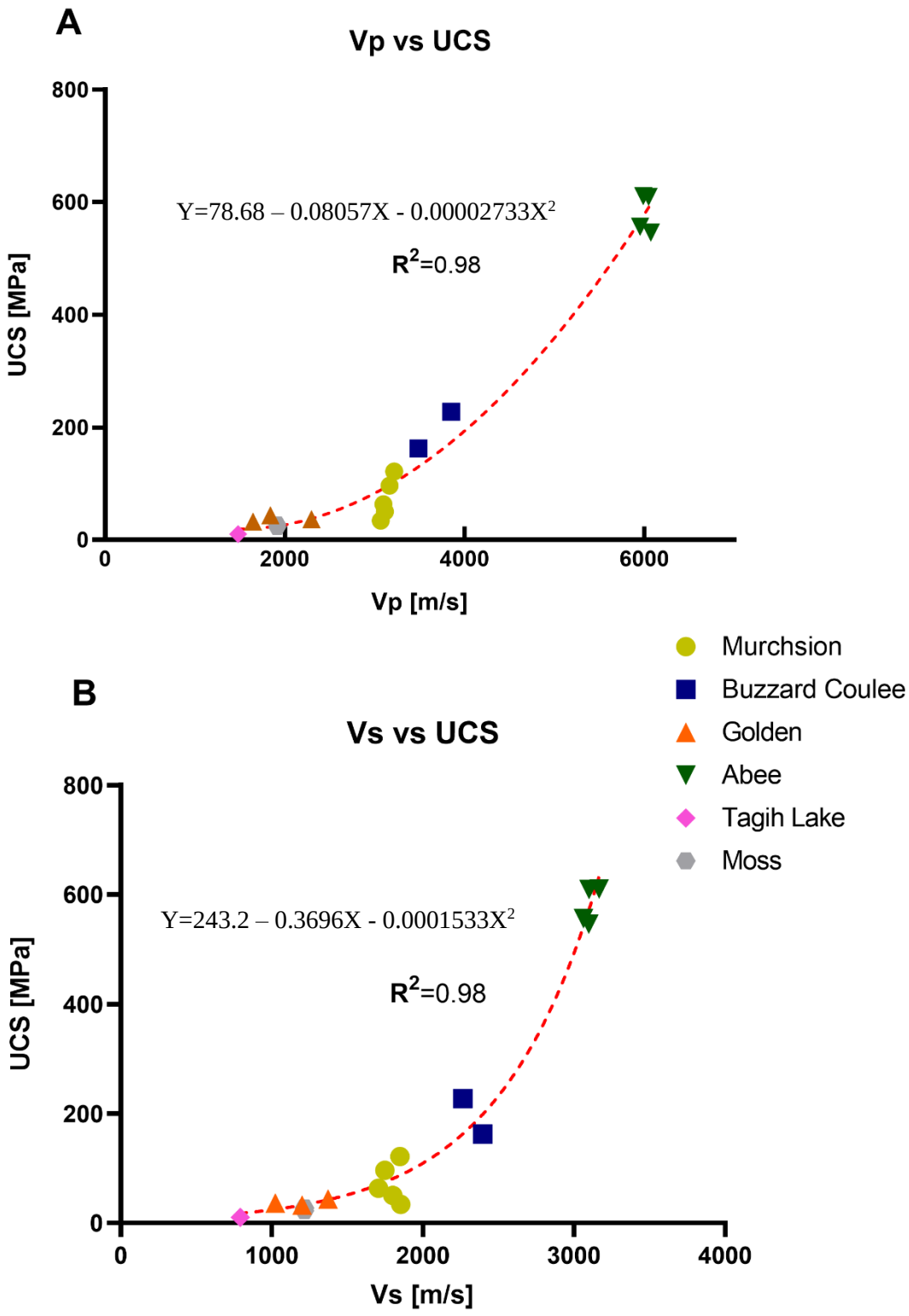

Figure 4.19: A) correlation between UCS and Vp. B) correlation between Vs and UCS.

4.5.5 Direct Shear Strength (DSS) – Samples Comparison

This study presents the first shear strength data ever reported for meteorites (Figure 4.20). As discussed in the Methods chapter, the community defines the shear strength measured in this study as Direct Shear Strength (DSS).

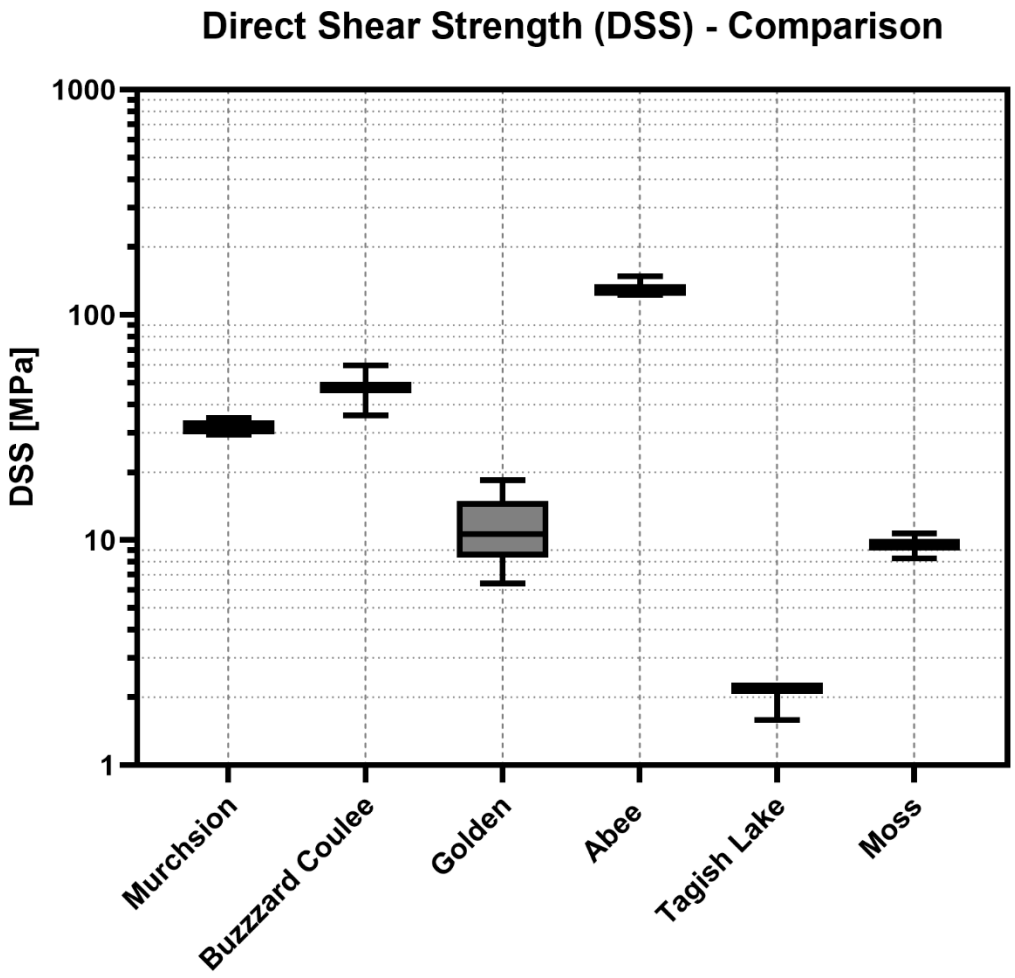

Figure 4.20: Box and whisker plot illustrating DSS for each meteorite included in this study. Please observe that the y-axis employs a logarithmic scale.

While the UCS values of Murchison (CM) meteorite exhibit the widest range among all the meteorites examined in this study, the Direct Shear Strength (DSS) of Murchison, on the other hand, appears to be one of the most uniform (Figure 4.20). The significance of

these differences remains unclear and but is speculated to reflect a greater sensitivity to the presence and orientation of inclusions in the UCS experiments (The direct shear apparatus tests the yield strength of a specific narrow planar volume in the tested cube while the first failure plane formed under compression may occur in any orientation and location in the test cuboid volume.).

Among the meteorites studied, Golden (L/LL) and Buzzard Coulee (H) exhibit the most significant variations, with Golden being the weakest in terms of shear strength. This outcome further confirms that L/LL is the weakest lithology (or that Golden is a particularly weak example of this petrologic type) among the ordinary chondrites, consistent with the findings for UCS discussed in the corresponding section of this thesis.

Additionally, Moss (CO) DSS compares favorably with that of Golden (L/LL) and emerges as one of the weakest meteorites among those examined for DSS. This observation aligns with the fact that Moss ranks as the second weakest measured meteorite in terms of UCS.

As anticipated from the UCS results, Abee (EH) and Tagish Lake (C2-Ungrouped) represent the strongest and weakest samples, respectively.

4.5.6 Brief consideration of sample size vs grain size

The DSS data presented in Figure 4.21 for Murchison solely pertain to the 5x5 mm cubes. As a test for sample size limits Murchison cubes were prepared in 2.5x2.5 mm and 5x5 mm cubes. The size of Murchison (generally weak) inclusions (which are randomly distributed in a finer-grained matrix), typically ~0.5 mm diameter but which can exceed 2 mm at times, was found to be too large for the 2.5x2.5 mm sample cubes. Traditionally quasi-static strength measurements require the grain size to be at least ~10 times smaller

than the size of the sample components (e.g., mineral grains, breccia clasts) being tested to ensure a representative sample (note that this general guideline also assumes isotropic distribution and orientation of discrete components within the sample). Hence, the 2.5x2.5 mm cubes do not accurately represent the true behavior of the material.

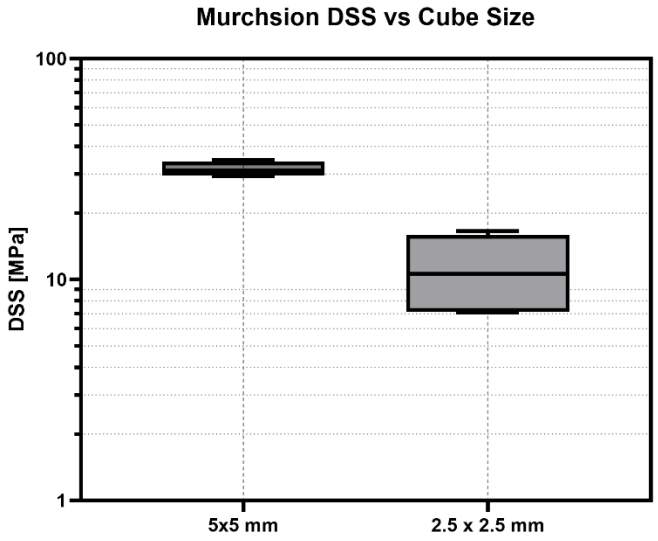

Figure 4.21: Box and whisker plot illustrating DSS measured for the two cube sizes of Murchison. Please observe that the y-axis shows a logarithmic scale.

The Direct Shear Strengths (DSSs) measured for the 2.5x2.5 mm cubes are noticeably different from those measured for the 5x5 mm cubes, not only with a smaller mean value but also with a larger range (Figure 4.21). The variability observed between the cube sizes should not be attributed to scale heterogeneities but rather to the violation of the principle concerning the relationship between component size and sample size. As a caution, the literature has previously discussed the correlation between sample sizes and strength, aiming to predict strength up to the scale of asteroids.

For instance, Cotto-Figueroa et al., 2016 conducted research on scale-dependent relations by measuring the uniaxial compressive strength (UCS) of cubes from Allende (CV) and Tamdakht (H5) at different sizes. However, their study deviated from standard testing protocols, employing sample dimensions ratios that are uncommon in geotechnical engineering or geology. In most literature, a ratio of >2 to 1 between length and width is commonly used to facilitate data comparison across various datasets.

4.5.7 DSS and correlations

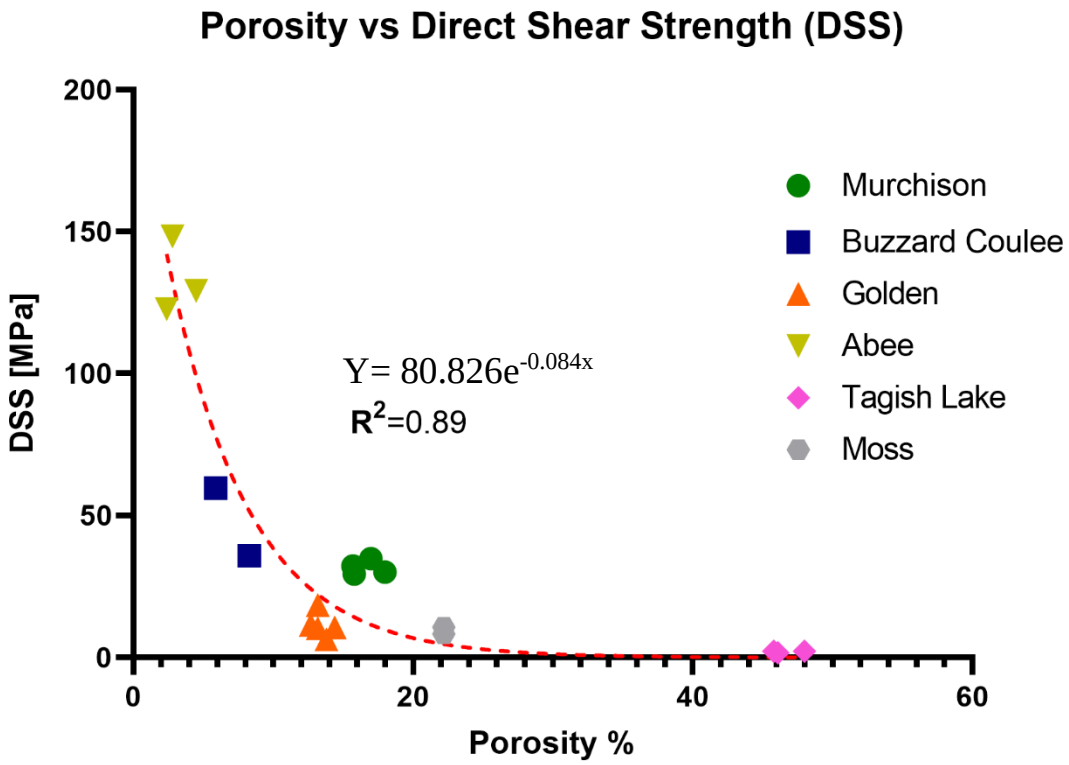

Figure 4.22: The graph depicts a correlation (R^2 = 0.89) between porosity and DSS across all the meteorites measured in this study.

The relationship between DSS and porosity shows a strong correlation (Figure 4.22). The correlation exhibits similarities to the relationship between UCS and porosity. As per the

UCS, the influence of porosity on DSS is most pronounced when porosity is below 10%, whereas the impact becomes less significant for porosity values exceeding 30%.

Interestingly, we observed a remarkably robust correlation between Vp, Vs, and DSS (Figure 4.23). Unlike the UCS, the correlation between Vp, Vs, and DSS is strongest when considering the measurements along the side perpendicular to the applied force, essentially normal to the shear plane; this correlation is as expected since the oscillation direction is perpendicular to the motion direction. This finding suggests that the wave velocities in specific directions hold significant influence over the material's shear strength properties, providing possible insight for further research.

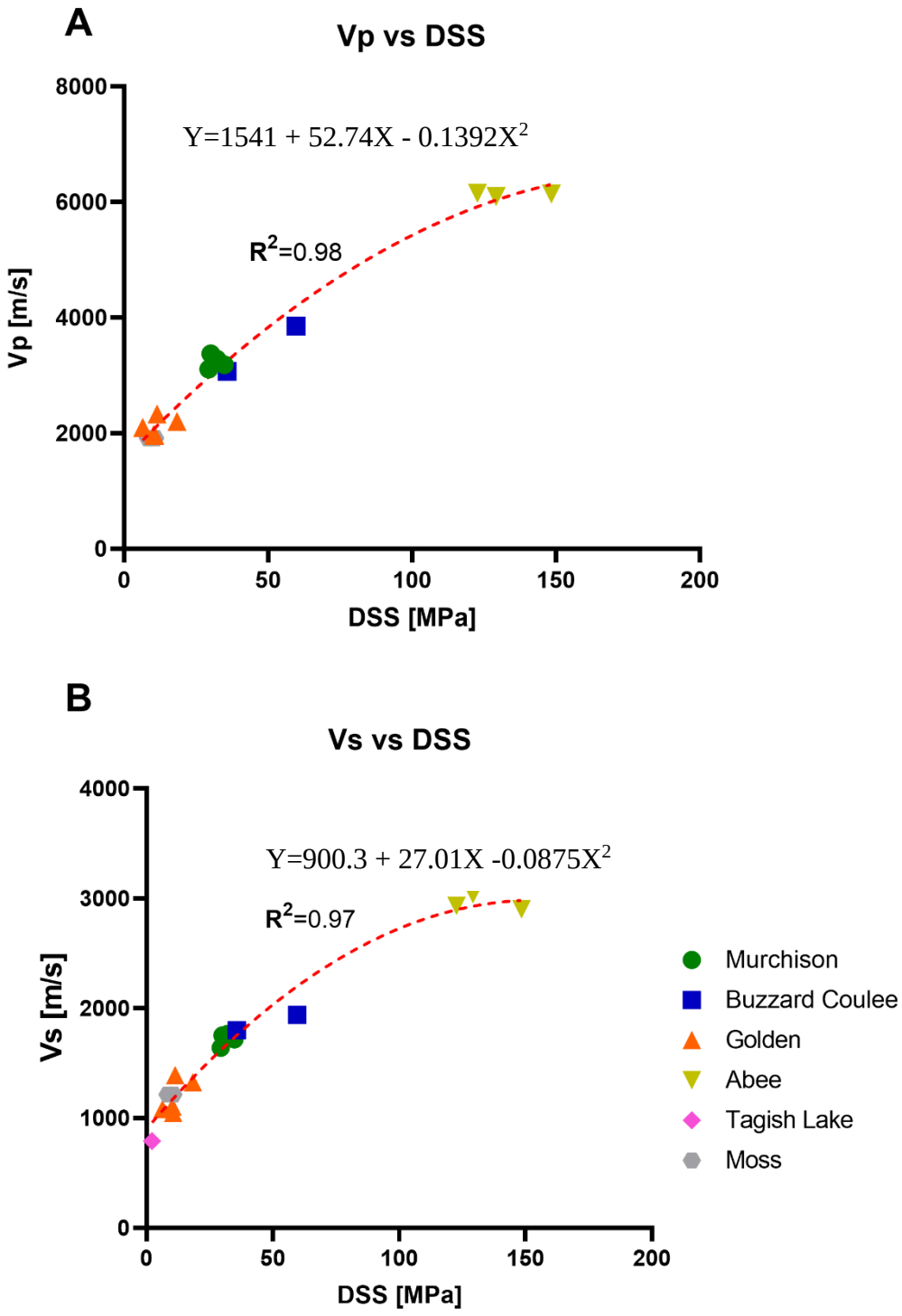

Figure 4.23: A) correlation between Vp and DSS. B) correlation between Vs and DSS

4.5.8 DSS vs UCS

The stress-strain behavior of a material under shear and compressive loading differs. In direct shear testing, the shear stress is directly related to the shear strain, providing valuable information about the material's internal friction angle and cohesion.

In terrestrial rocks literature, many empirical relationships have been proposed between the UCS and DSS, particularly in the context of geotechnical engineering. [e.g., Rashidi et al., 2019]

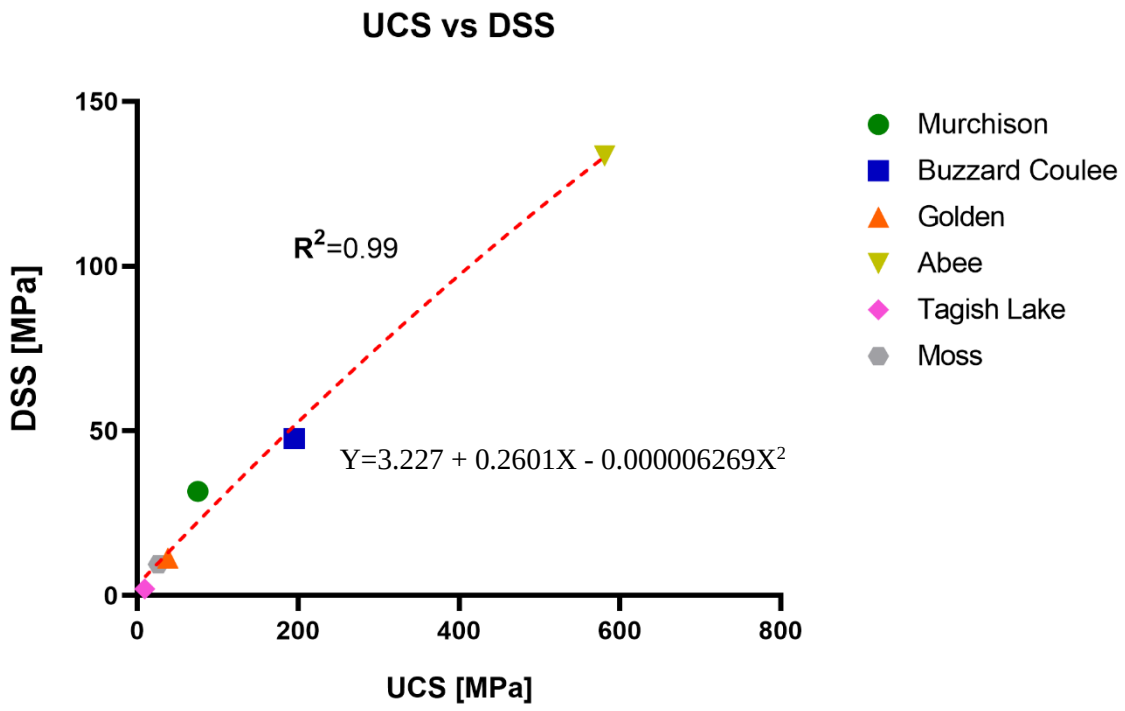

3: The graph illustrates a correlation between DSS and UCS, yielding an R-value of 0.99.

The tested meteorite samples show a robust correlation between the UCS and the DSS, showing an exceptionally high R-value of 0.99. This strong correlation is non-linear (second order polynomial) as depicted in Figure 4.24; DSS increases at a slower pace

relative to UCS. The UCS and DSS values used for this correlation were averaged for each meteorite sample.

The robust correlation established in this study offers a useful means to predict the shear strength of meteorites and asteroids based on their UCS values or vice versa.

It was observed that the UCS/DSS ratio may also exhibit a correlation with the porosity of meteorites. Upon plotting the porosity against the UCS/DSS ratio, a linear correlation emerged, excluding Tagish Lake, which is an outlier in the data set (Figure 4.25).

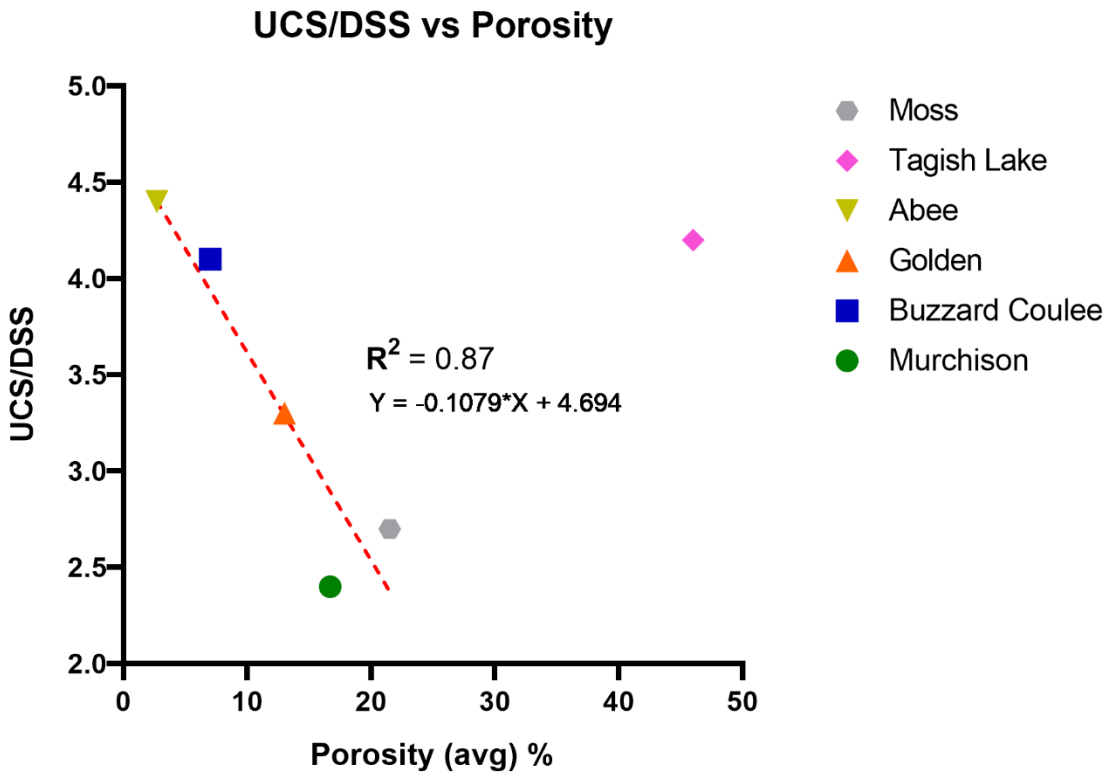

Figure 4.25: correlation analysis of the UCS/DSS ratio with porosity reveals an R-value of 0.87 (when excluding Tagish Lake data).

The presence of Tagish Lake as a distinct outlier may suggests that materials similar to Tagish meteorites might exhibit a significant different mechanical response compared to other meteorites in the study.

More data are needed to better establish the relation between porosity and the UCS/DSS ratio.

4.5.9 Static vs Dynamic Young's Modulus

The Young's Modulus is a parameter that describes the stiffness of a material, however, the reported data of both dynamic and static Young's Modulus are extremely scarce.

The relationship between the dynamic Young's Modulus and the static one remains a subject of ongoing debate. Most of the literature supports the idea that the dynamic Young's Modulus is generally higher than the static counterpart [e.g., Cicotti and Mulagria, 2004; Elkatatny et al., 2018; Martinez-Martinez, 2018, Kotsanis et al., 2021].

In general, rocks tend to exhibit greater strength when subjected to deformation under high strain-rate conditions. This phenomenon occurs due to the limited velocity of fracture propagation. At high loading rates, the weaker flaws in a material do not have sufficient time to cause failure before other, progressively stronger flaws become activated, contributing to the overall enhanced strength observed under such rapid loading conditions [e.g., Kimberley and Ramesh, 2011].

Meteorites present a challenging scenario in understanding their static and dynamic Young's Modulus as limited information is available. Additionally, cross-referencing data from various research papers is complicated because different authors have used distinct

techniques and size dimension ratios that do not conform to established technical standards of measurements, such as ASTM.

For instance, Cotto-Figueroa et al., 2016 conducted a study measuring both the static and dynamic Young's Modulus of two meteorites, Allende (CV) and Tamdakht (H5), marking the only systematic investigation of this kind for meteorites. However, the authors did not specify if they adhered to any recognized standards of measurements, and their use of a sample dimensions ratio that deviates from common standards like ASTMs raises additional concerns. In their study, the static Young's Modulus data were acquired using a camera, but the values obtained from using an extensometer to directly measure the strain (as they mentioned in the text) were not reported. Additionally, although the authors mentioned measuring seismic velocities in all directions, they did not elaborate on or provide the specifics of how these seismic velocities were utilized to calculate the dynamic Young's Modulus (e.g., whether the average or fastest values were used).

The static and dynamic properties play distinct roles in the study of various phenomena, with their applications based on the strain rate. Static properties are utilized to examine the behavior of materials under constant or very slow strain rates, providing insights into their response to steady and gradual loading. On the other hand, dynamic properties come into play when materials experience rapid or fluctuating strain rates, helping us understand their behavior under dynamic and high-speed loading conditions.

For example, the dynamic young’s modulus in planetary science is used to study impact cratering on both the Earth and Asteroids since the stress and the strain associated with the impact occur very rapidly and non in quasi-static conditions [e.g., Asphaug et al., 1996].

Rae et al., 2023 used a model that combine the static and the dynamic Young's Modulus to implement a model of rate-dependent strength, to better study impact scaling relationships.

Figure presents this studies' data of dynamic vs static Young's Modulus; note that due to technical difficulties, Abee and Moss static Young's Modulus was not measured.

The dynamic Young's modulus surpasses the static modulus noticeably, consistent with the conventional understanding of rock mechanics. The dynamic Young's modulus depicted in figure 4.26 was acquired from measurements taken along the parallel direction to the compression axis. This choice was motivated by the strong correlation observed between seismic velocities in the parallel direction and the UCS as discussed in previous sections of this thesis. For our samples the Ed is around two times the Es except for Tagish that is around 4 times. (Figure 4.26, right plot).

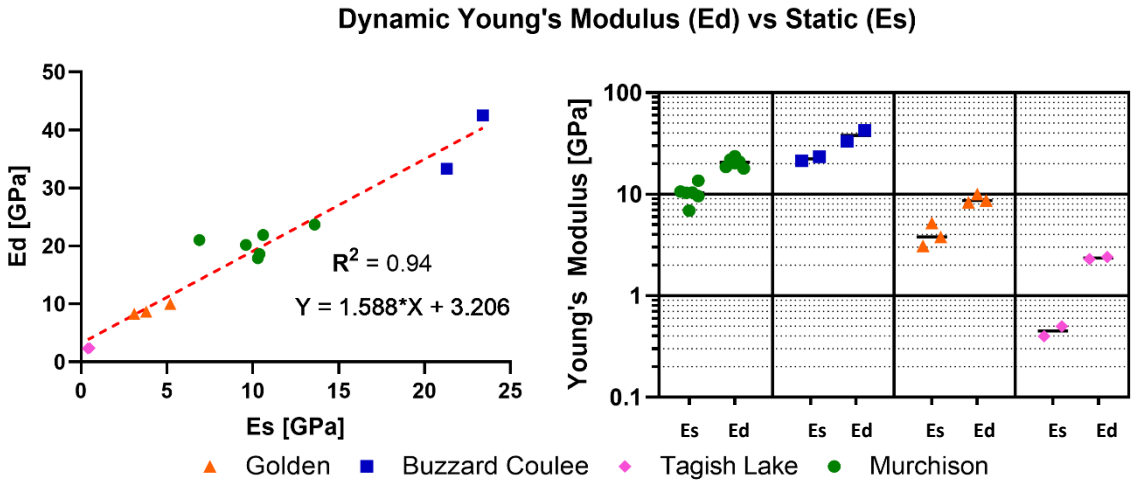

Figure 4.26: The left-hand plot illustrates the correlation between Ed and Es, exhibiting an R-value of 0.94. The right-hand plot showcases all Ed and Es values measured across all the meteorite

A robust correlation between Ed and Es has been noted, potentially enabling the prediction of the static Young's Modulus of meteorites without resorting to destructive testing methods (Figure 4.26, Left Plot).

4.6 The deformational behaviors of meteorites and asteroids

In the field of rheology and structural geology, understanding the failure mechanisms of rock masses or rocks in response to stress necessitates an understanding of their distinctive deformational behaviors. While earlier sections provided quantitative insights into the mechanical and elastic characteristics of meteorites, this section offers a more qualitative overview of their deformational behaviors.

Rocks are commonly categorized into two primary types: brittle and ductile. It's crucial to recognize that while rocks display both brittle and ductile behaviors at room temperatures, everything changes at elevated pressures and temperatures. When increasing temperature and pressure conditions, every rock will start to exhibit more ductility. As pressure and temperature escalate significantly, typically at depths around 12 kilometers for the Earth, fractures cease to form, and the rock undergoes a state of perfect plasticity, deforming consistently under constant stress once the elastic limit is surpassed. [e.g., Fossen, 2016]

Brittle materials are prone to fracture or break without undergoing significant deformation when subjected to stress. Cracks propagate quickly through brittle materials, leading to sudden and often catastrophic failure. A brittle rock will absorb much more energy in the elastic region.

Ductile materials are a subset of plastic materials that can sustain substantial plastic deformation before eventual failure. Ductile materials tend to higher capacity to absorb

energy than the brittle materials and most of the energy is absorbed in the plastic region passed the elastic limit.

Given the extensive spectrum of properties and strengths observed in meteorites, it becomes crucial to also account for these distinct behaviors when simulating geological processes on asteroids. Even in cases where an asteroid comprises inherently weaker lithologies, such as carbonaceous materials, its ability to absorb substantial energy could be amplified if it exhibits ductile characteristics (e.g., in the context of asteroid disruption or impact cratering).

A possible effective method for investigating the distinction between brittle and ductile behavior in meteorites is by examining the ratio between the Uniaxial Compressive Strength (define as ultimate strength) and the Proportional Limit. The Proportional Limit provides an estimate of the rock's elastic limit; thus, the UCS/Proportional Limit ratio serves as an indication of the elastic versus plastic deformation. It is essential to recognize that while the ratio offers a valuable insight into elastic/plastic deformation, it does not solely define the entirety of a rock's deformational behavior.

In general, when the ratio is close to 1, the rocks have primarily deformed within the elastic region, implying a more brittle nature. Conversely, ratios above 1 but below 2 indicate substantial elastic deformation, yet notable plastic deformation is also evident. Ratios surpassing 2 signify that the rocks have undergone more deformation within the plastic region than the elastic region, indicating more substantial ductility.

The ordinary chondrites show clear distinction in the UCS/Proportional Limit ratio respect to the hydrated carbonaceous chondrite, Murchison. While Golden and Buzzard Coulee display similar ratios, approaching 1 (Figure 4.27). Murchison showcases a notably higher ratio, reaching up to 1.8. This heightened ratio underscores Murchison's significantly greater ductility in comparison to the ordinary chondrites, which exhibit a more significant brittle disposition.

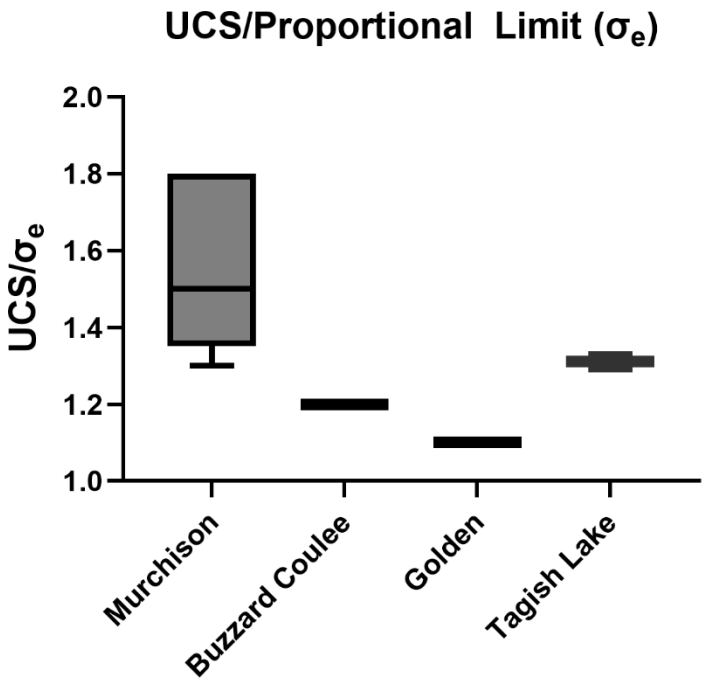

Figure 4.27: Figure 4.27 illustrates the ratios between UCS/Proportional Limit measured for the samples examined in this study.

Another distinctive characteristic of Murchison, setting it apart from the other meteorites under investigation, is its coefficient of restitution. Typically, in brittle rocks, where the majority of deformation transpires within the elastic region, the coefficient of restitution tends to be higher due to minimal energy absorption during sample deformation.

Conversely, manifestations of greater ductility result in lower coefficients of restitution, as a greater amount of energy is absorbed by inducing permanent deformation within the rock.

Despite Tagish Lake exhibiting the highest porosity, its UCS/Proportional Limit ratio of 1.3 is lower than that of Murchison, indicating it to be less ductile than the latter.

Figure 4.28 illustrates the coefficients of restitution measured for the samples analyzed in this study. Notably, Abee exhibited the highest coefficient of restitution, while Murchison displayed the lowest. These findings align with the inference that Murchison possesses a greater degree of ductility. Conversely, Abee, and possibly all the EH chondrites, could be a potential candidate for the most brittle rock within the chondrite lithologies.

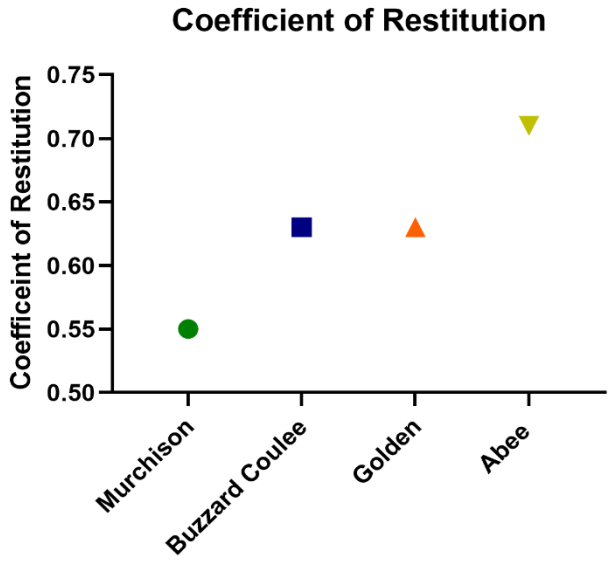

Figure 4.28: the figure displays the coefficient of restitution for the samples measured in this study.

Given the observed UCS/Proportional Limit ratio and coefficient of restitution between, given that Murchison and Abee are representing the two extremes we can then assume that

the same behavior will be maintain at the asteroid scale. In figure 4.29 we qualitatively classified asteroids (composed of chondrite lithologies) based on the deformational behavior.

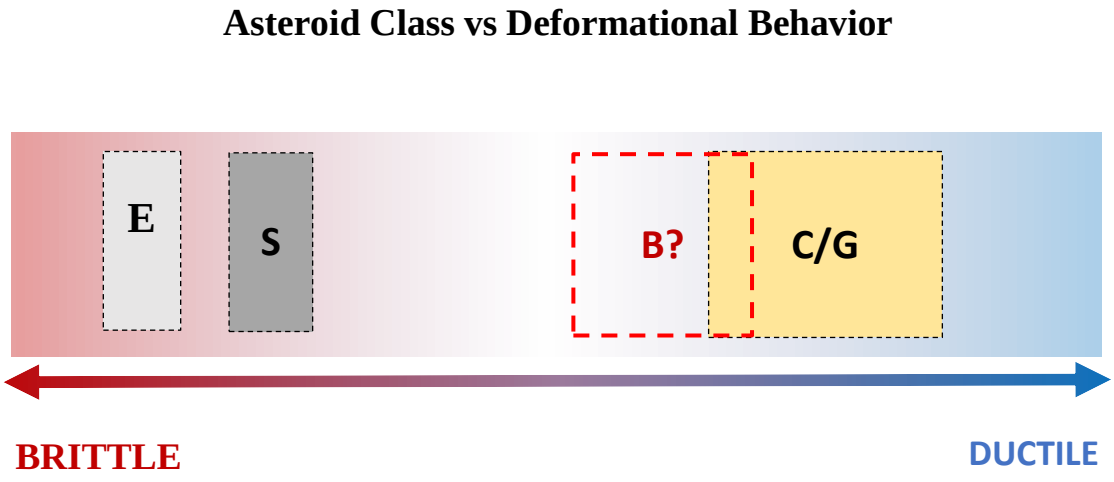

Figure 4.29: The boxes labeled E and S denote E-type (enstatite) and S-type (ordinary chondrite) asteroids, respectively. The yellow C/G box encompasses C-type and G-type carbonaceous asteroids. The broader range observed in the C/G box is attributed to the significant mechanical, physical, and elastic property variability noted in Murchison. The B box signifies B-type asteroids, specifically the exceedingly low albedo carbonaceous category, with Tagish Lake serving as a representative member.

4.7 Future work

Although a variety of rock types have been examined, it would be beneficial to further expand the pool of samples from these (mostly) relatively common meteorite lithologies to assess potential variability within a given clan. Increasing the number of surveyed meteorites to at least three times the current count is likely a practical step to take. The bigger pool of samples will also allow refining prediction curves; machine learning could be also used to better refine some of the curves. Rarer meteorite lithologies could also be explored as available samples allow.

Additionally, I would explore the of grain and chondrule sizes along with their mineralogical compositions. How do the sizes and compositions of these minerals influence the mechanical properties of meteorites?

Utilizing XR-CT could facilitate the assessment of cracks and pore orientations and morphologies. Could the certain pore and crack orientations/morphologies potentially explain the observed seismic velocity disparities among various orientations?

In addition, low pressure gas absorption techniques could also be used to measure pore size distribution that could play a role in the mechanical properties of meteorites.

4.8 Understanding rubble-piles properties from Ryugu sample

The spacecraft Hayabusa2 has recently returned samples from the asteroid Ryugu, ranging in size from 1 to 8 mm (Figure 4.30). This marks the first-ever chance for us to examine the physical, mechanical, and elastic properties on returned asteroid samples. It also offers a valuable opportunity to enhance our comprehension of the internal structure of these rubble pile asteroids.

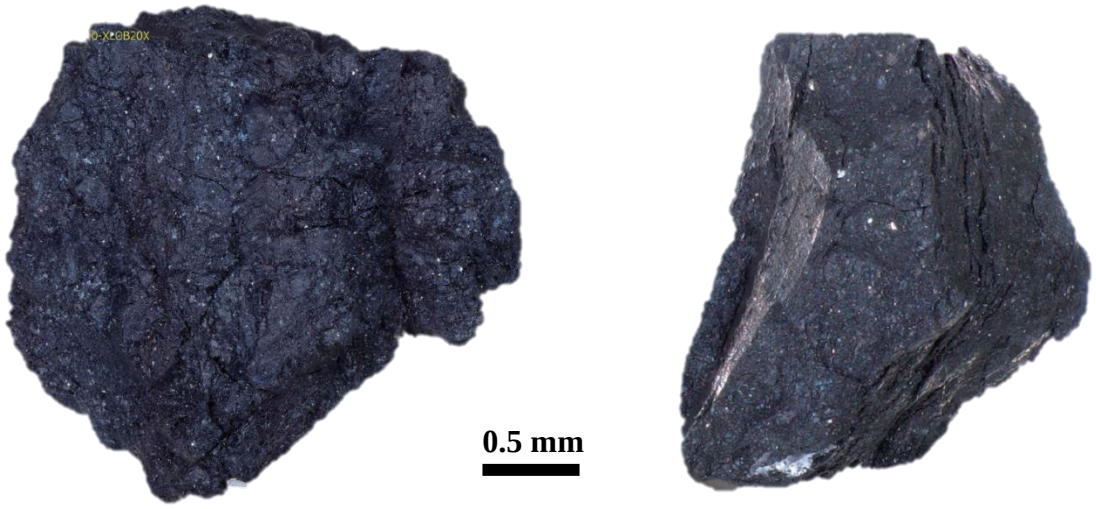

Figure 4.30: this photo shows 2 Ryugu's samples that have been scanned at synchrotron. [photo modified after Nakamura et al., 2022]

As of today, there have been no direct measurements conducted to determine the porosity or grain density of samples from Ryugu. Nevertheless, a significant portion of Ryugu's large clasts have undergone characterization by synchrotron X-ray computed tomography, enabling the calculation of clast volumes. The bulk density measured ranged from 1.7 to 1.9 g/cm^3 with a mean of 1.79 ± 0.08 g/cm^3. [Nakamura et al., 2022]

Considering the mineralogical affinities of Ryugu's samples with those of the CI clan and Tagish Lake, we can safely assume that the grain density of Ryugu's samples will range from 2.50 g/cm^3 (that is the lowest measured for CI, and in agreement with the serpentine and saponite densities of 2.58 and 2.50 respectively) to 2.88 g/cm^3 (less likely) that is the maximum grain density measured for Tagish Lake (the mean Tagish Lake grain density is 2.72 g/cm^3; Hildebrand et al., 2006).

Porosity (ϕ) can be measured as:

$$\phi = 1 - \frac{\rho_b}{\rho_g}$$

were ρ_b is the bulk density and ρ_g is the grain density. Considering the range of bulk densities measured for Ryugu's samples and the upper and lower limit of grain densities measured for the CI and Tagish Lake, Ryugu's average intraclast porosities can range between 25 % (ρ_b = 1.87 g/cm^3 and ρ_g = 2.50 g/cm^3) to 41 % (ρ_b = 1.71 g/cm^3 and ρ_g = 2.88 g/cm^3) (Figure 4.31, gray area)

Furthermore, in a study by Nakamura et al., 2022, Ryugu's grain densities were determined from the modal abundance of phases. This approach yielded a spectrum of grain densities ranging from 2.5 g/cm³ to 2.68 g/cm³, aligning with the grain densities of CI and Tagish Lake samples. By considering both the grain density range established by Nakamura et al., 2022 and the direct assessments of bulk densities, the potential variation in Ryugu's intraclast porosities spans from 25 % (ρ_b = 1.87 g/cm^3 and ρ_g = 2.50 g/cm^3) to 36 % (ρ_b = 1.71 g/cm^3 and ρ_g = 2.68 g/cm^3). Considering the mean bulk density and average grain density (measured by Nakamura et al., 2022), Ryugu mean intraclast porosity is 31%.

These data give us enough constrains to measure the interclast porosity of Ryugu. The asteroid density (ρ_A) is:

$$\rho_A = (1 - \emptyset_{\boldsymbol{inter}}) \times (1 - \emptyset_{\boldsymbol{intra}}) \times \rho_g$$

So the interclast porosity ($\emptyset_{\boldsymbol{inter}}$) is:

$$\emptyset_{\boldsymbol{inter}} = 1 - \frac{\rho_A}{(1 - \emptyset_{\boldsymbol{intra}}) \times \rho_g}$$

The possible range of interclast porosity of asteroid Ryugu is 26% to 41%, considering the asteroid bulk density of 1.19 g/cm^3, a upper and lower limit of 2.69 g/cm^3 and 2.50 g/cm^3 respectively and a range of intraclast porosity from 25% to 36 % (Figure 4.31, blue area).

If we consider the average grain density measure by Nakamura et al., 2022 of 2.59 and the average porosity (from average bulk and grain density) of 31%, the predicted interclast porosity of Ryugu is 33% (Figure 4.31, red diamond).

Considering that Ryugu has shape and composition that are similar to those of Bennu, and that the asteroid density of 1.19 g/cm^3 for both the asteroids, we can expect the same range of Intraclast and interclast porosities for asteroid Bennu. (Figure 4.31, gray area).

Nakamura et al., 2022 also measured some mechanical and elastic properties on Ryugu's samples. Ryugu seismic velocities are 2080 m/s and 1370 m/s for Vp and Vs respectively. Interestingly, Ryugu's seismic velocities are higher than those measured for Tagish Lake and lower than Murchison which is consistent with the possibility of reflecting an intraclast porosity that lies between those of the two meteorites. The seismic velocities of Ryugu are very close to the average measured for Moss (CO) of 2122 m/s and 1290 m/s for Vp and Vs respectively.

The correlation found in this study between Vp,Vs and the porosity, predicts an intraclast porosity of Ryugu around 32 % that is in strong agreement with the porosity derived from the grain and bulk density.

Considering the strong correlation observed for both UCS and shear strength with seismic velocities, we could speculate that Moss strength would be a good representation of Ryugu's clasts strength, but the mineralogies are significantly different. However, intraclast porosity also correlates with strength (UCS and DSS) and Ryugu samples are more porous than Moss, so Ryugu's clast might be slightly weaker. Comparing the Ryugu velocities to those of Murchison and Tagish Lake at least somewhat removes the variable of differing mineralogies suggesting that Ryugu's strengths lie between those two meteorites and likely closer to those of Tagish Lake.

The correlation found in this study between UCS, DSS and Vp, Vs predict a UCS for Ryugu clasts of 20 MPa and a DSS of 9 MPa.

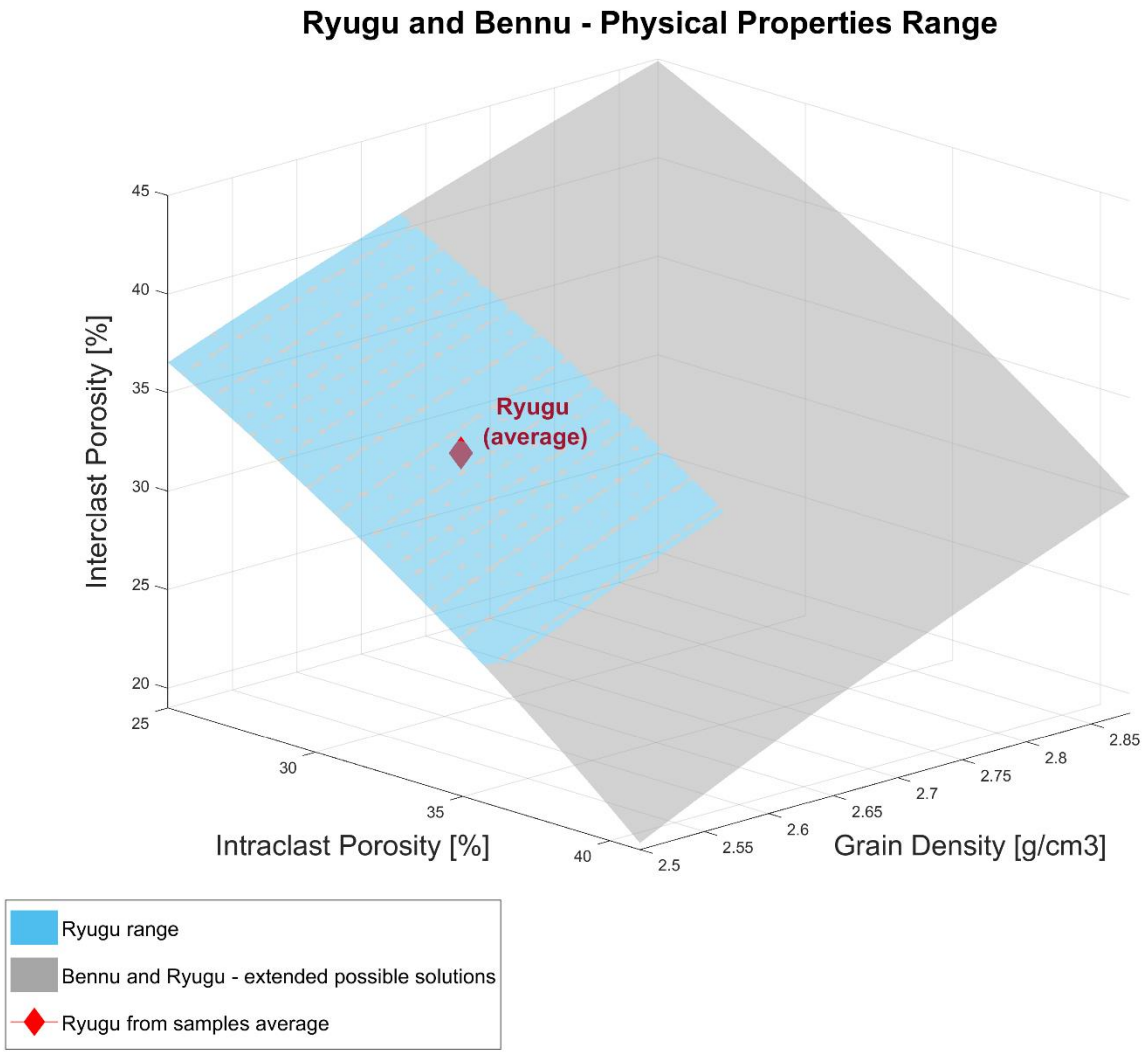

Figure 4.31: the 3D plot shows the possible range of physical properties (Intraclast porosity, interclast porosity and grain density) for Asteroids Ryugu and Bennu. For details refer to the text.

4.9 Modeling Asteroids

When trying to simulate certain phenomena like asteroid breakup or impact cratering on planets, it's crucial to have precise understanding of their physical, mechanical, and elastic properties. However, this has proven difficult due to limited data on the mechanical and elastic characteristics of meteorites. Consequently, numerous models rely on terrestrial comparisons, even though these may substantially deviate from meteorite properties. This underscores the significance of the data gathered in this research.

Asphaug et al., 1996 conducted a study on the effects of impact cratering on asteroid 243 Ida, where they employed mechanical and elastic dynamic parameters from terrestrial basalts to model the impact cratering process on asteroid Ida. For the target material, they used a dynamic Young's Modulus value of approximately 53 GPa. Ida is classified as an S-Type asteroid and shares compositional similarities with the LL group, as reported by Granahan et al., 2002. A potentially more suitable candidate for representing the properties of asteroid 243 Ida is the Golden meteorite, which exhibits characteristics of both L and LL chondrites and is exceptionally fresh, experiencing limited terrestrial weathering. Compared to the basalts used in the Asphaug et al., 1996 model, Golden displays notable differences in Young's Modulus and other mechanical properties. Specifically, Golden has a recorded dynamic Young's Modulus of 9.9 GPa and a static Young's Modulus of 4 GPa. Considering these differences, using the mechanical properties of Golden may lead to more accurate and representative models when studying the impact cratering effects on asteroid 243 Ida.

Michel et al., 2001, performed numerical simulations of asteroid collisions and reaccumulation for asteroids of two different families, the Eunomia and Koronis families.

The asteroids of the Eunomia family display two distinct hemispheres with different compositions, partially resembling the composition of the S-Type (ordinary chondrite) and partially resembling the composition of differentiated bodies [Nathues et al., 2005]. On other hands, the asteroids of the Koronis family have been classified as Q-type showing spectra between the L and LL chondrites [Rivkin et al., 2011]. The best representation for the properties of the Koronis asteroids is Golden meteorite that has properties between the L and LL chondrites (as discussed in previous sections of this thesis). Michel et al., 2001 modeled the parent asteroids of the Eunomia and Koronis families as solid basalts, possessing properties that would notably contrast with those of the Golden meteorite.

Molaro et al., 2020 studied thermal fatigue on asteroid Bennu as possible mechanism for particle ejections events and exfoliation-like fractures observed on numerous Bennu's boulders. They performed finite element modeling of stress fields induced in boulders from diurnal cycling on asteroid Bennu. Together with the thermal properties, the Young's Modulus and Poison Ratio of the boulders are the key inputs. Molaro et al., 2020 simulated both "dense" and "porous" boulders, with properties representing serpentinite's range of porosities (10% to 35%). The strain rate concerning thermal cycling can be considered quasi-static so static properties should be considered. Tagish Lake meteorite is the best representations for properties of Bennu, due to its mineralogy, porosity, and general aspect.

Considering the static Young's Modulus range of Tagish Lake, which spans from 0.4 to 0.57 GPa, the Young's Modulus most representative of the "porous" boulders in the Molaro et al., 2020 model may be ~ 1 GPa range assuming that Bennu's intraclast porosity is slightly lower than Tagish Lake's and that its mineralogy will be similar. This value is an

order of magnitude lower than the value of 15 GPa utilized in the model; its use would significantly affect the predicted stress field in Bennu's boulders.

Ballouz et al., 2021, examined the interaction between the OSIRIS-REx Touch-and-Go Sampling Acquisition Mechanism (TAGSAM) and Bennu's surface, in the context of granular physics to understand the projectiles penetration depth into granular materials. They modeled low-speed impact onto glass beads and dry sands. Some of the key inputs are the grain densities, coefficient of restitution, Young's Modulus and Poisson's ratio of the glass beads and dry sands. Considering the low-speed nature of the impacts studied, quasi-static properties should be considered. The properties of the glass beads and sand differ considerably from those of Tagish Lake, which is likely a more accurate representation of the properties of asteroid Bennu.

Watters et al., 2011 studied the formation of the Hinks Dorsum an 18km long ridge present at the surface of the S-Type asteroid 433 Eros. The authors of the paper used modeling techniques based on topographic data to determine that Hinks Dorsum was likely formed by a shallow-rooted thrust fault with a maximum depth of 250 m and a cumulative slip of around 90. This conclusion was based on the estimated near-surface shear strength of Eros that ranges from approximately 1 to 6 MPa. Eros has is an S-type asteroid with a composition similar to the L and LL even if a clear distinction is not clear [e.g, Peplowski, 2016]. Shear strength of the clasts at the surface of Eros could be at slow as 6.4 MPa as that is the weakest measured for Golden (range 6.4-18.4 MPa) that is the weakest meteorite among the L and LL. Therefore, the rock mass comprising Eros might not be expected to have such a large shear strength.

Zhang et al., 2018 have modeled how the critical spin and subsequent evolution of a rubble-pile asteroid may be influenced by its shear and cohesive strengths. The critical spin and evolution of asteroid and the role of shear strength has also been discussed widely in the literature [e.g., Holsapple, 2004]

4.10 Summary

Within the context of this study, we have compiled a comprehensive overview of essential static (Table 9) and dynamic (Table 10) properties associated with various asteroid lithologies. Our intention is for these summaries, presented in Table 9 and Table 10, to data imputs of reference for future asteroid modeling. The data presented in the tables originate from our investigation, with the exception of the porosity data for Tagish Lake, which was sourced from Hildebrand et al. (2006) since they measured the most pristine samples.

The derived range for tensile strength is founded upon the observation that the Unconfined Compressive Strength (UCS) surpasses the Tensile Strength by a factor of ten, a factor based upon terrestrial rock literature [e.g., Perras and Diedrichs, 2014].

Table 9: The table provides a summary of the static properties and porosities to be utilized in the modeling of various asteroid lithologies.

Asteroid Lithology	UCS [MPa]	DSS [MPa]	E_s [Gpa]	Prop. Limit [MPa]	Coef. of Rest.	Predicted Tensile Strength [MPa]	Porosity [%]
Saponite dominated (Tagish Lake/CI)	10	1.9	0.5	8	-	1	40
CM-like	80	31	10	50	0.55	8	18

C-chondrites weakly hydrated (CO)	24	9	-	-	-	2	21
Weak ordinary chondrite (LL/L)	38	12	4	28	0.63	3	13
Strong Ordinary Chondrite (H)	180	42	22	160	0.63	18	7
Enstatite-like	580	130	-	-	0.7	58	2.7

Table 10: The table provides a summary of the dynamic properties to be utilized in the modeling of various asteroid lithologies.

Asteroid Lithology	**Vp [m/s]**	**Vs [m/s]**	**E_d [Gpa]**	**ν_d**	**μ_d [Gpa]**	**K_d [Gpa]**
Saponite dominated (Tagish Lake/CI)	1350	800	2.5	0.25	1	1.5
CM-like	3200	1900	20	0.25	8.5	14
C-chondrites non hydrated (CO)	2150	1250	12	0.20	5	7
Weak ordinary chondrite (LL/L)	2000	1150	11	0.28	4	8
Strong Ordinary Chondrite (H)	3500	2000	38	0.25	15	25

Enstatite-like	6000	3000	85	0.36	32	110

5. CONCLUSIONS

Through a comprehensive exploration of the physical, mechanical, and elastic properties of meteorites, this study has shed new light on the strength of meteorites and related physical properties, offering fresh perspectives and expanding the boundaries of knowledge in meteorites and asteroid deformational behaviors.

UCS exponentially increases as porosity decreases below 10%, while reaching a plateau as porosity increases pass 30%. This distinctive trend underscores the pivotal role of porosity in shaping the mechanical properties of these materials. The plateauing of UCS at higher porosities challenges the conventional perception that stronger lithologies necessarily dominate the population of meteorites surviving atmospheric entry.

The study also uncovers robust correlations between UCS and seismic velocities (Vp, Vs), a significant discovery that fortifies the utility of these parameters in predicting the mechanical properties of meteorites from non-destructive testing. This correlation aligns harmoniously with the well-established body of knowledge on terrestrial rocks, highlighting the universality of these relationships across diverse materials and contexts.

The exploration of direct shear strength (DSS) data for meteorites contributes novel insights into their shear behavior. These fresh perspectives on shear behavior offer a more complete understanding of meteorite mechanical responses under various loading conditions.

Another particularly compelling aspect of this thesis lies in the examination of the static and dynamic Young's Modulus, shedding light on the intricate interplay between material

behavior and loading rates. The empirical relationships and correlations established, despite being constrained by currently available data, emphasize the pressing need for standardized measurement techniques and protocols.

Furthermore, the UCS/Proportional Limit ratio and coefficient of restitution provide valuable insights into the extent of elastic and plastic deformation, enriching our grasp of material behavior during impact and disruption events. These revelations offer pathways for understanding the intricate dynamics at play in asteroids during physical interactions.

The data collected in this study map the physical properties of hydrated carbonaceous chondrites, such as those seen in the Tagish Lake meteorite. These properties hold the potential to help decode the current state and evolutionary trajectories of primitive asteroids like Bennu and Ryugu. This understanding cascades into unraveling particle ejection events, surface regolith dynamics, and the intricate relationships between observed spacecraft data and laboratory measurements.

The intrinsic connection between material properties and physical interactions forms the bedrock of our investigation, underpinning the need to unravel the properties that define these bodies. The significance of this study becomes strikingly evident when we consider the implications of material properties on space phenomena. Objects hurtling through the cosmos, be they meteorites or asteroids, navigate a landscape punctuated by interaction and stress. The knowledge of their physical, elastic, and mechanical traits becomes critical inputs for understanding and modeling space events, from atmospheric entry to impact dynamics.

Insights from this study pertain to the survivability of meteorites during atmospheric entry, the representation of parent asteroids in our collections, and the broader implications of these properties on asteroid interactions.

Beyond its immediate implications, this research seamlessly intertwines with the realm of planetary defense. The landmark Double Asteroid Redirection Test (DART) mission serves as a testament to the importance of asteroid material properties in safeguarding our planet. As planetary defense missions become increasingly integral, the insights gleaned from this study bear profound significance. The intricate interplay between factors such as density, porosity, and strength underscore the complexity of deflecting potentially hazardous asteroids. Planetary defense becomes an ever-evolving frontier, with knowledge of asteroid material properties as fundamental to collisions outcomes. DART may have initiated this transformative journey, but a cascade of forthcoming missions awaits.

In conclusion, this PhD thesis represents a significant step forward in our understanding meteorites' mechanics. The culmination of over 5 years of research (in the crazy landscape of the COVID19 pandemic) has resulted in a comprehensive body of knowledge that contributes to both theoretical understanding and practical applications within planetary science.

REFERENCES

- A. R. Hildebrand, L. Hanton, M. Rankin, and M.I. Ibrahim (2015). *AN ASTEROID REGOLITH SIMULANT FOR HYDRATED CARBONACEOUS CHONDRITE LITHOLOGIES (HCCL-1).* 78th Annual Meeting of the Meteoritical Society, 5368.

- Abdalla, H., Abdul, M., Chaham, M., Sahar, A., Sofia, A., Boemi, N., Bougdah, H., Bozonnet, E., de Bonis, L., Hawkes, D., Kostopoulou, S., Mahgoub, Y., Mesbah, S., Mohareb, N., Gawad, I. O., Oostra, M., Pignatta, G., Pisello, A. L., Rosso, F., & Pradhan, B. (2019). *IEREK Interdisciplinary Series for Sustainable Development Editorial Board Members*. http://www.springer.com/series/15883

- Anovitz, L. M., & Cole, D. R. (2015). *Characterization and analysis of porosity and pore structures*. In Pore Scale Geochemical Processes (pp. 61–164). De Gruyter. https://doi.org/10.2138/rmg.2015.80.04

- Asphaug, E., Moore, J. M., Morrison, D., Benz, W., Nolan, M. C., & Sullivan, R. J. (1996). *Mechanical and Geological Effects of Impact Cratering on Ida*. In ICARUS (Vol. 120) 158-184.

- Ballouz, R. L., Walsh, K. J., Sánchez, P., Holsapple, K. A., Michel, P., Scheeres, D. J., Zhang, Y., Richardson, D. C., Barnouin, O. S., Nolan, M. C., Bierhaus, E. B., Connolly, H. C., Schwartz, S. R., Çelik, O., Baba, M., & Lauretta, D. S. (2021).

Modified granular impact force laws for the OSIRIS-REx touchdown on the surface of asteroid (101955) Bennu. Monthly Notices of the Royal Astronomical Society, 507(4), 5087–5105. https://doi.org/10.1093/mnras/stab2365

- Barton, N. (2013). *Shear strength criteria for rock, rock joints, rockfill and rock masses: Problems and some solutions*. Journal of Rock Mechanics and Geotechnical Engineering, 5(4), 249–261.

- Biele, J., Kesseler, L., Grimm, C. D., Schröder, S., Mierheim, O., Lange, M., & Ho, T.-M. (2017). *Experimental Determination of the Structural Coefficient of Restitution of a Bouncing Asteroid Lander*.

- Bierhaus B., B.C. Clark, J.W. Harris, K.S. Payne, R.D. Dubisher, D.W. Wurts, R.A. Hund, R.M. Kuhns, T.M. Linn, J.L. Wood, A.J. May, J.P. Dworkin, E. Beshore, D.S. Lauretta, the OSIRIS-REx Team (2018). *The OSIRIS-REx Spacecraft and the Touch-and-Go Sample Acquisition Mechanism (TAGSAM).* Space Sci Rev (2018) 214:107

- Bilet M., Roaldset E, (2013). *The meteorite Moss – a rare carbonaceous chondrite.* Meteoroids 2013, Proceedings of the Astronomical Conference, eds Jopek T.J., Rietmeijer F.J.M., Watanabe J., Williams I.P., Adam Mickiewicz University Press in Pozna´n, pp 69–74

- Bland, P. A., Jackson, M. D., Coker, R. F., Cohen, B. A., Webber, J. B. W., Lee, M. R., Duffy, C. M., Chater, R. J., Ardakani, M. G., McPhail, D. S., McComb, D. W., & Benedix, G. K. (2009). *Why aqueous alteration in asteroids was isochemical: High porosity ≠ high permeability*. Earth and Planetary Science Letters, 287(3–4), 559–568. https://doi.org/10.1016/j.epsl.2009.09.004

- Borovička, J., Spurný, P., & Shrbený, L. (2020). *Two Strengths of Ordinary Chondritic Meteoroids as Derived from Their Atmospheric Fragmentation Modeling.* The Astronomical Journal, 160(1), 42. https://doi.org/10.3847/1538-3881/ab9608

- Bottke Jr. William F., David Vokrouhlicky´, Miroslav Broz˘, David Nesvorny´, Alessandro Morbidelli (2001). *Dynamical Spreading of Asteroid Families by the Yarkovsky Effect.* SCIENCE VOL 294

- Brisset, J., Colwell, J., Dove, A., Abukhalil, S., Cox, C., & Mohammed, N. (2018). *Regolith behavior under asteroid-level gravity conditions: low-velocity impact experiments*. Progress in Earth and Planetary Science, 5(1). https://doi.org/10.1186/s40645-018-0222-5

- Britt, D. T., & Consolmagno, S. J. G. J. (2003). *Stony meteorite porosities and densities: A review of the data through 2001*. Meteoritics and Planetary Science, 38(8), 1161–1180. https://doi.org/10.1111/j.1945-5100.2003.tb00305.x

- Britt, D. T., Tholen, D. J., Bell, J. F., & Pieters, C. M. (1992). *Comparison of Asteroid and Meteorite Spectra: Classification by Principal Component Analysis*. ICARUS (Vol. 99). 153-166

- Britt, D. T., Yeomans, D., Housen, K., & Consolmagno, G. (2002). *Asteroid Density, Porosity, and Structure.* Asteroids III

- Brotons, V., Tomás, R., Ivorra, S., Grediaga, A., Martínez-Martínez, J., Benavente, D., & Gómez-Heras, M. (2016). *Improved correlation between the static and dynamic elastic modulus of different types of rocks*. Materials and Structures/Materiaux et Constructions, 49(8), 3021–3037. https://doi.org/10.1617/s11527-015-0702-7.

- Brown Peter G., Alan R. Hildebrand, Michael E. Zolensky, Monica Grady, Robert N. Clayton, Toshiko K. Mayeda, Edward Tagliaferri, Richard Spalding, Neil D. MacRae, Eric L. Hoffman, David W. Mittlefehldt, John F. Wacker, J. Andrew Bird, Margaret D. Campbell, Robert Carpenter, Heather Gingerich, Michael Glatiotis, Erika Greiner, Michael J. Mazur, Phil JA. McCausland, Howard Plotkin, and Tina Rubak Mazur (2000). *The Fall, Recovery, Orbit, and Composition of the Tagish Lake Meteorite: A New Type of Carbonaceous Chondrite*. Science Vol 290, Issue 5490, pp. 320-325, DOI: 10.1126/science.290.5490.320

- Bruck Syal, M., Michael Owen, J., & Miller, P. L. (2016). *Deflection by kinetic impact: Sensitivity to asteroid properties*. Icarus, 269, 50–61. https://doi.org/10.1016/j.icarus.2016.01.010

- Buddhue John Davis (1942), *The Compressive Strength of Meteorites.* https://doi.org/10.1111/j.1945-5100.1942.tb00140.x

- Castagna J. P., M. L. Batzle, and R. L. Eastwood (1985). *Relationships between compressional-wave and shear-wave velocities in clastic silicate rocks*. GEOPHYSICS Volume 50, Issue 4, https://doi.org/10.1190/1.1441933.

- Cheng A.F., P. Michel, M. Jutzi, A.S. Rivkin, A. Stickle, O. Barnouin, C. Ernst, J. Atchison, P. Pravec, D.C. Richardson, AIDA team, AIM team (2016). *Asteroid Impact & Deflection Assessment mission: Kinetic impactor.* Planetary and Space Science 121, 27-35, http://dx.doi.org/10.1016/j.pss.2015.12.004.

- Cheng, A. F., Agrusa, H. F., Barbee, B. W., Meyer, A. J., Farnham, T. L., Raducan, S. D., Richardson, D. C., Dotto, E., Zinzi, A., della Corte, V., Statler, T. S., Chesley, S., Naidu, S. P., Hirabayashi, M., Li, J. Y., Eggl, S., Barnouin, O. S., Chabot, N. L., Chocron, S., … Zanotti, G. (2023). *Momentum transfer from the DART mission kinetic impact on asteroid Dimorphos*. Nature, 616(7957), 457–460. https://doi.org/10.1038/s41586-023-05878-z

- Choquehe', P. W., Pray' Littleton, L. C., & Wisconsin, M. (1970). *Geologic Nomenclature and Classification of Porosity in Sedimentary Carbonates*. The American Association of Petroleum Geologists Bulletin V (Vol. 54, Issue February). pdf/54/2/207/4400454/aapg_1970_0054_0002_0207.pdf.

- Christaras, B., Auger, F., & Mosse, E. (1994). *Determination of the moduli of elasticity of rocks. Comparison of the ultrasonic velocity and mechanical resonance frequency methods with direct static methods*. In Materials and Structures (Vol. 27), 222-228.

- Ciccotti, M., & Mulargia, F. (2004). Differences between static and dynamic elastic moduli of a typical seismogenic rock. Geophysical Journal International, 157(1), 474–477. https://doi.org/10.1111/j.1365-246X.2004.02213.x

- Clark, B. E., Ferrone, S. M., Kaplan, H. H., & Zou, X. (2019). *Are the brighter rocks on Bennu products of recent mechanical weathering, and therefore less space-weathered?* EPSC Abstracts, Vol. 13, EPSC-DPS2019-962-1, 2019 EPSC-DPS Joint Meeting 2019

- Clayton Robert N., Toshiko K. Mayeda, Alan E. Rubin (1984). *Oxygen isotopic compositions of enstatite chondrites and aubrites*. Journal of Geophysical Research, https://doi.org/10.1029/JB089iS01p0C245

- Connolly, H. C., Zipfel, J., Folco, L., Smith, C., Jones, R. H., Benedix, G., Righter, K., Yamaguchi, A., Chennaoui, H., 10, A., & Grossman, J. N. (2007). The Meteoritical Bulletin, No. 91, 2007 March. In Meteoritics & Planetary Science (Vol. 42).

- Consolmagno, G. J., Britt, D. T., & Macke, R. J. (2008). *The significance of meteorite density and porosity*. Chemie Der Erde, 68(1), 1–29. https://doi.org/10.1016/j.chemer.2008.01.003

- Corkum, A. G., Asiri, Y., el Naggar, H., & Kinakin, D. (2018). *The Leeb Hardness Test for Rock: An Updated Methodology and UCS Correlation.* Rock Mechanics and Rock Engineering, 51(3), 665–675. https://doi.org/10.1007/s00603-017-1372-2

- Cotto-Figueroa, D., Asphaug, E., Garvie, L. A. J., Rai, A., Johnston, J., Borkowski, L., Datta, S., Chattopadhyay, A., & Morris, M. A. (2016). *Scale-dependent measurements of meteorite strength: Implications for asteroid fragmentation*. Icarus, 277, 73–77. https://doi.org/10.1016/j.icarus.2016.05.003

- Davarpanah, S. M., Ván, P., & Vásárhelyi, B. (2020). *Investigation of the relationship between dynamic and static deformation moduli of rocks*. In Geomechanics and Geophysics for Geo-Energy and Geo-Resources (Vol. 6, Issue

1). Springer Science and Business Media Deutschland GmbH. https://doi.org/10.1007/s40948-020-00155-z

- DeMeo, F. E., & Carry, B. (2014). *Solar System evolution from compositional mapping of the asteroid belt*. Nature, 505, 629–634.

- DeMeo, F. E., Binzel, R. P., Slivan, S. M., & Bus, S. J. (2009). *An extension of the Bus asteroid taxonomy into the near-infrared*. Icarus, 202(1), 160–180. https://doi.org/10.1016/j.icarus.2009.02.005

- Deo, S. N., & Kushvah, B. S. (2017). *Yarkovsky effect and solar radiation pressure on the orbital dynamics of the asteroid (101955) Bennu*. Astronomy and Computing, 20, 97–104. https://doi.org/10.1016/j.ascom.2017.07.002

- Elkatatny, S., Mahmoud, M., Mohamed, I., & Abdulraheem, A. (2018). *Development of a new correlation to determine the static Young's modulus*. Journal of Petroleum Exploration and Production Technology, 8(1), 17–30. https://doi.org/10.1007/s13202-017-0316-4

- Eugster O. (2003). *Cosmic-ray Exposure Ages of Meteorites and Lunar Rocks and Their Significance*. Geochemistry Volume 63, Issue 1, 2003, Pages 3-30.

- Flynn, G. J., Consolmagno, G. J., Brown, P., & Macke, R. J. (2017). *Physical properties of the stone meteorites: Implications for the properties of their parent bodies*. In Chemie der Erde (Vol. 78, Issue 3, pp. 269–298). Elsevier GmbH. https://doi.org/10.1016/j.chemer.2017.04.002

- Flynn, G. J., Durda, D. D., Molesky, M. J., May, B. A., Congram, S. N., Loftus, C. L., Reagan, J. R., Strait, M. M., & Macke, R. J. (2020). *Momentum transfer in hypervelocity cratering of meteorites and meteorite analogs: Implications for orbital evolution and kinetic impact deflection of asteroids*. International Journal of Impact Engineering, 136. https://doi.org/10.1016/j.ijimpeng.2019.103437

- Fossen, H. (2016). *Structural Geology. Second Edition.* Cambridge University Press, Cambridge.

- Fry, C., Melanson, D., Samson, C., Mccausland, P. J. A., Herd, R. K., Ernst, R. E., Umoh, J., & Holdsworth, D. W. (2013). *Physical characterization of a suite of Buzzard Coulee H4 chondrite fragments*. Meteoritics and Planetary Science, 48(6), 1060–1073. https://doi.org/10.1111/maps.12130

- Fuchs, L. H., & Jansen, K. J. (1970). *Mineralogy and composition of the Murchison meteorite.* Meteoritical Society

- Fujiwara, A., Kawaguchi, J., Yeomans, D. K., Abe, M., Mukai, T., Okada, T., Saito, J., Yano, H., Yoshikawa, M., Scheeres, D. J., Barnouin-Jha, O., Cheng, A. F., Demura, H., Gaskell, R. W., Hirata, N., Ikeda, H., Kominato, T., Miyamoto, H.,

Nakamura, A. M., … Uesugi, K. (2006). *The Rubble-Pile Asteroid Itokawa as Observed by Hayabusa*. Science VOL 312, HAYABUSA ASTEROID ITOKAWA REPORT

- Gao, Y., Cheng, B., & Yu, Y. (2022). *The interactive dynamics of a binary asteroid and ejecta after medium kinetic impact*. Astrophysics and Space Science, 367(8). https://doi.org/10.1007/s10509-022-04111-z

- GATTACCECA Je´rome, Millarca VALENZUELA, Minoru UEHARA, A. J. Timothy JULL, Marlene GISCARD, Pierre ROCHETTE, Regis BRAUCHER, Clement SUAVET, Matthieu GOUNELLE, Diego MORATA, Pablo MUNAYCO, Michele BOUROT-DENISE, Didier BOURLES, and Francois DEMOR (2011). *The densest meteorite collection area in hot deserts: The San Juan meteorite field (Atacama Desert, Chile).* Meteoritics & Planetary Science46, Nr 9, 1276–1287 (2011).

- Ghanizadeh Amin; Christopher R. Clarkson; Atena Vahedian; Omid H. Ardakani; James M. Wood; Hamed Sanei (2018). *Laboratory-based characterization of pore network and matrix permeability in the Montney Formation: Insights from methodology comparisons.* Bulletin of Canadian Petroleum Geology (2018) 66 (2): 472–498.

- Ghanizadeh, A., Rashidi, B., Clarkson, C.R., Vahedian, A., Vocke, C.P. (2017). *Indirect Estimation of Fluid Transport and Rock Mechanical Properties from Elemental Compositions: Implications for "Sweet Spot" Identification in the Montney Formation (Canada).* Unconventional Resources Technology Conference (URTeC) DOI 10.15530-urtec-2017-267089

- Ghorbani, S., Hoseinie, S. H., Ghasemi, E., & Sherizadeh, T. (2022). *Application of Leeb Hardness Test in Prediction of Dynamic Elastic Constants of Sedimentary and Igneous Rocks. Geotechnical and Geological Engineering*, 40(6), 3125–3145. https://doi.org/10.1007/s10706-022-02083-z

- Golden, D. C., Ming, D. W., & Zolensky, M. E. (1992). *CHEMISTRY AND MINERALOGY OF OXIDATION PRODUCTS FROM A NICKE-RICH ATAXITE*. LPSC XXIII

- Granahan, J. (2002). *A compositional study of asteroid 243 Ida and Dactyl from Galileo NIMS and SSI observations*. Journal of Geophysical Research: Planets, 107(10). https://doi.org/10.1029/2001je001759

- Griffin, A. A., Millman, P. M., & Halliday, I. (1991). *The fall of the Abee meteorite and its probable orbit*. The Royal Astronomical Society of Canada, 86 (1).

- Grossman, J., & Rubin, A. (2006). *White paper report for the Nomenclature Committee on the composition of olivine and pyroxene in equilibrated ordinary chondrites.*

- Halliday, I., & McIntosh, B. A. (1990). *Orbit of the Murchison meteorite*. Meteoritics, 25(4), 339–340. https://doi.org/10.1111/j.1945-5100.1990.tb00718.x

- Hamada, G., & Joseph, V. (2020). *Developed correlations between sound wave velocity and porosity, permeability and mechanical properties of sandstone core samples.* Petroleum Research, 5(4), 326–338. https://doi.org/10.1016/j.ptlrs.2020.07.001

- Hamilton, V. E., Simon, A. A., Christensen, P. R., Reuter, D. C., Clark, B. E., Barucci, M. A., Bowles, N. E., Boynton, W. v., Brucato, J. R., Cloutis, E. A., Connolly, H. C., Donaldson Hanna, K. L., Emery, J. P., Enos, H. L., Fornasier, S., Haberle, C. W., Hanna, R. D., Howell, E. S., Kaplan, H. H., … Marty, B. (2019). *Evidence for widespread hydrated minerals on asteroid (101955) Bennu*. Nature Astronomy, 3(4), 332–340. https://doi.org/10.1038/s41550-019-0722-2

- Hergenrother, C. W., Maleszewski, C. K., Nolan, M. C., Li, J. Y., Drouet d'Aubigny, C. Y., Shelly, F. C., Howell, E. S., Kareta, T. R., Izawa, M. R. M., Barucci, M. A., Bierhaus, E. B., Campins, H., Chesley, S. R., Clark, B. E., Christensen, E. J., DellaGiustina, D. N., Fornasier, S., Golish, D. R., Hartzell, C.

M., … Marty, B. (2019). T*he operational environment and rotational acceleration of asteroid (101955)* Bennu from OSIRIS-REx observations. Nature Communications, 10(1). https://doi.org/10.1038/s41467-019-09213-x

- Hildebrand, A. R., McCausland, P. J. A., Brown, P. G., Longstaffe, F. J., Russell, S. D. J., Tagliaferri, E., Wacker, J. F., & Mazur, M. J. (2006). *The fall and recovery of the Tagish Lake meteorite*. Meteoritics and Planetary Science, 41(3), 407–431. https://doi.org/10.1111/j.1945-5100.2006.tb00471.x

- Hisayoshi Yurimoto, Ken-ichi Abe, Masanao Abe, Mitsuru Ebihara, Akio Fujimura, Minako Hashiguchi, et al., (2011). *Oxygen Isotopic Compositions of Asteroidal Materials Returned from Itokawa by the Hayabusa Mission*. VOL 333 SCIENCE

F

- Hons, M. 2004. Compressional and shear wave velocity in meteorites. B.Sc. Thesis, Department of Geology and Geophysics, University of Calgary, Calgary, Alberta.

- Holsapple, K. A. (2004). *Equilibrium figures of spinning bodies with self-gravity*. Icarus, 172(1 SPEC.ISS.), 272–303. https://doi.org/10.1016/j.icarus.2004.05.023

- Hook, J. R. (2003). *An Introduction to Porosity*. PETROPHYSICS, VOL. 44, NO. 3 (MAY-JUNE 2003); P. 205–212.

- Housen, K. R., Sweet, W. J., & Holsapple, K. A. (2018). *Impacts into porous asteroids*. Icarus, 300, 72–96. https://doi.org/10.1016/j.icarus.2017.08.019
- Hutson, L., Ruzicka, A. M., Milley, E. P., & Hildebrand, A. R. (2009). *A FIRST LOOK AT THE PETROGRAPHY OF THE BUZZARD COULEE (H4) CHONDRITE, A RECENTLY OBSERVED FALL FROM SASKATCHEWAN*. Lunar and Planetary Science Conference (Issue 1983).

- Ibrahim, Mahadia, E. (2012). *The Elastic Properties of Carbonaceous Chondrites.* Master Thesis, University of Calgary https://doi.org/10.11575/PRISM/28122.

- Jaumann, R., Schmitz, N., Ho, T.-M., Schröder, S. E., Otto, K. A., Stephan, K., Elgner, S., Krohn, K., Preusker, F., Scholten, F., Biele, J., Ulamec, S., Krause, C., Sugita, S., Matz, K.-D., Roatsch, T., Parekh, R., Mottola, S., Grott, M., … Kouyama, T. (2019). *Images from the surface of asteroid Ryugu show rocks similar to carbonaceous chondrite meteorites*. Science 365, 817–820

- Karaman, K., & Kesimal, A. (2015). *Correlation of Schmidt Rebound Hardness with Uniaxial Compressive Strength and P-Wave Velocity of Rock Materials*. Arabian Journal for Science and Engineering, 40(7), 1897–1906. https://doi.org/10.1007/s13369-014-1510-z

- Kimberley, J., & Ramesh, K. T. (2011). *The dynamic strength of an ordinary chondrite.* Meteoritics and Planetary Science, 46(11), 1653–1669. https://doi.org/10.1111/j.1945-5100.2011.01254.x
- Kitazato, K., Milliken, R. E., Iwata, T., Abe, M., Ohtake, M., Matsuura, S., Arai, T., Nakauchi, Y., Nakamura, T., Matsuoka, M., et al., (2019). *The surface composition of asteroid 162173 Ryugu from Hayabusa2 near-infrared spectroscopy*. Science, https://www.science.org.
- Kotsanis, D., Nomikos, P., & Rozos, D. (2021). *Comparison of Static and Dynamic Young's Modulus of Prasinites.* Mater. Proc. 2021, 5, 54. https://doi.org/10.3390/materproc 2021005054
- Krot, A. N., Keil, K., Goodrich, C. A., Scott, E. R. D., & Weisberg, M. K. (2005). *Classification of Meteorites*. Meteorites, Comets, and Planets: Treatise on Geochemistry, Second Edition, Volume 1.
- Kumamoto, K. M., Owen, J. M., Syal, M. B., Pearl, J., Raskin, C., Caldwell, W. K., Rainey, E., Stickle, A. M., Daly, R. T., & Barnouin, O. (2022). *Predicting Asteroid Material Properties from a DART-like Kinetic Impact*. Planetary Science Journal, 3(10). https://doi.org/10.3847/PSJ/ac93f2
- Lauretta, D. S., & Dellagiustina, D. N. (2019). *OSIRIS-REx SAMPLE SCIENCE AND THE GEOLOGY OF ACTIVE ASTEROID BENNU*. In Nature Geoscience (Vol. 568).

- Lauretta, D. S., DellaGiustina, D. N., Bennett, C. A., Golish, D. R., Becker, K. J., Balram-Knutson, S. S., Barnouin, O. S., Becker, T. L., Bottke, W. F., Boynton, W. v., Campins, H., Clark, B. E., Connolly, H. C., Drouet d'Aubigny, C. Y., Dworkin, J. P., Emery, J. P., Enos, H. L., Hamilton, V. E., Hergenrother, C. W., … Marty, B. (2019). *The unexpected surface of asteroid (101955) Bennu*. Nature, 568(7750), 55–60. https://doi.org/10.1038/s41586-019-1033-6

- Lauretta, D. S., Hergenrother, C. W., Chesley, S. R., Leonard, J. M., Pelgrift, J. Y., Adam, C. D., Asad, M. al, Antreasian, P. G., Ballouz, R. L., Becker, K. J., Bennett, C. A., Bos, B. J., Bottke, W. F., Brozović, M., Campins, H., Connolly, H. C., Daly, M. G., Davis, A. B., de León, J., … Wolner, C. W. V. (2019). *Episodes of particle ejection from the surface of the active asteroid (101955) Bennu.* Science, 366(6470). https://doi.org/10.1126/science.aay3544

- Lee, M. W. (2003). *Velocity Ratio and its Application to Predicting Velocities*. U.S. Geological Survey Bulletin, 2197. http://geology.cr.usgs.gov/pub/bulletins/b2197

- Lewis John S. (2004). *Physics and Chemistry of the Solar System (Second Edition)*. ELSEVIER, INC.

- Liu, P. H., Wu, J. H., & Lee, D. H. (2022). *New rock strength-based UCS-Vp correlation equation for different rock types by statistical regression methods*.

Geomechanics for Energy and the Environment, 32. https://doi.org/10.1016/j.gete.2022.100403

- MacDonald, N. R., Packulak, T. R. M., & Day, J. J. (2023). *A Critical Review of Current States of Practice in Direct Shear Testing of Unfilled Rock Fractures Focused on Multi-Stage and Boundary Conditions*. Geosciences, 13(6), 172. https://doi.org/10.3390/geosciences13060172

- Macke, R. J. (2010). *Survey Of Meteorite Physical Properties Density, Porosity And Magnetic Susceptibility.* Doctoral Dissertation, University of Central Florida.

- Macke, R. J., Consolmagno, G. J., & Britt, D. T. (2011). *Density, porosity, and magnetic susceptibility of carbonaceous chondrites*. Meteoritics and Planetary Science, 46(12), 1842–1862. https://doi.org/10.1111/j.1945-5100.2011.01298

- Martínez-Martínez, J., Benavente, D., & García-del-Cura, M. A. (2012). *Comparison of the static and dynamic elastic modulus in carbonate rocks*. Bulletin of Engineering Geology and the Environment, 71(2), 263–268. https://doi.org/10.1007/s10064-011-0399-y

- McSween, H. Y. Jr. (1999). *Meteorites and Their Parent Planets (Second).* Cambridge University Press.

- Michel, P., Benz, W., Tanga, P., & Richardson, D. C. (2001). *Collisions and Gravitational Reaccumulation: Forming Asteroid Families and Satellites*. Science, 294, 1696–1700.
- Michel, P., DeMeo, F. E., & Bottke, W. F. (2015). *Asteroids IV* (P. Michel, F. E. DeMeo, & W. F. Bottke, Eds.). University of Arizona Press. https://doi.org/10.2458/azu_uapress_9780816532131
- Michel, P., Küppers, M., Bagatin, A. C., Carry, B., Charnoz, S., de Leon, J., Fitzsimmons, A., Gordo, P., Green, S. F., Hérique, A., Juzi, M., Karatekin, Ö., Kohout, T., Lazzarin, M., Murdoch, N., Okada, T., Palomba, E., Pravec, P., Snodgrass, C., … Carnelli, I. (2022). *The ESA Hera Mission: Detailed Characterization of the DART Impact Outcome and of the Binary Asteroid (65803) Didymos*. Planetary Science Journal, 3(7). https://doi.org/10.3847/PSJ/ac6f52
- Milley, E. P., Hildebrand, A. R., Brown, P. G., Noble, M., Sarty, G., Ling, A., & Maillet, L. A. (2009). *Pre-fall Orbit of the Buzzard Coulee Meteoroid*. GeoCanada 2010 – Working with the Earth
- Mishra, D. A., & Basu, A. (2013). *Estimation of uniaxial compressive strength of rock materials by index tests using regression analysis and fuzzy inference system*. Engineering Geology, 160, 54–68. https://doi.org/10.1016/j.enggeo.2013.04.004

- Mittlefehldt, D. W., Clayton, R. N., Drake, M. J., & Righter, K. (2008). *Oxygen isotopic composition and chemical correlations in meteorites and the terrestrial planets*. In Oxygen in the Solar System (pp. 399–428). De Gruyter Mouton. https://doi.org/10.2138/rmg.2008.68.14
- Molaro, J. L., Hergenrother, C. W., Chesley, S. R., Walsh, K. J., Hanna, R. D., Haberle, C. W., Schwartz, S. R., Ballouz, R. L., Bottke, W. F., Campins, H. J., & Lauretta, D. S. (2020). *Thermal Fatigue as a Driving Mechanism for Activity on Asteroid Bennu*. Journal of Geophysical Research: Planets, 125(8). https://doi.org/10.1029/2019JE006325
- Nakamura, T., Matsumoto, M., Amano, K., Enokido, Y., Zolensky, M. E., Mikouchi, T., Genda, H., Tanaka, S., Zolotov, M. Y., Kurosawa, K., Wakita, S., Hyodo, R., Nagano, H., Nakashima, D., Takahashi, Y., Fujioka, Y., Kikuiri, M., Kagawa, E., Matsuoka, M., … Tsuda, Y. (2022). *Formation and evolution of carbonaceous asteroid Ryugu: Direct evidence from returned samples. Science*, 379(6634). https://doi.org/10.1126/science.abn8671/10.1126/
- Nathues, A., Mottola, S., Kaasalainen, M., & Neukum, G. (2005). Spectral study of the Eunomia asteroid family. I. Eunomia. Icarus, 175(2), 452–463. https://doi.org/10.1016/j.icarus.2004.12.013

- Nolan, M. C., Asphaug, E., Melosh, H. J., & Greenberg, R. (1996). *Impact Craters on Asteroids: Does Gravity or Strength Control Their Size?* ICARUS (Vol. 124). 359–371

- Ostrowski, D., & Bryson, K. (2019). The physical properties of meteorites. In Planetary and Space Science (Vol. 165, pp. 148–178). Elsevier Ltd. https://doi.org/10.1016/j.pss.2018.11.003

- Ota, T., Potiszil, C., Kobayashi, K., Tanaka, R., Kitagawa, H., Kunihiro, T., Sakaguchi, C., Yamanaka, M., & Nakamura, E. (2023). *The Formation of a Rubble Pile Asteroid: Insights from the Asteroid Ryugu.* Universe, 9(6), 293. https://doi.org/10.3390/universe9060293

- Patrick N. Peplowski, 2016. *The global elemental composition of 433 Eros: First results from the NEAR gamma-ray spectrometer orbital dataset.* Planetary and Space Science, Volume 134, 1 December 2016, Pages 36-51

- Perras, M.A. and Diedrichs, M.S., 2014, a Review of the Tensile Strength of Rock: Concepts and Testing, Geotechnical and Geological Engineering doi:10.1007/s10706-014-9732-0

- Pohl, L., & Britt, D. T. (2020). *Strengths of meteorites—An overview and analysis of available data.* Meteoritics and Planetary Science, 55(4), 962–987. https://doi.org/10.1111/maps.13449

- Rivkin, A. S., Li, J. Y., Milliken, R. E., Lim, L. F., Lovell, A. J., Schmidt, B. E., McFadden, L. A., & Cohen, B. A. (2011). *The surface composition of Ceres.* Space Science Reviews, 163(1–4), 95–116. https://doi.org/10.1007/s11214-010-9677-4

- Rubin, A. E., & Keil, K. (1983). *Mineralogy and petrology of the Abee enstatite chondrite breccia and its dark inclusions*. Earth and Planetary Science Letters, 62 (1983) 118-131

- Rubin, A. E., & Scott Z, E. R. D. (1997). *Abee and related EH chondrite impact-melt breccias*. In Geochimica et Cosmochimica Acta (Vol. 61, Issue 2) 425-435.

- Rubin, A. E., Trigo-Rodríguez, J. M., Huber, H., & Wasson, J. T. (2007). *Progressive aqueous alteration of CM carbonaceous chondrites*. Geochimica et Cosmochimica Acta, 71(9), 2361–2382. https://doi.org/10.1016/j.gca.2007.02.008

- Schmitt-Kopplin, P., Gabelica, Z., Gougeon, R. D., Fekete, A., Kanawati, B., Harir, M., Gebefuegi, I., Eckel, G., & Hertkorn, N. (2010). *High molecular diversity of extraterrestrial organic matter in Murchison meteorite revealed 40 years after its fall*. Proceedings of the National Academy of Sciences of the United States of America, 107(7), 2763–2768. https://doi.org/10.1073/pnas.0912157107

- Sing, K. S. W., Everett, D. H., Haul, R. A. W., Moscou, L., Pierotti, R. A., Rouquerol, J., & Siemieniewska, T. (1984). *Reporting physisorption data for gas/solid systems-with special reference to the determination of surface area and porosity.* Pure & App. Chem., Vol. 57, No. 4, pp. 603—619, 1985.

- Sugita, S., Honda, R., Morota, T., Kameda, S., Sawada, H., Tatsumi, E., Yamada, M., Honda, C., Yokota, Y., Kouyama, T., Sakatani, N., et al., (2019). *The geomorphology, color, and thermal properties of Ryugu: Implications for parent-body processes*. Science, 364(6437). https://doi.org

- Svetsov V. V., Nemtchinov I.V. (1995). *Disintegration of Large Meteoroids in Earth's Atmosphere: Theoretical Models.* Icarus, Volume 116, Issue 1, July 1995, Pages 131-153

- Szabo, P. S., Poppe, A. R., Biber, H., Mutzke, A., Pichler, J., Jäggi, N., Galli, A., Wurz, P., & Aumayr, F. (2022). *Deducing Lunar Regolith Porosity From Energetic Neutral Atom Emission.* Geophysical Research Letters, 49(21). https://doi.org/10.1029/2022GL101232

- Thommes, M., Kaneko, K., Neimark, A. v., Olivier, J. P., Rodriguez-Reinoso, F., Rouquerol, J., & Sing, K. S. W. (2015). *Physisorption of gases, with special reference to the evaluation of surface area and pore size distribution (IUPAC*

Technical Report). Pure and Applied Chemistry, 87(9–10), 1051–1069. https://doi.org/10.1515/pac-2014-1117

- Tsuchiyama, A., Mashio, E., Imai, Y., Noguchi, T., Miura, Y. N., & Yano, H. (2008). *Strength measurements of carbonaceous chondrites and cosmic dust analogs using micro compression testing machine*. P-168-002. http://astrogranma.ess.sci.osaka-u.ac.jp/

- Walsh, K. J. (2018). *Annual Review of Astronomy and Astrophysics Rubble Pile Asteroids*. Annu. Rev. Astron. Astrophys. 2018. 56:593–624 https://doi.org/10.1146/annurev-astro-081817

- Walsh, K. J., Jawin, E. R., Ballouz, R. L., Barnouin, O. S., Bierhaus, E. B., Connolly, H. C., Molaro, J. L., McCoy, T. J., Delbo', M., Hartzell, C. M., Pajola, M., Schwartz, S. R., Trang, D., Asphaug, E., Becker, K. J., Beddingfield, C. B., Bennett, C. A., Bottke, W. F., Burke, K. N., … Lauretta, D. S. (2019). *Craters, boulders and regolith of (101955) bennu indicative of an old and dynamic surface*. Nature Geoscience, 12, 242–246. https://doi.org/10.1038/s41561-019-0326-6

- Watters, T. R., Thomas, P. C., & Robinson, M. S. (2011). *Thrust faults and the near-surface strength of asteroid 433 Eros*. Geophysical Research Letters, 38(2). https://doi.org/10.1029/2010GL045302

- Weisberg, M. K., Mccoy, T. J., & Krot, A. N. (2006). Systematics and Evaluation of Meteorite Classification. Meteorites and the Early Solar System II.
- Yaşar, E., & Erdoğan, Y. (2004). *Estimation of rock physicomechanical properties using hardness methods*. Engineering Geology, 71(3–4), 281–288. https://doi.org/10.1016/S0013-7952(03)00141-8.
- Yayoi N. Miura; Takaaki Noguch; Akira Tsuchiyam; Hajime Yano; Shingo Yoshida; Kohei Nagata (2008). *Compressive strength measurements of meteorites and terrestrial rocks: Implications for physical properties of asteroidal surfaces*. P168-P002
- Yu, C., Ji, S., & Li, Q. (2016). *Effects of porosity on seismic velocities, elastic moduli and Poisson's ratios of solid materials and rocks.* Journal of Rock Mechanics and Geotechnical Engineering, 8(1), 35–49. https://doi.org/10.1016/j.jrmge.2015.07.004.
- Zhang Yun, Derek C. Richardson, Olivier S. Barnouin, Patrick Michel, Stephen R. Schwartz, and Ronald-Louis Ballouz (2018). *Rotational Failure of Rubble-pile Bodies: Influences of Shear and Cohesive Strengths*. The Astrophysical Journal, Volume 857, Number 1, 10.3847/1538-4357/aab5b2.

- Zolensky, M. E., & Gooding, J. L. (1989). *Aqueous alteration on carbonaceous-chondrite parent bodies as inferred from weathering of meteorites in Antartica*. Meteoritical Society, 548–549.
- Zolensky, M. E., Nakamura, K., Gounelle, M., Mikouchi, T., Kasama, T., Tachikawa, O., & Tonui, E. (2002). *Mineralogy of Tagish Lake: An ungrouped type 2 carbonaceous chondrite*. Meteoritics and Planetary Science, 37(5), 737–761. https://doi.org/10.1111/j.1945-5100.2002.tb00852.x

APPENDIX A

ASTM International standards list

ASTM D7012-14 Standard Test Methods for Compressive Strength and Elastic Moduli of Intact Rock Core Specimens under Varying States of Stress and Temperatures

ASTM D4543-08 Standard Practices for Preparing Rock Core as Cylindrical Test Specimens and Verifying Conformance to Dimensional and Shape Tolerances

ASTM D5731-08 Standard Test Method for Determination of the Point Load Strength Index of Rock and Application to Rock Strength Classifications

ASTM D3967-08 Standard Test Method for Splitting Tensile Strength of Intact Rock Core Specimens

ASTM D2936-08 Standard Test Method for Direct Tensile Strength of Intact Rock Core Specimens

ASTM D5607-08 Standard Test Method for Performing Laboratory Direct Shear Strength Tests of Rock Specimens Under Constant Normal Force

ASTM E83 – 23 Standard Practice for Verification and Classification of Extensometer Systems

ASTM A956/A956M-17a Standard Test Method for Leeb Hardness Testing of Steel Products

ASTM D2845 - 00 Standard Test Method for Laboratory Determination of Pulse Velocities and Ultrasonic Elastic Constants of Rock

ASTM D2938 SCT39 Method for Determining the Unconfined Compressive Strength of Intact Rock Core Specimens

ASTM D5550.1117501-1 Standard Test Method for Specific Gravity of Soil Solids by Gas Pycnometer